UCL Université catholique de Louvain

École polytechnique de Louvain (EPL)

epl

Red Blood Cells Analysis in Fluorescence Microscopy Images

Dissertation presented by
Alice FRISSON

for obtaining the Master's degree in
Biomedical Engineering

Supervisor(s)
Christophe DE VLEESCHOUWER

Reader(s)
Benoit MACQ, Donatienne TYTECA

Academic year 2017-2018

Contents

Contents **2**

Acknowledgements **3**

List of Figures **7**

List of Abbreviations **8**

1 Introduction **9**
1.1 Biological Context . . . 9
1.1.1 Images description . . . 9
1.1.2 Problem statement . . . 12
1.2 General methods in segmentation and bright spots detection . . . 13
1.2.1 Image processing techniques . . . 13
1.2.2 Learning based techniques . . . 14
1.2.3 Method selection . . . 14
1.3 Work Contributions . . . 14

2 State of the Art Review **16**
2.1 Salient points detection . . . 16
2.2 Cells segmentation . . . 17
2.2.1 Intensity Thresholding . . . 17
2.2.2 Morphology Operators . . . 18
2.2.3 Watershed Transform . . . 19
2.2.4 Circular Hough Transform . . . 23

3 Bright Spots Detection **25**
3.1 Prior knowledge . . . 25
3.2 Confocal microscopy images . . . 25
3.2.1 Iterative Thresholding method . . . 25
3.2.2 Unique Thresholding and Filtering method . . . 25
3.3 Wide-field microscopy images . . . 26
3.4 Spots size computation . . . 27
3.5 Parameters summary . . . 27

4 Cells Segmentation **28**
4.1 Prior knowledge . . . 28
4.2 Confocal microscopy images . . . 28
4.2.1 Thresholding controlled watershed . . . 29
4.2.2 CHT controlled watershed . . . 31
4.3 Wide-field microscopy images . . . 32
4.4 Elliptic red blood cells . . . 33

4.5 Irrelevant cells detection . . . 33
4.6 Parameters summary . . . 34

5 Validation method **35**
5.1 Validation metrics . . . 35
5.1.1 Segmentation . . . 36
5.1.2 Bright spots detection . . . 36
5.2 Domains Analysis metrics . . . 36
5.3 Used Parameters . . . 37

6 Algorithms validation **39**
6.1 Confocal images . . . 39
6.1.1 Cells Segmentation . . . 39
6.1.2 Bright spots detection . . . 44
6.1.3 Partial conclusion for confocal images . . . 49
6.2 Wide-field images . . . 50
6.2.1 Cells Segmentation . . . 50
6.2.2 Bright spots Detection . . . 52
6.2.3 Partial conclusion on wide-field images . . . 54
6.3 Irrelevant cells detection . . . 54

7 Lipidic Domains Analysis **56**
7.1 Cholesterol domains . . . 56
7.1.1 Number of bright spots . . . 56
7.1.2 Bright spots location . . . 58
7.1.3 Domains area and surface coverage . . . 60
7.1.4 Partial conclusion on cholesterol domains . . . 61
7.2 Sphingomyelin domains . . . 62
7.2.1 Number of bright spots . . . 62
7.2.2 Bright spots location . . . 63
7.2.3 Domains area and surface coverage . . . 64
7.2.4 Partial conclusion on sphingomyelin domains . . . 65

8 Conclusion **66**

Bibliography **71**

Appendices **72**

A Additional segmentation results **73**

B Additional detection results **79**

Acknowledgements

Work is made of collaboration. It promotes ideas exchange, creativity, reassessment and continuous improvement. With colleagues, work gets better and better. This is why, in the context of my master thesis, I would like to thank people who worked with me during this year and helped to improve this work. First, I am specially grateful for the assistance given by Christophe De Vleeschouwer, for his regular coaching and feedback. Then, I would like to thank Donatienne Tyteca and Hélène Pollet, who took time to explain me the biology behind images, to answer my questions and to provide me databases and manual results; and Benoit Macq, for accepting to read my thesis and giving his opinion about it. Finally, I would like to thank my family and friends for their moral support.

List of Figures

1.1 Wide-field microscopy image of Sphingomyelin labelled with BODIPY, this probe emits green light. Sphingomyelin domains are located only in the central part of the cell. . . . 10
1.2 Confocal microscopy image of Sphingomyelin labelled with BODIPY, this probe emits green light. Sphingomyelin domains are located only in the central part of the cell. . . . 10
1.3 Confocal microscopy image of Cholesterol labelled by the Theta probe, this probe emits red light. Cholesterol domains are located on the centrum and periphery of the cell. . . . 10
1.4 Confocal microscopy image of cholesterol domains : Fluorescence image. . . . 11
1.5 Confocal microscopy image of cholesterol domains : Transmission image. . . . 11
1.6 Wide-field microscopy image of sphingomyelin domains : Fluorescence image. . . 11
1.7 Wide-field microscopy image of sphingomyelin domains : Transmission image. . . 11
1.8 Examples of artifact and exception occuring in images. Confocal microscopy image and transmission image are superimposed. . . . 12

2.1 Mexican hat function in the 3D-space, generated by a difference of two Gaussian functions. It shows why it is called a Mexican hat. . . . 17
2.2 Real Gaussian second order derivative in y-direction (first panel) and in xy-direction (second panel) and their corresponding box integral approximation (third and fourth panels) [3] . . . 17
2.3 Dilation operation : The operator enlarges the boundaries of the binary images. A is the original image, B is the structuring element, $A \oplus B$ is the resulting image. (from [44]) . . . 18
2.4 Erosion operation : The operator crops the boundaries of the binary images. A is the original image, B is the structuring element, $A \ominus B$ is the resulting image. (from [44]) . . . 18
2.5 Opening with a 3X3 square structuring element. (from [13]) . . . 19
2.6 Closing with a 3X3 square structuring element. (from [12]) . . . 19
2.7 Graphical representation of the merge tree method. (a) Watershed segmented regions of the input image, (b) Region adjacency graph built from segmentation, (c) Merge tree built from the region adjacency graph and used for merging the over-segmented regions [20]. . . . 21
2.8 Schematic representation of the morphological reconstruction algorithm. The red curve is the input mask and the blue curve is the input image. This algorithm is used to apply our control marker for the watershed algorithm on the transmission image to segment [26]. . . . 22
2.9 Example of how morphological reconstruction can be used to impose a local minimum on an image. This algorithm is used to apply our control marker for the watershed algorithm on the transmission image to segment [26]. . . . 22
2.10 Accumulation pattern in the 3D space for a unique detected edge point (from [29]) 23

3.1 Mexican Hat used for bright spots detection in the Unique Thresholding and filtering method :$\Psi(x) = (2 - 1.475x^2)e^{\frac{-x^2}{2}}$. Parameters are chosen to have a low response for cells borders (red integral must be low) and a high response for spots (magenta integral must be high). Point diameter is here of 5 pixels, the red integral is of 5.66 and the magenta integral is of 19.08. 26
3.2 Example for fluorescence image in the case of BODIPY-labelling : the analysis of the histogram can be used to define the threshold between cells and background. The threshold between regions 1 and 2 is defined as the minimum location between the two larger maximum in the histogram. 27

4.1 Confocal microscopy images of cholesterol domains : the transmission image is used for watershed algorithm since it has high intensity values at cells edges, this is not the case for the fluorescence image. 29
4.2 Example of transmission image in the case of theta-labelling : the analysis of the histogram can be used to define the threshold between the inner part of the cells, their borders and the rest of the image 30
4.3 Example of the impact of control marker used in watershed segmentation 30
4.4 Histogram of the accumulator value occurrences. It is used to define the threshold on the accumulator value above which they correspond to a circle. This threshold is defined as the value for which the filtered histogram slope is the lowest multiplied by a factor of 1.5. 31
4.5 Example of the impact of control marker used in watershed segmentation 32

5.1 Example of annotated image 35

6.1 Segmentation results for confocal images of healthy cells, with the two proposed methods : left column is for CHT controlled watershed and right column is for thresholding controlled watershed. The image to segment, the markers, the segmentation results as well as the regions kept from the segmentation and that correspond to cells are shown. 41
6.2 Segmentation results for confocal images of elliptic cells, with the two proposed methods : left column is for CHT controlled watershed and right column is for thresholding controlled watershed. The image to segment, the markers, the segmentation results as well as the regions kept from the segmentation and that correspond to cells are shown. 42
6.3 Number of cells detected with each method and for each image : (a) healthy cells, (b) elliptic cells. 43
6.4 Detection rate for each method and for each image : (a) healthy cells, (b) elliptic cells. 43
6.5 Cells shape coefficient for each method and for each image : (a) healthy cells, (b) elliptic cells. 44
6.6 Bright spots detection results for both methods. Red dots are detection results and green circles are ground truth. The upper row shows total images while the lower row shows zoomed versions of images. 45
6.7 Comparison between both methods - Green dots : Unique thresholding and filtering method results; red circles : Iterative thresholding method results. 45
6.8 Unique thresholding and filtering method : bright spots detection results with different thresholds 46
6.9 ROC curve for the bright spot detection methods on confocal images. 46
6.10 Analysis of the detection rate and false positive rate per cell for healthy cells. . . 48
6.11 Analysis of the detection rate and false positive rate per cell for elliptic cells. . . 48

6.12 Segmentation results for wide-field images of healthy (left column) and elliptic cells (right column). The image to segment, the marker, the segmentation results as well as the regions kept from the segmentation and that correspond to cells are shown. 51
6.13 Detection rate and shape coefficient for the different images for healthy cells. . . 52
6.14 Detection rate and shape coefficient for the different images for elliptic cells. . . . 52
6.15 Bright spots detection results for healthy cells and elliptic cells. Red dots are algorithm results and green dots are ground truth. 53
6.16 Analysis of detection rate and false positive rate for healthy and elliptic cells . . 53
6.17 Ransac results for a sphingomyelin marked image (wide-field acquired image) . . 55

7.1 Analysis of the number of bright spots per cell. 57
7.2 Density of bright spots : upper panel : healthy cells; lower panel : elliptic cells. . 57
7.3 Comparison of bright spots distributions between ground truth and both detection methods for healthy cells. The left panel is the cumulative number of spots and the right panel is the normalized curve. 58
7.4 Comparison of bright spots distribution between ground truth and both detection methods for elliptic cells. The left panel is the cumulative number of spots and the right panel is the normalized curve. 59
7.5 Percentage of bright spots in the central part of cells for ground truth and algorithmic results : upper panel : healthy cells; lower panel : elliptic cells. . . . 60
7.6 Frequency histogram of domains size 61
7.7 Coverage percentage for healthy and elliptic cells 61
7.8 Frequency of the number of brights spots per cell for healthy cells (left panel) and elliptic cells (right panel). 62
7.9 Density of domains : left panel : healthy cells; right panel : elliptic cells 62
7.10 Comparison of bright spots distributions between ground truth and method detection for healthy cells. The left panel is the cumulative number of spots and the right panel is the normalized curve. 63
7.11 Comparison of bright spots distributions between ground truth and method detection for elliptic cells. The left panel is the cumulative number of spots and the right panel is the normalized curve 63
7.12 Percentage of bright spots located in the central part of cells for healthy cells and elliptic ones. Comparison between ground truth and algorithm results are provided. Left panel : healthy cells; right panel : elliptic cells. 64
7.13 Sphingomyelin domains size evaluation results for 2 domains. Left images : fluorescent images, central images : thresholded images, right images : domain contour applied on fluorescent images. 65
7.14 Left panel : frequency histogram of domains size; right panel : frequency histogram of domains coverage 65

A.1 Results images at each step of the Thresholding controlled watershed for a confocal image of healthy cells (Theta labelling). 73
A.2 Results images at each step of the CHT controlled watershed for a confocal image of healthy cells (Theta labelling). 74
A.3 Results images at each step of the Thresholding controlled watershed for a confocal image of elliptic cells (Theta labelling). 75
A.4 Results images at each step of the CHT controlled watershed for a confocal image of elliptic cells (Theta labelling). 76
A.5 Results images at each step of the algorithm for a wide-field image of healthy cells (BODIPY-sphingomyelin labelling). 77

A.6 Results images at each step of the algorithm for a wide-field image of elliptic cells (BODIPY-sphingomyelin labelling). 78

B.1 Detection results for a confocal image of elliptic cells. Red dots are algorithm results and green circles are ground truth spots. 79

List of Abbreviations

- BODIPY : Bore-dipyromethene
- CHT : Circular Hough Transform
- DR : Detection rate
- FPR : False positive rate
- HE : Hereditary elliptocytosis
- HS : Hereditary spherocytosis
- RBC : Red blood cells

Chapter 1

Introduction

1.1 Biological Context

Red blood cells (RBC), also called erythrocytes, are the most important cell type in blood. Their role is to ensure tissues oxygenation by transporting oxygen. Oxygen is fixed to RBC thanks to haemoglobin. RBC have a well known shape : they are biconcave disks with a diameter of about 8 μm. However, some diseases can modify this shape. Two common disorders are hereditary elliptocytosis (HE) and hereditary spherocytosis (HS) [14]. HE is characterized by elliptic RBC. They are formed due to mechanical weakness or fragility of their membrane caused by defects in some proteins. HE can lead to anemia and jaundice but most of the time patients are asymptomatic [14]. HS is characterized by a lack of cohesion and stabilization properties of cells [9][11]. It leads to a reduced cells life span mainly due to the fact that damaged cells are destructed by the spleen. This leads to an increased erythropoietic rate and if the red blood cells production rate is not sufficient enough, it leads to anemia. It will increase the bilirubin level and can potentially trigger jaundice and gallstones [9][35].

Researchers from the CELL Unit in *De Duve Institute* are currently analyzing red blood cells to figure out how and why their mechanical properties are weakened [23]. Previous researchers [34] thought red blood cells membranes were quite homogeneous structures. However, Léonard C. and co-authors [23] found out that membranes are composed of lipidic domains : some are very small (nanometric) while others are larger (micrometric). These larger ones show different organizations for ill patients compared to healthy subjects and can thus be thought to play a role in HE and HS. To be able to quantify better the organization of these domains, red blood cells are analyzed by fluorescence microscopy [23]. Fluorescent probes are attached to the domains under analysis and create bright spots in fluorescence images. Researchers are then able to see where micrometric domains are localized and in what quantity. Currently, these images are manually processed and it can be very time consuming because a lot of data need to be analyzed. To help researchers, image processing tools are needed to perform automatic analysis of the images. This will reduce time dedicated to image analysis and will provide more reliable quantitative results. The processing tools will also enable the analysis of a huge amount of images and provide quantitative and statistically relevant comparisons between patients, which could potentially be useful for clinical purposes.

1.1.1 Images description

For their research, biologists work with control samples (healthy subjects) but also with samples from patients suffering from elliptocytosis and spherocytosis. Images represent thus circular or elliptic cells. Different fluorescent labelling but also different microscopes have been considered during acquisition. We will explain here the impact of these choices on the obtained images and

characterize them visually. We will also point out artifacts that can be observed in samples and that must be taken into account.

Fluorescent labelling

Tyteca et al. have identified in 2 types of domains. The first kind of domains are spots composed of cholesterol. These domains are found in the central part of red blood cells but also on their edges. The second kind of domains are composed of sphingomyelin, these ones are always found in the central part of red blood cells. To analyze these domains, they used different fluorescent agents [23]. For sphingomyelin domains (fig. 1.1 and 1.2), they enriched RBC membranes with BODIPY-sphingomyelin molecules. The sphingomyelin part will behave normally in the cell, while the BODIPY part will emit light to track the organisation of sphingomyelin. Since sphingomyelin is present everywhere in the membrane (and more in domains), light is emitted from the whole cell. For cholesterol domains (fig. 1.3), the D4 Theta toxin is used to bind to the cholesterol molecules naturally present in domains. Cholesterol is not present in other membrane structures and thus light is only emitted from domains. These probes respectively emit green and red light and thus determine the color of the acquired image.

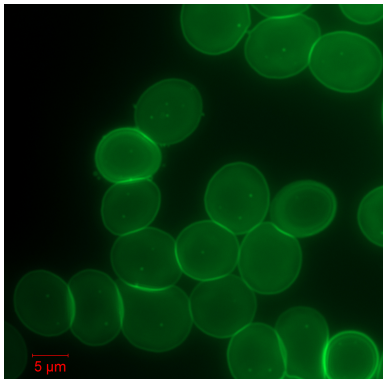


Figure 1.1: Wide-field microscopy image of Sphingomyelin labelled with BODIPY, this probe emits green light. Sphingomyelin domains are located only in the central part of the cell.

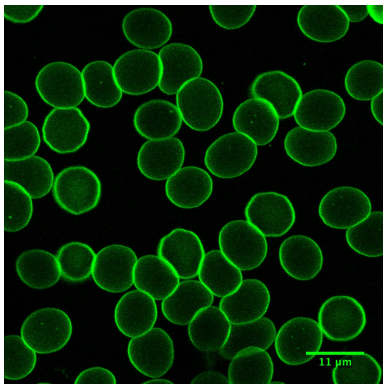


Figure 1.2: Confocal microscopy image of Sphingomyelin labelled with BODIPY, this probe emits green light. Sphingomyelin domains are located only in the central part of the cell.

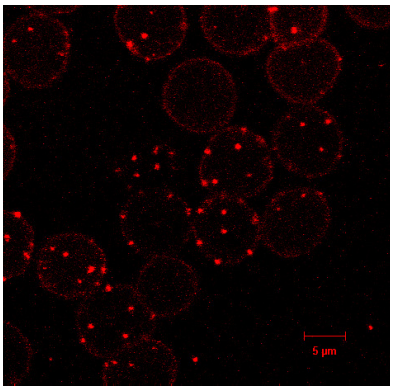


Figure 1.3: Confocal microscopy image of Cholesterol labelled by the Theta probe, this probe emits red light. Cholesterol domains are located on the centrum and periphery of the cell.

Microscope type

To capture images, 2 types of microscopes are considered : wide-field fluorescent microscopy and confocal microscopy. Wide-field fluorescent microscopes gather the light emitted by the whole sample structure and thus leads to brighter images : red blood cells are brighter and the spots are more difficult to see (fig. 1.1). This microscope can produce an image in less than one second. Alternatively, confocal microscopy may be used. In this case, only the light coming from a thin layer (400 nm) of the sample is recorded. This leads to darker images where the spots are easier to see (fig. 1.2 and 1.3). However, this technique takes more time to produce images (15 secondes for one image[1]) and is also more expensive to use. Biologists chose to use both techniques. They use wide-field microscopy for sphingomyelin domain analysis. Capturing the whole fluorescence emitted from the sample is not a problem here since domains are located in the center of the cell and can be easily seen. On the contrary, confocal microscopy is used

[1] Acquisition times are provided as indicative values since they depend on many parameters and can vary considerably.

to analyze cholesterol domains. Indeed, since these domains are also located on the border of the cell, they are less visible on wide-field fluorescent images. Moreover, they appear blurred and are difficult to detect even manually, leading to counting discrepancies between researchers. Confocal microscopy is thus favoured for this case, with the disadvantage of a higher cost.

Finally, for both techniques, the microscope gives two images : the transmission image (fig. 1.5 and 1.7) built from the light passing through the sample and thus without the fluorescent information; and the fluorescent image (fig. 1.4 and 1.6) built from the light emitted by the fluorescent probes.

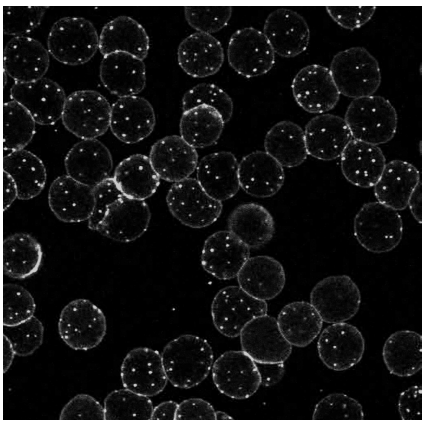


Figure 1.4: Confocal microscopy image of cholesterol domains : Fluorescence image.

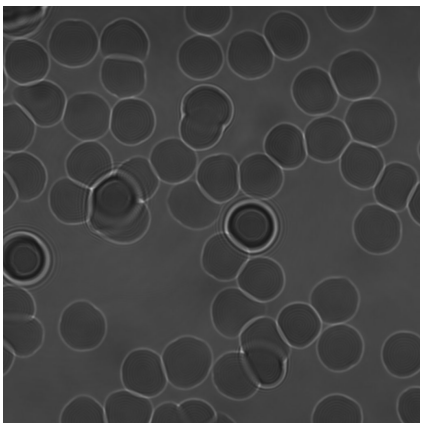


Figure 1.5: Confocal microscopy image of cholesterol domains : Transmission image.

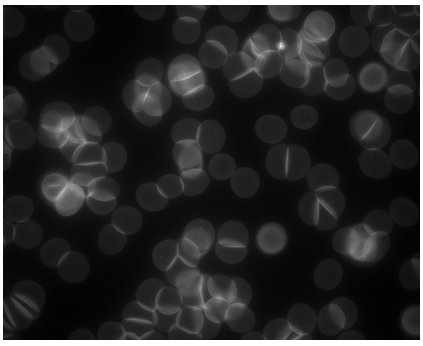


Figure 1.6: Wide-field microscopy image of sphingomyelin domains : Fluorescence image.

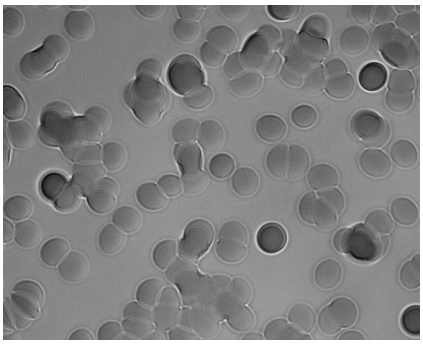


Figure 1.7: Wide-field microscopy image of sphingomyelin domains : Transmission image.

Images characteristics and biological relevance of their visual features

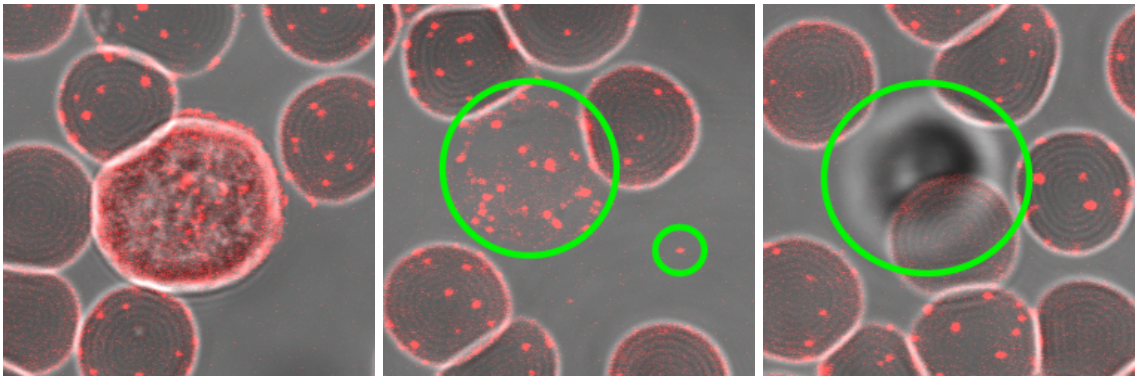
Whatever their acquisition method and fluorescent labelling, images show common properties.

- The microscope returns grey-level images : for convenience, color is then added to the fluorescence images to reflect the emitted color of the probe but it brings no information.
- Resolution may differ from one image to the other. However, each image is given with its resolution (number of pixels) and scale (total real size of the image).
- Lipidic domains are bright spots in the images with a diameter of about 0.5-0.6 nm. Red blood cells are very well shaped cells : there are circular with a diameter of about 8 μm.

Samples are not perfect. Potential artifacts have to be taken into account when segmenting and analyzing red blood cells. The main irregularities and sources of confusion that can occur are :

- The presence of another cell : generally a white blood cell. These cells are larger and can thus be removed based on their size (fig. 1.8(a)).
- The presence of dying cells : these cells begin to vesiculate and bright spots are released by the cell. These isolated bright spots and the ones belonging to the dying cell must not be taken into account. These dying cells are not present in the transmission images, we will thus make our cell segmentation on these images (fig. 1.8(b)).
- Artifacts due to cells lying above or under the confocal plane or mis-placed on the support : these cells are seen in the transmission images but they don't show bright spots in the fluorescent image. They can be differentiated from confocal cells in the transmission images due to their darker appearance (fig. 1.8(c)).

The given examples only show cholesterol domains, however these exceptions are also seen for sphingomyelin domains.



(a) White blood cell (b) Dying cell that vesiculates (c) Artifact due to a cell out of the confocal plane

Figure 1.8: Examples of artifact and exception occuring in images. Confocal microscopy image and transmission image are superimposed.

1.1.2 Problem statement

Concretely, researchers are interested in different information. They would like to :

- Count the number of bright spots and thus the number of lipidic domains per red blood cell unit surface;
- Count the surface occupied by the bright spots per red blood cell unit surface;
- Compute the radial distribution of bright spots in a cell by looking at their distances to the center of the cell.

These requirements can be translated in two problems : Bright Spots Detection and Cells Segmentation. The proposed algorithm will thus focus on these two tasks. On top of this, methods used to compute spots sizes and remove unwanted cells will also be presented.

As explained previously, images can be obtained with different acquisition procedures. Biologists are mainly using BODIPY-labelled domains acquired with wide-field microscopy to see

Sphingomyelin domains and Theta-labelled domains acquired with confocal microscopy to see Cholesterol domains. The developed methods will thus focus on these images. These two types of images will be called wide-field images and confocal images, without mentioning the used probe. When talking about bright spots detection in confocal images, we are thus speaking about cholesterol domains, and similarly, the bright spots detection in wide-field images refers to Sphingomyelin domains (this nomenclature is summarized in table 1.1). Since currently no processing tool exists to solve this problem, the running time is not critical. However, achieving a running time comparable to the acquisition time (1s/image for wide-field microscopy and 15s/image for confocal microscopy) should be convenient. Concretely, algorithms for the three tasks must be provided in the form of a MATLAB program.

	Wide-field microscopy	Confocal microscopy
Sphingomyelin domains	Referred as wide-field images (fig. 1.1)	Not used in this work (fig. 1.2)
Cholesterol domains	Not used in this work	Referred as confocal images (fig. 1.3)

Table 1.1: Nomenclature used for the different image types

1.2 General methods in segmentation and bright spots detection

A lot of techniques are currently used for cells image analysis [17][41]. Mainly two general approaches can be used to analyze images : image processing techniques and learning techniques. These two can either be used for cell segmentation or for bright spots detection. Different methods belong to these categories and have already been used for red blood cells analysis. Moreover, in most cases, many methods are combined together to perform the whole processing. We will explain them briefly and a deeper explanation of methods used in this work, will be given in section 2.

1.2.1 Image processing techniques

This type of techniques has the property to keep the pixel representation of the image to analyze it. Algorithms directly use a numbers array that keep track of the spatial location of each intensity value. A first method is thresholding. The idea is to keep only pixels that have an intensity higher or lower than the pre-defined threshold. The threshold can be the same for the whole image or can be adapted depending on the illumination of the image [32]. Then, we have corner detectors. These methods aim at finding image patterns by comparison of pixel intensity. Different detectors have already been proposed depending on the type of pattern to analyze [16][18][21]. Mathematical Morphology can also be used [31]. It can be applied on grey-level images but is generally applied on binary images (that can be obtained from thresholding, for example). It consists of 2 operations : dilation and erosion, that will respectively dilate or erode the binary mask of the image. Other techniques that are more focused on segmentation are the Watershed algorithm [8][27][39]; the Hough Transform and in particular the Circular Hough Transform that is adapted for circle detection [43] and Active Contours. Active contours algorithm starts from a manually drawn curve around the object to segment and by minimizing an energy associated to this curve, the curve will converge toward the edge of the object.

1.2.2 Learning based techniques

Even if pixels locations is always taken into account, the pixel representation is not central in these types of methods. There are mainly three algorithms that are used in cell segmentation.

The first one is clustering. It relies on features extraction and computations in the feature space. Characteristics for each pixel are computed and form a feature vector. Pixels belonging to the same object are supposed to be close to each other in the feature space : these features need to be chosen adequately depending on the type of cells and the type of images. In most cases, cells are of the same type and show the same features, they thus cannot be clustered into different clusters. We end up then with only two clusters. If different types of cells are present, clustering can be used to distinguish them. The distance between vectors can be computed with different metrics : Euclidean distance and correlation being the most used ones. Based on these distances, algorithms will cluster vectors together. There are mainly three algorithms used for this purpose [41] : K-means, fuzzy C-means [5] and Expectation-Maximization.

Then, we have graph-based methods. These methods represent pixels or sub-pixels as nodes in a graph. Edges between nodes correspond to the similarity between the two pixels and thus their likelihood to belong to the same object. Nodes are then partitioned, building the segmentation of each object. Some methods require the number of output partitions, while others do not [38].

Finally, supervised classification can also be used. This method relies on a model that has previously been built based on data : this can be a geometrical representation as in [7] or a probabilistic one. Each pixel can be classified independently or super-pixel blocks can be built and then classified. Both techniques are not able to handle touching object and thus require second step to segment them. Different well-known classification algorithms are used for cell segmentation once the model is built : Support Vector Machine (SVM) [33], Convolutional Neural Networks (CNN) [37][40] or also the K-Nearest Neighbors (KNN).

1.2.3 Method selection

Since we are working on red blood cells, we have a very good prior on the object we are looking for. These cells are circular and their radius is approximately known. Moreover, all cells have the same appearance. Their edges are also already well defined in images. Concerning the bright spots detection, their size is well known and they are defined by a high intensity. Due to these reasons, we are going to use an image processing approach to solve the current task. Indeed, with these kind of methods we can use our prior information to define the parameters of our methods. On the contrary, with learning techniques, the prior information is not used in the implementation : the algorithm is going to find it by itself. However, in our case, this prior might not be easy to find by learning since we can have noisy images.

1.3 Work Contributions

The solution to the biologists task will be first to segment cells from the transmission image and then to detect the bright spots from the fluorescence image. Bright spots that are lying outside of cells will be removed and only the other ones will be kept in our computations. Finally, we will be able to count the number of spots, the number of cells, evaluate their surface and location. Each spot can then be assigned to one cell and finally the spot density and radical distribution can be computed.

The structure of this report will be the following. In chapter 2, we will present the different algorithms we are going to use to perform cells segmentation and bright spots detection. Then, chapters 3 and 4 will be devoted to our methods explanation, respectively for Bright spots detection and Cells Segmentation. Next, chapter 5 will present the different metrics that are

used to analyze algorithm performances and to characterize bright spots. It also defines precisely the input parameters that are used to perform it. The ground truth will also be defined in this chapter. Afterwards, results of the predefined algorithms on the testing data will be presented and discussed (chapter 6). This consists mainly in comparing algorithm results with ground truth. Chapter 7 will then present a brief analysis of lipidic domains (detected bright spots) properties. These properties will be compared with other literature results that has already been gathered and with ground truth. For each property, comparison between healthy cells and elliptic ones will also be made. The relevance to use the proposed methods to compare these cells will be assessed. Finally, a conclusion about the proposed method and its results will be given in chapter 8.

Chapter 2

State of the Art Review

This chapter introduces the main image processing techniques that are considered to answer biologists questions. The way these techniques are adapted will be given in chapters 3 and 4.

2.1 Salient points detection

Bright spots detection can be seen as a salient point detection problem, also named corner detection in the literature.

Salient points correspond to singularities in the image intensity pattern. Detecting them will largely rely on the comparison of pixels intensities in a local neighborhood, using appropriate filters. A first simple corner detector was proposed by Moravec [16]. It takes a window and compare this window to adjacent ones. If there is a large difference between the two, an edge is present. This is repeated in all four directions and determine if we have an edge, a corner, an isolated point or a flat surface. Harris [16] improved this tool by considering smaller window shifts and by using smoothing functions. The Harris detector was then used as a starting point for other works [22]. Kitchen and Rosenberg [18] also built salient point detectors by combining edge detection and gradient computation.

Concerning edge detectors, we have also differential local filters [24]. This filter category clusters Prewitt, Sobel and Robert filters. Unlike Moravec detector that compares windows to detect a gradient, they compare neighbouring pixels intensities directly. They can be represented as convolution kernels, typically a 2x2 matrix for Robert and a 3x3 matrix for Sobel and Prewitt filters. These filters are directional, meaning they only detect edges in one direction. To find all edges, the image is filtered in each direction and the solutions of all filterings are added. As example [15], two Sobel operators are given here : S_1 detects vertical edges and S_2 detects horizontal edges.

$$S_1 = \begin{pmatrix} -1 & 0 & 1 \\ -2 & 0 & 2 \\ -1 & 0 & 1 \end{pmatrix} \quad S_2 = \begin{pmatrix} 1 & 2 & 1 \\ 0 & 0 & 0 \\ -1 & -2 & -1 \end{pmatrix}$$

More advanced works have been developed to have scale invariant detectors. It is the case of the SIFT (Scale Invariant Feature Transform) detector [22]. The method uses a Gaussian function $G(x, y, \sigma)$, as scale-space kernel that is then convoluted with the image intensity I(x,y):

$$L(x, y, \sigma) = G(x, y, \sigma) * I(x, y)$$

To detect salient points, a difference of these Gaussian functions is applied on the input image [22]. This corresponds to filter the image with two different Gaussian filters and then substracting the obtained images.

$$D(x, y, \sigma) = (G(x, y, k\sigma) - G(x, y, \sigma)) * I(x, y) = L(x, y, k\sigma) - L(x, y, \sigma)$$

Here, the two Gaussian functions have standard deviations σ and $k\sigma$. This difference of Gaussian functions is also called the Mexican Hat function (as can be understood in figure 2.1). This Mexican Hat can be seen as an approximation for the Laplacian of Gaussians filter. Formally, Mexican Hat functions can also be defined like,

$$\Psi(x) = (2 - x^2)e^{\frac{-x^2}{2}}$$

where x = |**x**|, the length of the position vector **x**. Bay [3] went a step further and developed the SURF (Speeded-Up Robust Features) detector. It uses the Hessian matrix and approximate it as done in SIFT, by image integrals. Mathematically, it is written as follows :

$$H(\mathbf{x}, \sigma) = \begin{bmatrix} L_{xx}(\mathbf{x}, \sigma) & L_{xy}(\mathbf{x}, \sigma) \\ L_{yx}(\mathbf{x}, \sigma) & L_{yy}(\mathbf{x}, \sigma) \end{bmatrix}$$

where **x** is an image point (x,y), $L_{xx}(\mathbf{x}, \sigma)$ is the convolution of the Gaussian second order derivative with the image I in point **x** and similarly for the other directions. In practice, the filtered values will be estimated with box integrals that are faster to compute (fig. 2.2). These techniques can be easily extended to color images since RGB images can be seen as three gray-level images. They were also further developed to be scale and affine invariant [36].

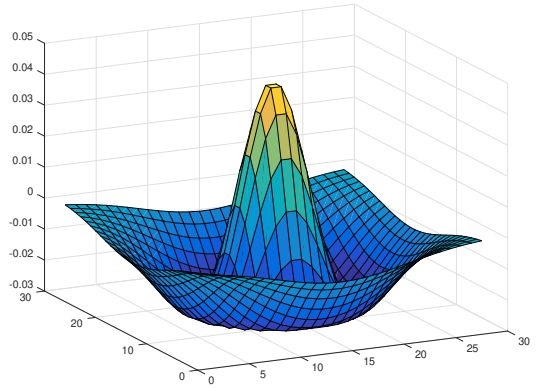


Figure 2.1: Mexican hat function in the 3D-space, generated by a difference of two Gaussian functions. It shows why it is called a Mexican hat.

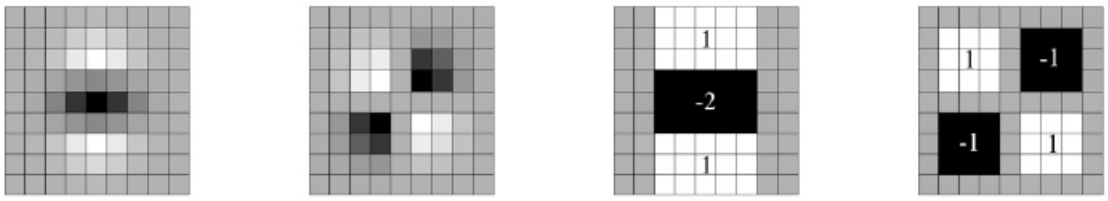


Figure 2.2: Real Gaussian second order derivative in y-direction (first panel) and in xy-direction (second panel) and their corresponding box integral approximation (third and fourth panels) [3]

2.2 Cells segmentation

Cells segmentation techniques have been widely investigated. Many techniques are used nowadays to solve this problem [17][41]. The aim of cell segmentation is to define the boundary of each cell in the image. This allows to distinguish each cell from other cells and from background.

2.2.1 Intensity Thresholding

Thresholding is a simple image processing tool that consists in keeping only pixels that have an intensity lower or higher than a predefined threshold. This operation will produce a binary image, defining if the pixel is above or under the threshold. The method is suited for segmenting images in which the object (e.g. cell) of interest has a higher or lower intensity than the rest of the image. In simple images, the threshold may be the same for the whole image. In more complex cases, where the illumination is not the same everywhere, a locally adaptative threshold may be used. Otsu's method [32] computes this local threshold on sub-windows of the local image by maximizing the between-class variance of the current sub-window. Alternatively, iterative thresholding can be used. It is the use of successive thresholdings. Thresholds may

be increasing or decreasing, the thresholds used are defined by a maximum threshold t_{max}, a minimum threshold t_{min} and a number of iteration $n_{iteration}$. In the context of this work, iterative thresholding is used in two ways for bright spots detection. The first one, referred here after as *sequential thresholding*, will apply sequentially different thresholds on the same initial image. For each threshold, pixels that have a larger (lower) intensity are set to one (zero). The obtained binary image is analyzed to extract white pixels regions that correspond to bright spots based on a geometry criterion. Finally, the best threshold is chosen to maximize the number of regions that have the right properties. This threshold is used for a final thresholding that will define regions that are kept. A second way of using *iterative thresholding* is to adapt the image that is thresholded at each step. For the first step, the image is thresholded with the highest threshold. Again, pixels that have a larger (lower) intensity are set to one (zero). Regions properties are then computed and only regions that have properties corresponding to the criteria are kept. These regions are stored and removed from the initial image. This new image is then used for the next thresholding. The process is repeated again with decreasing thresholds until the minimum threshold is reached. At each step, the regions that are kept are stored to finally have a mask of all kept regions.

2.2.2 Morphology Operators

Mathematical morphology applies on binary and grey-level images. We restricted here our definition for binary images since, in the rest of our work, mathematical morphology is only considered to denoise thresholded images. Basically, two operations exist : erosion and dilation. These operations apply a structuring element $B \in Z^2$ on the image $A \in Z^2$ and are defined as follows [10][44]:

$$\textbf{Dilation :} \quad A \oplus B = \cup_{b \in B} A_b$$

$$\textbf{Erosion :} \quad A \ominus B = \cap_{b \in B} A_{-b}$$

with $A_b = \{c \in Z^2 \quad | \quad c = a + b, \text{ for some } a \in A\}$. A schematic representation of the two operators is given in figures 2.3 and 2.4.

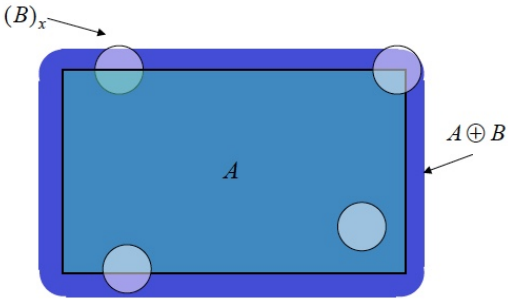


Figure 2.3: Dilation operation : The operator enlarges the boundaries of the binary images. A is the original image, B is the structuring element, $A \oplus B$ is the resulting image. (from [44])

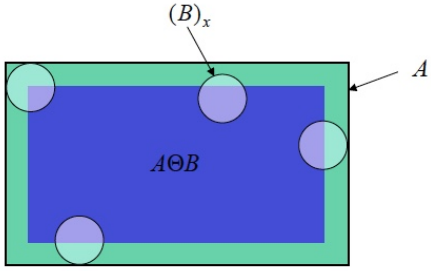


Figure 2.4: Erosion operation : The operator crops the boundaries of the binary images. A is the original image, B is the structuring element, $A \ominus B$ is the resulting image. (from [44])

These two operations can be applied successively and create two other ones called opening and closing and defined as follows:

$$\textbf{Opening :} \quad A \bullet B = (A \oplus B) \ominus B$$

$$\textbf{Closing :} \quad A \circ B = (A \ominus B) \oplus B$$

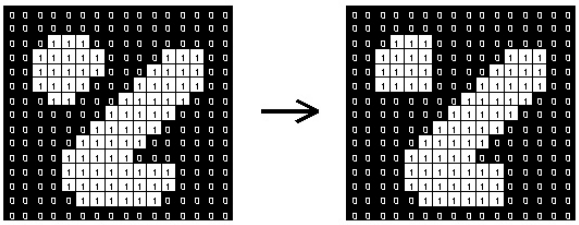


Figure 2.5: Opening with a 3X3 square structuring element. (from [13])

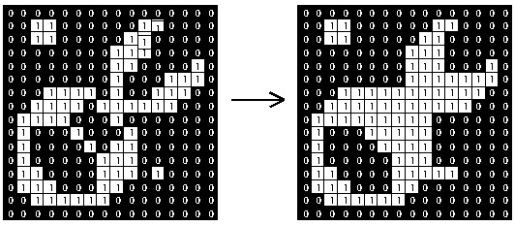


Figure 2.6: Closing with a 3X3 square structuring element. (from [12])

2.2.3 Watershed Transform

Watershed transform is widely used for segmentation. The pixel intensity or alternatively the image gradient profile is here seen as a landscape. Water is flooded from lowest locations in the landscape and progressively fills valleys. The merging of two growing regions defines the boundary between those regions. This is done until water fills the whole image.

From a formal point of view, the Watershed algorithm can be defined in different ways [30]. Definitions for the continuous case as well as for the discrete case exist. We will here focus on the latter since we are working on images that have discrete intensities values. Moreover, two definitions are possible in this case : one by immersion and one by topographical distance [30]. This latter one will be presented [27]. In both cases, a graph formalism is adopted.

A graph G=(V,E,w) is defined by vertices (or nodes) V and by edges $E \subseteq V \times V$ that link vertices between each other. The graph may be directed or not. $N_G(v)$ represents the neighbours of vertice v, i.e. all vertices that are linked to v by an edge. In the case of a weighted graph, each edge (p,q) is associated with a non-negative weight w=d(p,q), where d(p,q) is the distance between non-neighbouring pixels p and q. This distance is defined by the minimum path length among all paths form p to q.

An image or its gradient can be seen as a graph where each pixel is a vertice and is linked in the graph to its neighbouring pixels. Let f be the digital grey value of an image defined for all pixels p in this image. We focus here on lower complete f functions, meaning that each non-minimum pixel has a neighbour of lower grey value. It rejects images where plateaus of pixels with the same intensity are present. The extension of the algorithm to this case can be found in [30]. To build the watershed definition, different concepts need to be defined. This is what is done here under.

The *lower slope LS(p)* of f at a pixel p is defined as the maximal slope between p and one of its neighbours.

$$LS(p) = \max_{q \in N_G(p) \cup \{p\}} \left(\frac{f(p) - f(q)}{d(p,q)} \right)$$

where $N_G(p)$ is the set of neighbours of p and d(p,q) is the distance associated with the edge between p and q. From this lower slope, a cost to go from pixel p to a neighbouring pixel q can be built.

$$cost(p,q) = \begin{cases} LS(p) \cdot d(p,q) & if \quad f(p) > f(q) \\ LS(q) \cdot d(p,q) & if \quad f(p) < f(q) \\ \frac{1}{2}(LS(p) + LS(q)) \cdot d(p,q) & if \quad f(p) = f(q) \end{cases}$$

The set of lower neighbours q of p for which the slope $\frac{f(p)-f(q)}{d(p,q)}$ is maximal (thus equals the value of LS(p)) is denoted by $\Gamma(p)$.

The *topographical distance* along a path $\pi = (p_0, ..., p_l)$ between $p_0 = p$ and $p_l = q$ is defined as

$$T_f^{\pi}(p,q) = \sum_{i=0}^{l-1} d(p_i, p_{i+1}) cost(p_i, p_{i+1})$$

The topographical distance between p and q is then the minimum topographical distance along all paths between p and q :

$$T_f(p,q) = \min_{\pi \in [p \to q]} T_f^{\pi}(p,q)$$

where the set of all paths from p to q is denoted by $[p \to q]$. The path $(p_0, p_1, ..., p_n)$ from $p_0 = p$ to $p_n = q$ is of steepest descent if $p_{i+1} \in \Gamma(p_i)$ for each i=0,...,n-1.

The watershed definition is based on a property of the topographical distance : Let f(p)>f(q), a path π from p to q is of steepest descent if and only if $T_f^{\pi}(p,q) = f(p) - f(q)$. If not we have $T_f^{\pi}(p,q) > f(p) - f(q)$. The paths of steepest descent are thus the *shortest paths* (geodesics) of the topographical distance function. Thereafter, the term of *catchment basin* CB can be defined. Let $f \in C(D)$ have minima $\{m_k\}_{k \in I}$ for some index I, where C(D) is the space of real twice continuously differentiable functions on a connected domain D. The catchment basin $CB(m_i)$ of a minimum m_i is defined as the set of points $x \in D$ which are topographically closer to m_i than to any other minimum m_j:

$$CB(m_i) = \{x \in D \quad | \quad \forall j \in I \backslash \{i\} : f(m_i) + T_f(x, m_i) < f(m_j) + T_f(x, m_j)\}$$

Finally, the watershed definition of f is given by the set of points which do not belong to any catchment basin :

$$Watershed(f) = D \cap \left(\bigcup_{i \in I} CB(m_i) \right)^c$$

where the superscript c refers to the complementary operation. The Watershed transform is thus a mapping between the image pixels (or alternatively their gradient) and a set of indexes that label each catchment basin and the watershed region. Formally, let W be some label with $W \notin I$. The watershed transform of f is the mapping $\lambda : D \to I \cup \{W\}$, such that $\lambda(p) = i$ if $p \in CB(m_i)$, and $\lambda(p) = W$ if $p \in Watershed(f)$.

The major drawback of the Watershed algorithm is that a lot of local minimum are present in gradient images. This leads to over-segmentation since for each minimum a catchment basin will be built. A subsequent step is generally to merge regions together. Mainly two ways are possible to do it : either use the edge information, either build a statistical object model. In most cases, when edge information is used, the idea is to delete edges that are too weak, i.e. have a too low gradient amplitude and do not correspond to a real edge. The other solution is to build a statistical object model [19] : first, cells are modeled with a multivariate Gaussian; then a merging score is computed for each segment depending on its agreement with the Gaussian model and finally, the decision to delete the edge or not is taken by thresholding the score. Another way to do this, is to build a hierarchical merge tree [20]. The first step of this method consists in building a region adjacency graph of the image. Then, a merge tree of a given depth is built for each node. The score of each node of the tree depends on the likelihood for regions to be merged according to some criterion. Finally, the node with the highest score will induce merging (graphical representation in fig. 2.7).

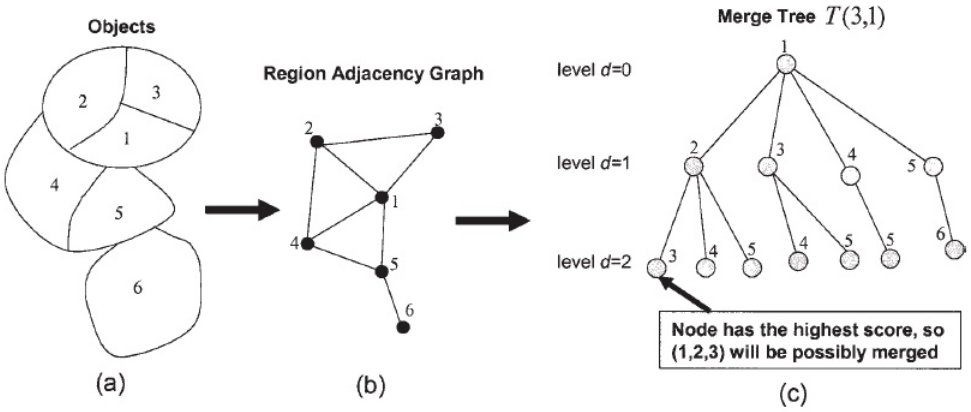


Figure 2.7: Graphical representation of the merge tree method. (a) Watershed segmented regions of the input image, (b) Region adjacency graph built from segmentation, (c) Merge tree built from the region adjacency graph and used for merging the over-segmented regions [20].

Another commonly used solution is to use a marker-controlled watershed algorithm [28]. The idea is to restrict the sources of water to locations where we want an object to be detected. Different methods can be used to perform this : H-minima/maxima, Hough Transform and mathematical morphology are examples. In the scope of this work, morphological reconstruction is used to apply the computed marker on the image to segment. This method is explained in the following section.

Marker-controlled watershed transform

In marker-controlled watershed, locations where water rises are controlled to avoid over-segmentation. In practice, this is done by enforcing pixels of the control marker to be regional minima of the image to segment. Concretely, morphological reconstruction is used to perform it. This algorithm uses an image and a mask as input. The procedure to obtain these inputs is given below.

- Input image :
  1. Modify the image to be segmented such that pixels indicated by the mask have a positive infinite value;
  2. Take the complementary image of the one obtained at previous step;
- Input mask : Impose a positive infinity value at white pixels locations and a negative infinity value at black pixels location.

Morphological reconstruction is then applied with these inputs. Concretely, it consists to apply dilation on the image iteratively, under the constrain to lie underneath the mask. When further dilation ceases to change the image, the process ends. A schematic representation of this algorithm is given in figure 2.8.

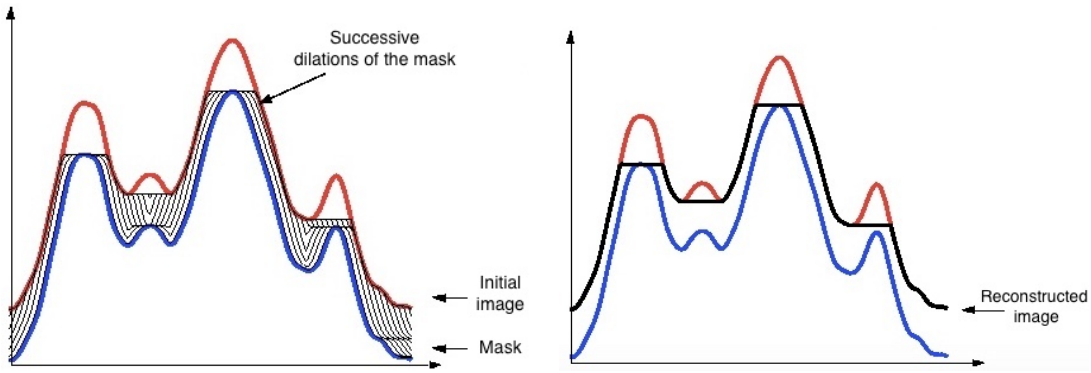


Figure 2.8: Schematic representation of the morphological reconstruction algorithm. The red curve is the input mask and the blue curve is the input image. This algorithm is used to apply our control marker for the watershed algorithm on the transmission image to segment [26].

An example of how the image is modified with this technique is given below (fig. 2.9).

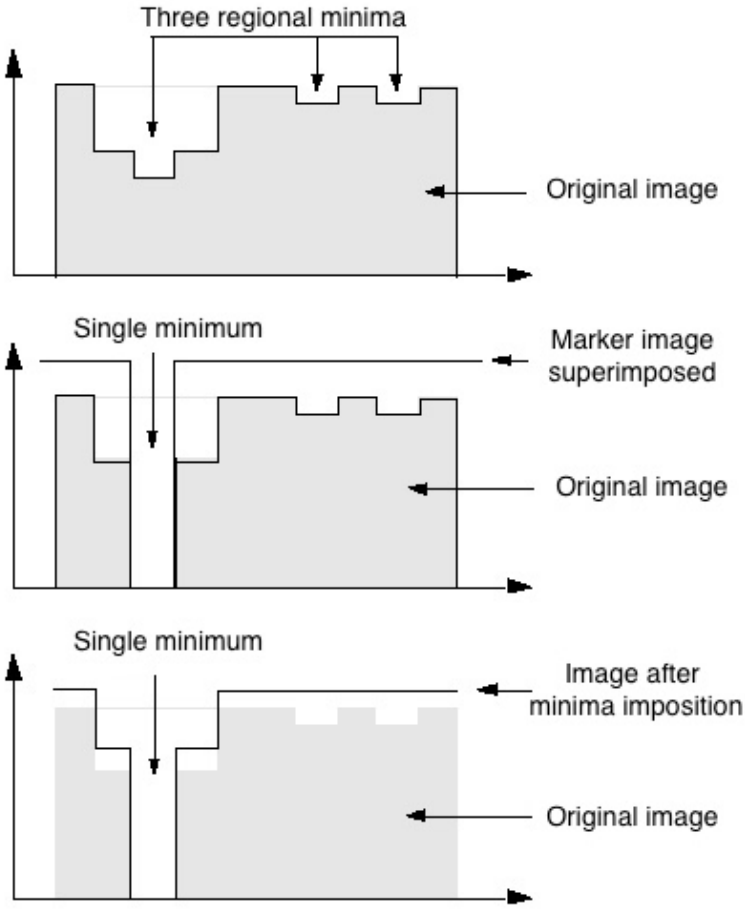


Figure 2.9: Example of how morphological reconstruction can be used to impose a local minimum on an image. This algorithm is used to apply our control marker for the watershed algorithm on the transmission image to segment [26].

2.2.4 Circular Hough Transform

The Circular Hough Transform is relevant for red blood cells detection. Indeed, red blood cells have a well defined circular shape and their diameter is approximately known.

The Circular Hough Transform algorithm is based on edge detection and on an accumulator space [2]. The basic principle is as follows. A circle in an image can be represented by the equation $(x-a)^2 + (y-b)^2 = r^2$. The aim is to find a, b and r for all circles in the image. Edge points, i.e. pixels defining object boundaries, are first extracted from the image. Various methods can be used to perform this. The accumulator space is composed of three dimensions : x and y, the location of the center of the circle and r, its radius. For each edge point, the increment in the accumulator space has a cone shape (fig. 2.10). This cone represents the possible locations for a circle center, if the edge point belongs to the circle. The cone peak is centered at the edge point location and grows upward. This procedure will be repeated for all detected edge points. Finally, the point in the accumulator space that has the larger value will be chosen to be the circle center and the third dimension will give the radius of the circle.

This procedure requires a large storage [42] but is however robust to noise, occlusion and illumination variation [25]. To reduce storage requirements [42] but also enhance efficiency and accuracy, and reduce complexity [2], researchers have adapted this basic principle in various way. First, edge orientation (Kimme et al.) was exploited [2]. Thanks to this information, a smaller part of the accumulator array will be incremented since we know on which side of the edge point the center will be. Going further, Minor and Sklansky [2] only incremented a line perpendicular to the tangent at edge point. This line takes into account all radius length possibilities. A 2-dimensional accumulator space is thus sufficient, reducing the computational complexity. Finally, if a range for the radius value is known, only a segment will be incremented in the accumulator array. Another idea, proposed by Atherton and Kerbyson [1], was to use a complex accumulator array. This algorithm is known as Coherent Circle Hough Transform or Phase Coding. It uses the previous idea and only increments lines in the accumulator array. The real part of the array records the location of the circle center. The phase (from 0 to 2π) records the radius by being proportional to the distance from the edge point. Points coming from the same circle will be in phase at the center location, producing a constructive interference. On the other hand, points coming from noise or edges points not coming from a circle will interfere destructively, leading to a lower peak. The larger peak in the accumulator array is then chosen to be the center of the circle and its phase gives the radius of the circle.

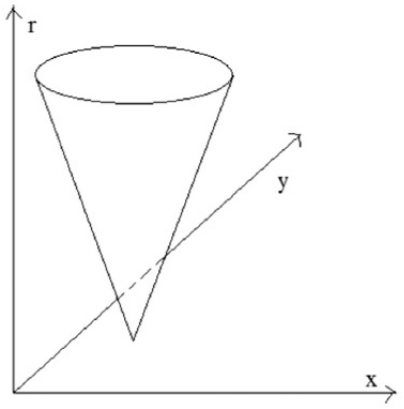


Figure 2.10: Accumulation pattern in the 3D space for a unique detected edge point (from [29])

Mathematically, this is written as follows [1]. Let the edge image be defined by $O(\mathbf{x}) = (O_x(\mathbf{x}), O_y(\mathbf{x}))^T$, where $\mathbf{x}$ is the point location. The edge magnitude is $e(\mathbf{x}) = \|O(\mathbf{x})\|$ and its orientation is $\psi(\mathbf{x}) = arg(O(\mathbf{x}))$, with the unit vector in this direction noted by $\hat{O}(\mathbf{x})$. Initially, the accumulator for the set of points X, in the image I is :

$$H(\mathbf{x}) = 0 \quad \forall \mathbf{x} \in X$$

The accumulator values are then incremented :

$$H_E(\mathbf{x}) = \sum_{\mathbf{x'} \in S(\mathbf{x})} e(\mathbf{x'})$$

where $S(\mathbf{x})$ is the set of points lying in a range between R_{min} and R_{max}, on the line coming from the current edge point. R_{min} and R_{max} are respectively the minimum and maximum radius length provided by the user. Mathematically, this is written as follows :

$$S(\mathbf{x}) = \{\mathbf{w}; \|(\mathbf{I} - \hat{O}(\mathbf{w})\hat{O}^T(\mathbf{w}))(\mathbf{w} - \mathbf{x})\| \leq 1, R_{min} \leq \|(\mathbf{w} - \mathbf{x})\| \leq R_{max}\}$$

In phase coding, the array increment is slightly modified to contain complex numbers and to take the radius of the circle into account.

$$H_c(\mathbf{x}) = \sum_{\mathbf{x'} \in S(\mathbf{x})} e(\mathbf{x'}) exp(-2\pi i u_0 \|\mathbf{x} - \mathbf{x'}\|)$$

where u_0 is fixed such that one wavelength of the sinusoid function fits the range $R_{max} - R_{min}$, i.e.

$$u_0 = (R_{max} - R_{min})^{-1}.$$

Chapter 3

Bright Spots Detection

In this section, the algorithms used to detect bright spots will be described. Strategies are different depending on the image type : confocal images with Theta-labelling to see Cholesterol domains or wide-field images with BODIPY-labelling to see Sphingomyelin domains. Methods will thus be described independently. Two methods were developed for the confocal images while only one was built for wide-field images. Before presenting the algorithms, the prior knowledge that is exploited by each of them will be presented. This prior is common to both image types.

3.1 Prior knowledge

Bright spots are defined by their area and eccentricity. The criteria that are used here to characterize bright spots are an area interval $\mathbb{A}$ and a maximum eccentricity E_{max}. These parameters can be adjusted depending on the aspect of the spots that need to be detected. Values used for results and how they are defined are given in section 5.3. The area interval is given in μm^2, the algorithm translates these values in number of pixel in the image. To do so, the size of the image S in μm and its resolution Res in number of pixels are provided by the user.

3.2 Confocal microscopy images

Two techniques are proposed to detect bright spots in confocal images. The first technique performs an iterative thresholding on the fluorescence image. The second one performs a unique thresholding on a filtered version of the fluorescence image.

3.2.1 Iterative Thresholding method

Iterative thresholding (see explanation in section 2.2.1) is here performed from high intensities to lower ones. Points that correspond to the criterion previously defined can be extracted. For all presented simulations, the maximum and minimum thresholds are respectively set to 0.98 and 0.2 since pixels intensities go from 0 to 1. The number of iterations is set to 50.

3.2.2 Unique Thresholding and Filtering method

The first step consists in filtering the fluorescence image with a Mexican Hat filter (see figure 2.1 in section 2.1 for more details). This Mexican Hat is defined to have a high response to points and a low response to edges. These conditions can be translated in integral conditions as can be seen in figure 3.1. The red integral computed for a horizontal border must be low and the magenta integral computed for a point must be high. The expression adopted here is $\Psi(X) = (2 - 1.475X^2)e^{\frac{-X^2}{2}}$, where $X = \sqrt{\frac{x^2+y^2}{R_{mean}^2}}$. x and y are the coordinates with respect to the center of the pattern. R_{mean} is here the average radius of the points we are looking for, this

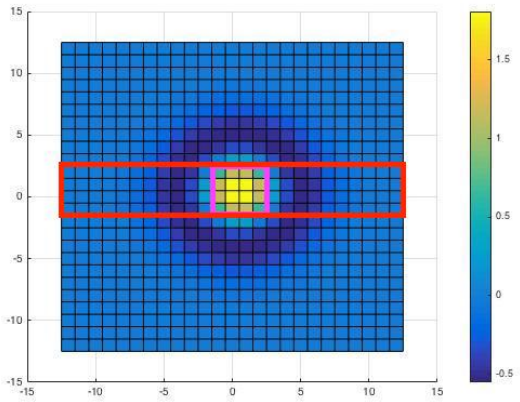


Figure 3.1: Mexican Hat used for bright spots detection in the Unique Thresholding and filtering method :$\Psi(x) = (2 - 1.475x^2)e^{\frac{-x^2}{2}}$. Parameters are chosen to have a low response for cells borders (red integral must be low) and a high response for spots (magenta integral must be high). Point diameter is here of 5 pixels, the red integral is of 5.66 and the magenta integral is of 19.08.

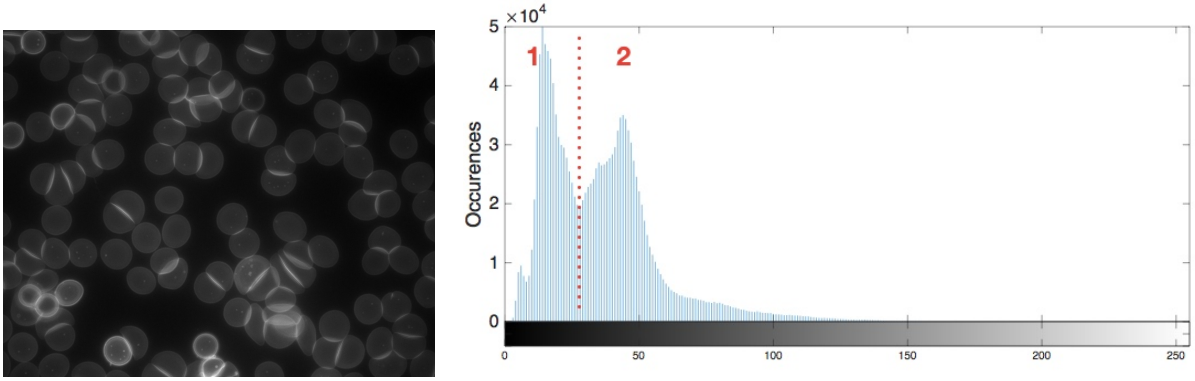
parameter enables to adapt the filter width to the points width. This radius is computed from the area range provided as input : the mean area range is computed and the radius is deduced from this value by assuming points are perfect circles.

The second step is to apply sequential thresholding to determine the best threshold (see section 2.2.1 for more details). The computed properties are the ones used to defined bright spots, i.e. area and eccentricity. The used thresholds go from the maximum of the image intensity to the minimum and the number of iterations n_{iter} can be adjusted. However, in all our simulation it will be set to a value of 100 iterations.

3.3 Wide-field microscopy images

In the case of wide-field images, the contrast between bright spots and the rest of the cell is lower than for confocal images (see figure 3.2(a)). Images are thus filtered with a Sobel operator (see section 2.1 for more details) in order to have images that look like confocal image : bright spots with intensity much higher than the neighbouring cell. However, Sobel filtering increases noise and leads to false detection outside cells. The background of the image will thus be extracted first. Background can be easily detected from histogram analysis of the fluorescence image. Indeed, the light of the whole cell is captured by the microscope in wide-field images, background is thus completely dark and cells are brighter. A unique thresholding will be enough to define background and the used threshold is defined as the minimum location between the two larger maximum in the histogram (see figure 3.2).

Once background pixels have been extracted and the images have been filtered by a Sobel filter, the final step consists in an iterative thresholding method (as in method of section 3.2.1) to select regions that meet requirements to be a bright spot (requirements defined in terms of area range and maximum eccentricity as previously). Number of iterations is again set to 50 and the range for thresholds is [0.4; 0.98]. The lower threshold is higher than previously to be sure to detect only points with a high contrast with respect to cell intensity.



(a) Fluorescence image

(b) Histogram - Region 1 corresponds to background and region 2 to cells

Figure 3.2: Example for fluorescence image in the case of BODIPY-labelling : the analysis of the histogram can be used to define the threshold between cells and background. The threshold between regions 1 and 2 is defined as the minimum location between the two larger maximum in the histogram.

3.4 Spots size computation

For both image types, the way spot sizes are defined is the same. Around each spot centroid, a square with sides $S = 2D$, with D the diameter of spots, is kept. This small image is thresholded with a threshold T defined like : $T = I_{max} - (I_{max} - I_{min}) * \alpha$, where I_{max} and I_{min} are respectively the maximum and minimum intensities of pixels in the kept square. α is determined based on biologists delimitation of spots : $\alpha = 0.7$ for confocal images and $\alpha = 0.5$ for wide-field images. Based on the obtained binary image, the number of pixels belonging to each connected region is computed. If many connected region are observed in the square image, then only the largest one is kept.

3.5 Parameters summary

Here is presented a summary of input parameters that must be provided by the user. They are the same for all methods. The numerical values that were used for simulation and the way there are defined are given in section 5.3.

- Image characteristics :
  - **Res**, the image resolution;
  - **S**, the image size.
- Bright spots descriptors :
  - $\mathbb{A}$, the area range of bright spots ;
  - $\mathbf{E_{max}}$, the maximum eccentricity of bright spots.

Chapter 4

Cells Segmentation

The method used to segment cells is a marker-controlled watershed algorithm. This method is fully explained in section 2.2.3. It has already been used in cell segmentation [4][39][43]. The specificity of our implementation lies in the procedure adopted to define the markers. Depending on the image type, markers will be different. Two methods are presented for the confocal images and one for the wide-field images. Adaptations of each of them in the case of elliptic cells are given. As for bright spot detection, a prior knowledge about cells is first presented.

4.1 Prior knowledge

Cells are defined based on their size and concavity ratio. The concavity ratio CR is defined as follows :

$$CR = \frac{A_{convex} - A}{A_{convex}}$$

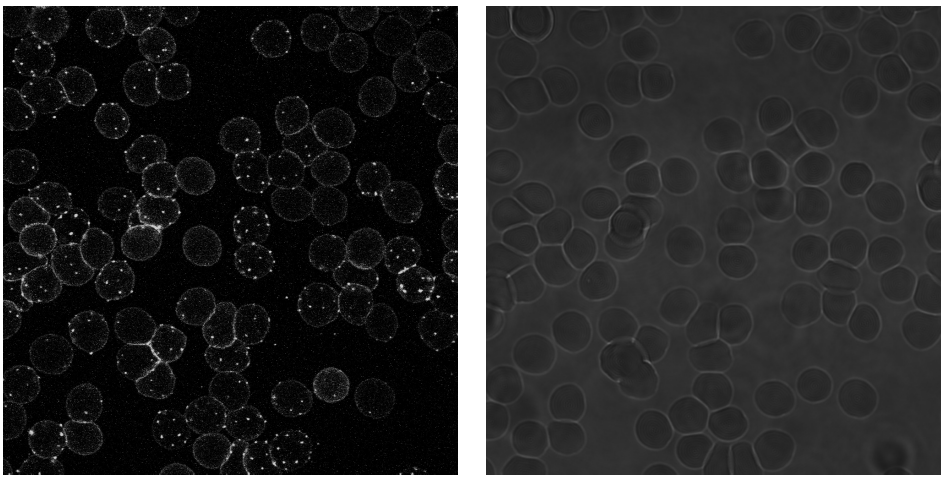
where A is the area of the cell and A_{convex} is the area of the convex hull around the cell. The larger the concavity ratio, the more concave the cell is. An allowed area range $\mathbb{A}$ and a maximum concavity ratio CR_{max} will be used to reject regions that are segmented and do not correspond to cells. Values used for results and how they are defined are given in section 5.3. The area range is given in μm^2, the algorithm translates these values in number of pixel in the image. To do so, the size of the image S in μm^2 and its resolution Res in number of pixels, are provided by the user. Finally, a second shape criterion is used to define cells. The length ratio LR is defined as the ratio between the major and minor axis length of the ellipse that has the same normalized variances as the cell. To ensure cells to have a circular shape, a maximum length ratio LR_{max} will be imposed, knowing that the perfect circle has a length ratio of 1.

In the case of elliptocytosis, cells have elliptic shapes and a different area. Research is still ongoing but globally, we can already say that elliptic cells have a lower area than control cells but the area variance is larger. This is translated by new boundaries for the allowed cells area. Moreover, the concavity ratio is kept as criterion while the length ratio is not used anymore since cells are not circles.

4.2 Confocal microscopy images

Two methods are proposed to segment cells in confocal microscopy images. The first one uses thresholding to determine the seeds for the watershed algorithm, while the second uses the Circular Hough Transform (CHT) (see method explanation in section 2.2.4) to define them. In both cases, the watershed algorithm is then applied on transmission images. Indeed, these images have high intensities values at cells edges, which is required for the watershed algorithm to work.

The fluorescence images do not present such characteristics (see the example provided in figure 4.1).



(a) Fluorescence image (b) Transmission image

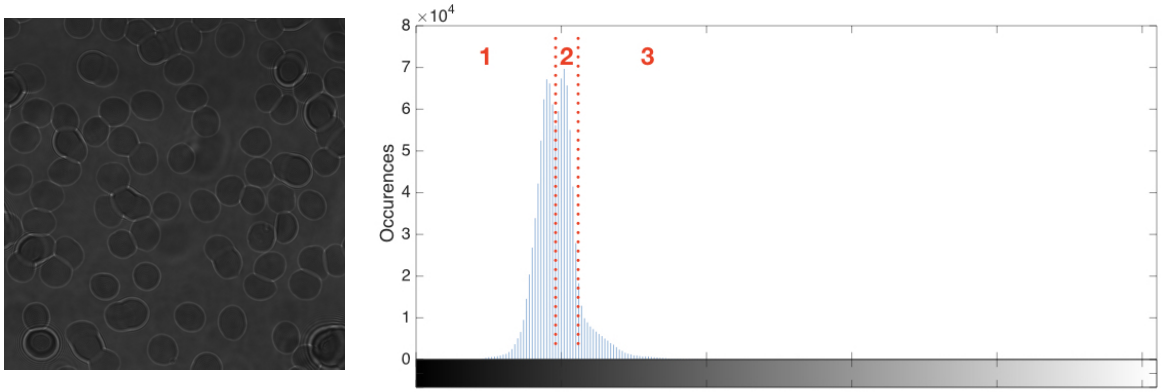
Figure 4.1: Confocal microscopy images of cholesterol domains : the transmission image is used for watershed algorithm since it has high intensity values at cells edges, this is not the case for the fluorescence image.

4.2.1 Thresholding controlled watershed

This method is composed of three steps: firstly, the threshold that isolate cells edges is computed and the marker is built; secondly, the marker is applied on the image to be segmented and thirdly, the watershed algorithm is applied on the new image to produce the final segmentation and wrong cells are deleted.

Threshold selection and marker construction

Based on histogram analysis, a threshold can be found to extract cells that are darker in the image. An example of this is shown in figure 4.2. The first threshold T1 between regions 1 and 2 is defined as the minimum between the two larger maximum of the histogram. The second threshold T2 between region 2 and 3 is defined as the location where the histogram derivative is the lowest. In some cases, the histogram does not show a local minimum between the two maxima to define T1. In these cases, only a maximum is visible in the histogram and this maximum is chosen as T1 threshold.



(a) Transmission image

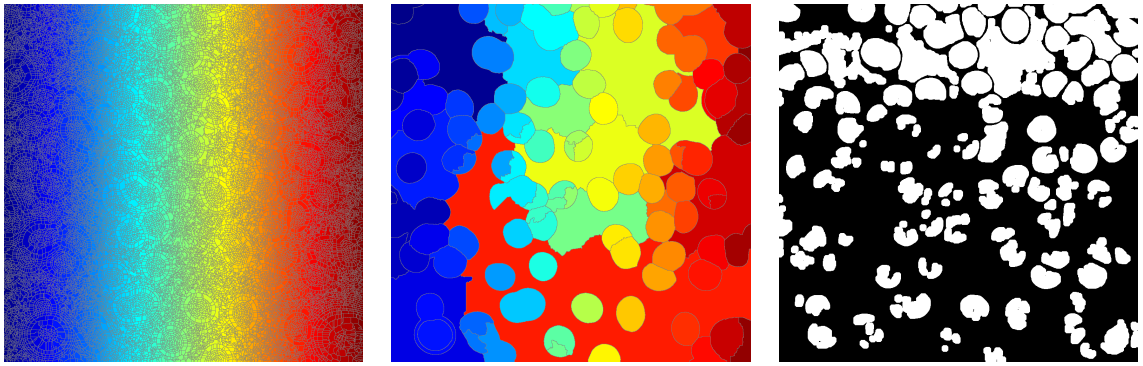
(b) Histogram - Region 1 corresponds to the cells, region 2 to the background and region 3 to the cells borders

Figure 4.2: Example of transmission image in the case of theta-labelling : the analysis of the histogram can be used to define the threshold between the inner part of the cells, their borders and the rest of the image

Pixels with values under the T1 threshold are kept and stored as a mask. An opening is then performed on this mask with a disk structuring element with a radius of 10 pixels. This mask is used as control marker for the watershed algorithm.

Image modification and Watershed algorithm

Morphological reconstruction (see more details in section 2.2.3) is used to impose pixels belonging to the mask as regional minima, and consequently as sources of water in the watershed flooding process. After they have been imposed, the watershed algorithm is applied. This produces the segmentation of the image. The result for one image is given in figure 4.3 and compared to the result without control marker. Clearly, over-segmentation is present without the use of markers and segmentation is strongly improved with them. However, some cells may have been badly delimited and thus cells that do not respect the predefined criterion (see details in section 4.1) are rejected. Background can also be segmented in several regions that are larger than cells, the criterion also enables to reject them.



(a) Watershed segmentation without control markers

(b) Watershed segmentation with control markers

(c) Marker used to obtain the segmentation in panel (b) built from thresholding

Figure 4.3: Example of the impact of control marker used in watershed segmentation

4.2.2 CHT controlled watershed

As for the previous method, this one is composed of three steps : control marker construction, watershed segmentation and wrong cells removal.

Control marker construction by CHT

As already seen previously, cells edges can be extracted by thresholding the transmission image (histogram was shown on figure 4.2). However, thresholding does not provide well defined edges depending on the image illumination. Circular Hough Transform is then used to detect circular shapes. Circles centers will then be chosen as markers for the watershed algorithm. The phase coding technique for CHT (described in section 2.2.4) is chosen since its complex accumulator array speeds up radii computation and it is more robust to noise.

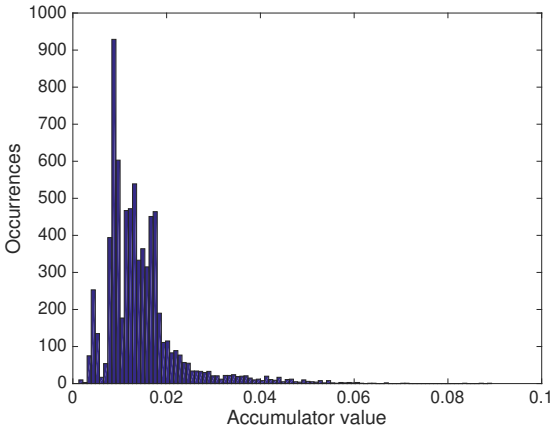


Figure 4.4: Histogram of the accumulator value occurrences. It is used to define the threshold on the accumulator value above which they correspond to a circle. This threshold is defined as the value for which the filtered histogram slope is the lowest multiplied by a factor of 1.5.

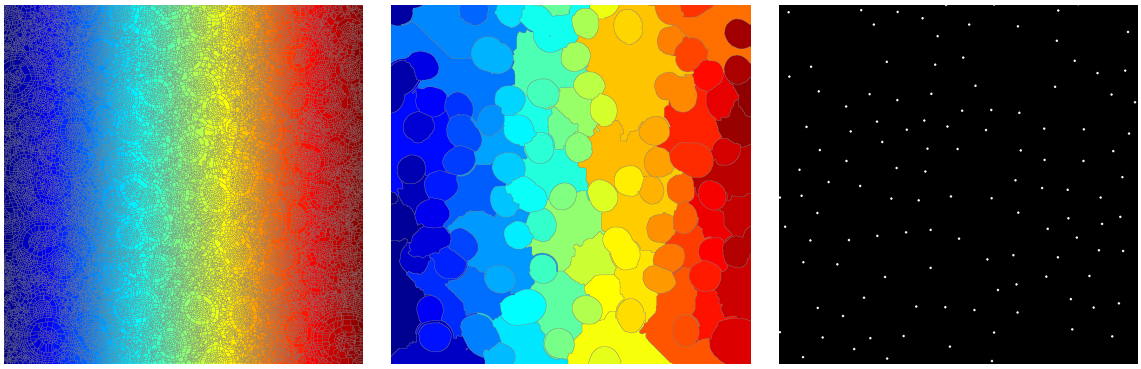
The technique used to determine edge pixels is the Otsu thresholding method already explained in section 2.2.1 [32]. The gradient is computed for all pixels and the threshold on the gradient value is computed to minimize the intraclass variance. Only pixels with a gradient value larger than the threshold will be used for accumulation. A radius range R will also be provided to limit the number of points to be incremented in the array. This one is computed based on the cells area range provided by the user, by assuming cells are perfect circles. Based on the accumulator array, an histogram of the occurrences of each accumulator value is built (see example on fig. 4.4). A lot of accumulator values are really low and does not correspond to cells. A threshold based on this histogram is computed to reject too low accumulation values. The histogram curve is filtered with a all zero-phases digital filtering (window size of 3) and discretely differentiated. The location of the last negative peak of the obtained curve corresponds to the threshold above which occurrences begin to be relatively low. This threshold is multiplied by 1.5 to give the final threshold on the accumulator values. This factor is added to remove more circles because even for metrics higher than the defined threshold, the number of occurrences is relatively high compared to the number of cells in each image. It is of approximately 100 as can be seen in figure 4.4. Only circles with an accumulator value higher than this threshold will be considered as real circles.

Among all circles that are detected, a lot of them are really close to each other. Indeed, since cells are not perfect circles, we often have 5 circles found for one cell. The idea is then to remove circles that are too close to each other and to only keep one of them. Circles that are too close to each other are defined here as circles for which the distance between their centers is smaller than the maximum radius allowed for cells. The circle that is kept is not critical since only the center will be used to determine the control marker of the watershed algorithm. The proposed implementation will keep the circle with the largest accumulation value, which seems logical.

Once all cells centers are found, they are combined in a binary mask : black everywhere and white where a center is located. This mask will be our control marker.

Image modification and Watershed algorithm

The image that is used to apply the watershed algorithm is the Sobel filtered version of the transmission image (the principle of the Sobel filter is explained in section 2.1). This will increase intensity of not well defined edges and avoid water leakage where edge intensity is too low. Next, as for the previous algorithm, morphological reconstruction (see section 2.2.3) is used to impose the regional minima of the control marker on the filtered image. Finally, the watershed algorithm is applied on this modified image to produce segmentation and wrong cells are rejected based on the predefined criterion (see details in section 4.1). Resulting segmentation and marker for one image is given in figure 4.5. The comparison with the segmentation without marker shows the crucial contribution of control marker in segmentation results.



(a) Watershed segmentation without control markers

(b) Watershed segmentation with control markers

(c) Marker used to obtain the segmentation in panel (b), built from CHT circle centers

Figure 4.5: Example of the impact of control marker used in watershed segmentation

4.3 Wide-field microscopy images

For this type of images, a combination of the two techniques proposed for the confocal microscopy images is used. The control marker for the watershed algorithm will be built from thresholding and from CHT results. This improvement is made because in these images, more cells are touching each other and flattened. The CHT will thus detect less cells and seeds will be missing, this is thus solved by adding seeds form thresholding.

Thresholding built control marker

For wide-field images, the fluorescence image can be used to easily extract background pixels. This is made using threshold analysis to determine a threshold between bright cells and black background. The algorithm used to compute the threshold and an example of this were already given in section 3.3 (fig. 3.2). Pixels under this threshold will form a region used as background marker for the watershed algorithm. Concerning cells seeds, iterative thresholding on the transmission image is used to find them. The image used for thresholding is the transmission image where the pre-computed background has been removed. Tested thresholds go from the background threshold to the maximum intensity of the image. The iteration step s can be adapted, however in all our simulation it will be set at a value of 0.5. After each thresholding, regions under the threshold are analyzed and if they meet the geometric criteria they are kept as seed and removed from the image. The iteration can then go further. Criteria for seeds' geometry is related to the cell criteria : the maximum and minimum allowed area are the half of the

maximum and minimum area allowed for cells. A maximum eccentricity of 0.8 is also imposed to avoid structure that do not represent cells, to be used as seeds. Seeds and background are then combined to form a unique control marker.

CHT built control marker

In addition, centers returned by the CHT applied on the fluorescence image are used as marker. The fluorescence image is chosen because it is less noisy than the transmission image and presents a gradient large enough on cells borders. The algorithm is exactly the same as for the confocal images (see section 4.2.2).

Image modification and watershed segmentation

Finally, seeds from thresholding and CHT are combined in a unique control marker. The fluorescence image is used because it is less noisy, however this image does not have a high intensity at edges and the watershed algorithm cannot be performed directly on image intensity values. The differential Sobel operator is thus applied to produce hills at cells borders. The control marker is then used to apply regional minima on the image by morphological reconstruction and the watershed algorithm performs segmentation. As previously, wrongly segmented regions that do not respect the cells geometry criterion are removed (see details in section 4.1).

4.4 Elliptic red blood cells

Confocal images Concerning the thresholding controlled watershed, no modifications need to be done in the algorithm to segment elliptic cells. Only the input parameters that define cells need to be adjusted. For the CHT controlled watershed, the CHT algorithm must be slightly modified since cells are not circles anymore. The idea is to lower the radius range of circles to detect, such that 2 circles are found in each ellipse. The new radius range is defined from the given area range as follows :

$$R = \sqrt{\frac{A}{2\pi}}$$

Previously, circles with centers distant of less than the maximum allowed radius were rejected. However, this criterion must be adapted and we will reject here circles that are less than 2 times the maximum allowed radius apart.

Wide-field images The same adaptation than the one made for the CHT controlled watershed for confocal images is made.

4.5 Irrelevant cells detection

Among detected cells, some of them are not correctly attached to their support. In some cases, one cell is above another one or cells are not in the confocal plane. An example of one of these cases was already given in figure 1.8 of section 1.1.1. These cells appear darker and should be removed for analysis. Their detection will be based on the analysis of the mean and variance of the pixels intensities belonging to each cell, in transmission images. This method is thus valid for both cells types and images. In the 2D space, the RANSAC method will be used to built a model based on the observations of all detected cells in the image. 100 iterations will be made and for each of them, half the number of cells will be used to build a Gaussian model. Cells are randomly chosen. For each model, the number of outliers is defined as points located outside the $[\mu - 2\sigma, \mu + 2\sigma]$ interval, for each dimension. The chosen model is the one with maximum 10% of

outliers and with the largest probability value for each point to belong to the model. Outliers of the chosen model correspond to cells with an aspect different from the majority of the other ones. They can then be removed from segmentation.

4.6 Parameters summary

Here is presented a summary of input parameters that must be provided by the user. They are the same for all methods. The numerical values that were used for simulation and the way there are defined are given in section 5.3.

- Image characteristics :
  - **Res**, the image resolution;
  - **S**, the image size.
- Cells descriptors :
  - $\mathbb{A}$, the area range of cells;
  - $\mathbf{CR_{max}}$, the maximum Convexity Ratio of cells;
  - $\mathbf{LR_{max}}$, the maximum Length Ration of cells, only used for healthy cells.

Chapter 5

Validation method

In this section, the algorithms validation will be presented. Ground truth images will be detailed. Validation metrics and how they are computed will be explained. Metrics for the lipidic domains analysis will also be defined. Finally, used values of input parameters will be given.

5.1 Validation metrics

The algorithm validation is based on the manual annotation of the different image types (fig. 5.1). The annotation consists in marking the cells of interest with a blue dot, this dot is placed as much as possible in the center of the cell. Moreover, bright spots are marked with a white dot. Note that the validation does not rely on all cells of the image, i.e. not all cells are marked with a blue dot. This is due to the fact that some cells are really close to each other and their boundaries are difficult to determine visually, making the assignment of bright spots to a cell ambiguous. These cells are thus discarded for validation because there are not used by biologists. Moreover, manual segmentation of individual cells has not been considered for algorithm validation.

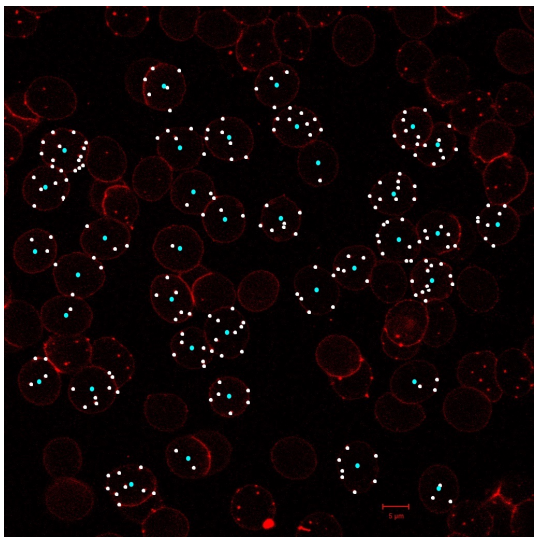


Figure 5.1: Example of annotated image

Validation will be made on four sets of five images. We have two sets of BODIPY labelled images (sphingomyelin domains) : one set of healthy cells and one of elliptic cells, and two sets of Theta labelled images (Cholesterol domains), again one of healthy cells and one of elliptic ones. Samples come from the CELL unit of the *De Duve Institute*, courtesy to D. Tyteca.

5.1.1 Segmentation

To assess segmentation quality, the percentage of blue dots that can be assigned to a segmented cell will be computed. This defines a cell detection rate. A cell is assigned to a blue dot when the blue dot to cell centroid distance is lower than the mean cell radius computed on this image. The number of detected cells is also given and a joint detection percentage is computed to compare method results. This joint percentage is defined as the percentage of cells detected by both methods with respect to the highest number of detected cells. This gives an idea of the number of cells that are detected but not if they are correctly segmented. To assess this, we will compute the percentage of annotated points that are part of the annotated cells. This will be called the shape coefficient. Mainly in theta-labelled images, bright spots are located in the cell periphery. To ensure that bright spots located on the watershed borders are assigned to the correct cell, the computed segmentation is dilated with a disk structuring element with a radius equivalent to the mean radius of bright spots. Dilation is performed iteratively so that, at each step, cells merging can be avoided by recording edges between cells. At each step, all cells are dilated of one pixel and the overlapping regions are removed to keep regions isolated. This is done many times until complete dilation is performed. The dilated segmentation will be used for all other metrics computations, except for their area evaluation.

Cells that are darker (badly attached to their support or one above another) are not taken into account by biologists and thus not selected for ground truth. Further results are thus not affected by their removal since we only compare cells selected by biologists. Moreover, for the analysis of cells properties in section 7, all cells were taken into account. This does not influence results since only a small part of cells are removed compared to the large number of cells used to compute these properties.

5.1.2 Bright spots detection

Since our algorithms will detect all bright spots in the image and the annotation only focuses on some cells, only a detection rate can be extracted from this information. Indeed, a percentage of false detection cannot be built consistently. Two points will be considered to be the same if their centers distance is less than their mean prescribed diameter multiplied by a factor of 0.7 to support manual matching. Segmentation and spots detection can then be combined to give more precision on the algorithm performances. Different metrics will be computed :

- Detection rate for the whole image : in the segmented cells kept by the annotation, the percentage of points that are correctly detected;
- False positive rate for the whole image : the percentage of points detected in the segmented cells kept in the annotation that were not manually detected;
- From above defined metrics, a ROC curve can be defined for thresholding techniques. For different threshold values, the detection rate is plotted with respect to the false positive rate.
- Detection rate per cell : the detection percentage of each annotated cell. These values will be summarized in an histogram.
- False positive rate per cell : the false positive percentage for each annotated cell. Again, these values will be summarized in an histogram.

5.2 Domains Analysis metrics

Concerning the analysis of lipidic domains, different metrics will be computed : there are listed hereunder.

- The **number of bright spots per cell** is computed only for annotated cells. Values are summarized in an histogram. As a second step, the number of bright spots is normalized by the maximum number of bright spots in a cell to produce a normalized histogram. This enables to compare methods regardless the number of detected spots;

- The **density of spots** is computed as the number of spots divided by the total area of cells annotated in the image. Densities in healthy cells and elliptic ones are then compared by computing the ratio between them. To compute this ratio, all detected cells are taken into account.

- The **cumulative number of detected spots** is plotted with respect to the distance to the cell center. To be able to compare curves returned by different algorithms and by the ground truth, this curve is normalized by the total number of detected cell in each case. Again, only spots in annotated cells are used to build this curve;

- The **percentage of bright spots located at the center of cells**. To compute this value, cells regions have been eroded with a disk structuring element of radius equal to the bright spots diameter. This enables to remove spots on the cells periphery. The percentage of kept spots with respect to the total number of spots is then computed. To compare results in healthy and elliptic cells, the ratio of their percentage is computed. To compute this ratio, all detected cells are considered;

- The **frequency histogram of spots size**. For cholesterol domains, all detected spots in segmented cells are used to build the histogram. On the contrary, for sphingomyelin domains, since their number is much lower and the number of false positives high (as we will see later), only correct detections are used to build the histogram. For cholesterol domains, it was not necessary. Indeed, because of the high amount of detected spots, the small number of false positives do not influence the statistics.

- The **surface coverage** of spots is the ratio between the total area of spots and the total area of cells for one image. All detected cells are used to compute this value.

5.3 Used Parameters

Most of the key parameters involved in our algorithms are directly derived from biologists knowledge. Concerning bright spots detection, numerical values for $\mathbb{A}$, the area range and E_{max}, the maximum eccentricity are provided by the user. Parameters are different depending on the image under analysis because spots appearances are quite different. Cholesterol domains (in confocal images) have a quite large area range that is valid for healthy cells as well as for elliptic cells. However, Léonard et al. [23] (see also figure 7.6(c)) have shown that the distribution is not gaussian so the range cannot be built from mean and standard deviation values. It will be chosen to cover a majority of possible areas. The maximum allowed eccentricity[1] is set close but smaller than one because a lot of points are located on the cell periphery and are flattened. For sphingomyelin domains (in wide-field images), the area range can be considered the same as the cholesterol ones. However due to their more central positioning, the eccentricity criterion can be more limiting. Used values are given in table 5.1.

For watershed segmentation, $\mathbb{A}$, the cells area range; CR_{max}, the maximum Convexity Ratio; and LR_{max}, the maximum length ratio are given as input. What is proposed for area range definition is to suppose a Gaussian distribution for their area and to take the 99.7% interval $(\mu \pm 3\sigma)$. In most cases, wrong segmented regions have a larger or smaller area and if it is not the

[1]The eccentricity E of a circle equals zero. For ellipses, $0 < E < 1$ and if E=1, we have a parabola.

case, the shape criterion (based in Convexity Ratio and Length ratio) is enough to discard them. A large interval is thus appropriate to keep the maximum number of cells. However, for elliptic cells the assumption for Gaussian distribution is less valid and the computed lower bound is very small (4 μm^2) and should not allow rejection of small regions not corresponding to cells. This lower bound was thus increased to 20 μm^2. The other parameters are fixed based on empirical evaluation but a deeper analysis should allow to have more precise estimation for them. Values are given in table 5.2.

Finally, in our dataset, for confocal images, 1024 pixels were corresponding to 102.04 μm, while for wide-field images 1376 pixels correspond to 124.94 μm.

	Confocal images	Wide-field images
$\mathbb{A}[\mu m^2]$	[0.1; 0.8]	
E_{max}	0.9	0.5

Table 5.1: Numerical values of parameters for bright spot detection

	Healthy cells	Elliptic cells
$\mathbb{A}[\mu m^2]$	[40; 90]	[20; 60]
CR_{max}	0.2	0.2
LR_{max}	1.4	/

Table 5.2: Numerical values of parameters for cells segmentation

Chapter 6

Algorithms validation

This chapter presents the results obtained for confocal images and wide-field images, for segmentation and bright spots detection. Results are compared with ground truth, analyzed and discussed.

6.1 Confocal images

6.1.1 Cells Segmentation

Two methods were proposed to segment cells in confocal images : both are marker controlled watershed algorithms. One is controlled by thresholding, the other by Circular Hough Transform (CHT) analysis. A comparison between them will be first presented and then their performance regarding the ground truth will be assessed.

Visually[1], segmentations are quite similar (figs. 6.1 and 6.2) and show the same properties. First, cells that are too close to borders are not detected, either because their area is out of the prescribed range, either because the center of the cell is out of the image and thus not detected by CHT for the CHT controlled segmentation. Missing these cells is not a major drawback since each image shows enough cells for analysis. Moreover, these cells even if there are not complete could be used for the spots density analysis as well as for their surface coverage. However, for the radial distribution evaluation these cells would be anyway useless.

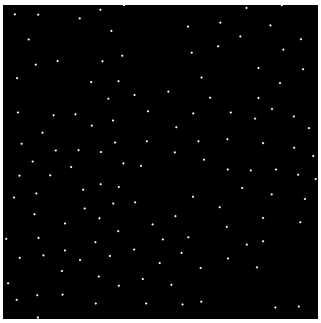
Secondly, missing cells in the inner part of the image are due to over-segmentation (cell divided in different watershed regions) or under-segmented (cells are merged together). In both cases, this is due to incorrect seeding : two seeds are placed in the same cell or the seed crosses two cells. Indeed, once the seed is correctly placed, watershed performs well due to well defined cells edges. Except in some particular cases where cells stick to each other, the edge between them is missing or when a cell is too flatten its edges are less clearer. However, these cells are also discarded by biologists for analysis. A solution to incorrect seeding is to use graph-cuts that allows multiple seeding in the same cell [6]. Another idea is to generate too much seeds and then merge cells based on their shape and intensities values [39]. Concerning seeds that are placed on cells edges, the intensity at seeds location could be analyzed to reject or cut incorrect seeds. Finally, seeds present outside cells are not critical since they will define large regions because there are not surrounded by edges. These regions are removed based on the shape and size criterion on cells.

Concerning methods comparison, a large part of cells are detected by both methods but each method detects cells that the other one has not detected. More quantitatively, for healthy cells (fig. 6.3(a)), the CHT controlled watershed detects more cells and in average 72% of cells detected by the CHT controlled watershed are also detected by the thresholding controlled one. For

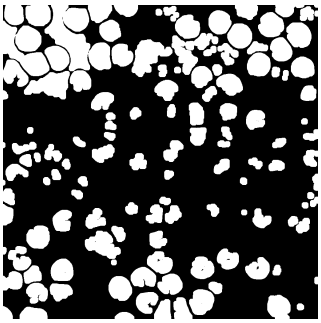
[1] Additional results images at each step are provided in appendice A for both methods and both image types.

elliptic cells (fig. 6.3(b)), the thresholding controlled watershed detects more cells. In this case, the percentage of jointly detected cells is higher (78%). CHT controlled watershed seems thus better suited for healthy cells detection, while thresholding controlled watershed is better suited for elliptic cells detection. However, a large number of detected cells reflects neither the quality of the segmentation, neither the false positive detection rate. Results are thus compared with ground truth. For healthy cells, the detection rate is higher with the CHT controlled watershed method : it is of 77% (fig. 6.4(a)). On the contrary, for elliptic cells the Thresholding controlled watershed performs better with 66% of detection (fig. 6.4(b)). This result can be explained by the fact that the CHT controlled watershed detects circles to define marker : it can be thus easily understood that it performs better for healthy and thus circular cells than for elliptic ones. On the contrary, thresholding controlled watershed is not shape specific. In both cases, detection rate is not very high. Concerning the CHT controlled watershed, this could be due to a too high threshold on accumulator value to keep circles. However, analysis shows that this threshold has a minor impact on the detection rate. Indeed, if too much circles are kept, cells will be over-segmented due to many seeds in one cell. On the contrary, if too low circles are kept, some cells have no seeds and are thus not detected. Concerning the thresholding controlled watershed, high performances were not expected due to the simplicity of the method. If images were uniform in cells pixels intensity, results should be higher. However, this cannot be guaranteed for all images.

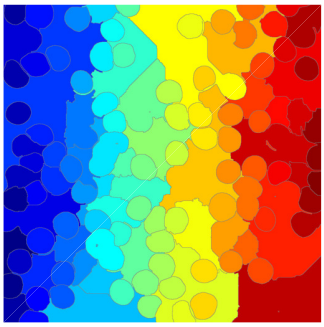
The cells detection rate analysis does not provide information about the shape of the segmented regions. However, we can see (fig. 6.1) that cells shapes are well preserved by both methods. The analysis of the shape coefficient for each method (fig. 6.5) shows that both for healthy cells and elliptic ones, the CHT controlled watershed provides better segmented cells. For both methods, performances are better for healthy and thus circular cells. Since CHT controlled segmentation shows better performances than the thresholding controlled watershed, the former method will be used for the rest of the analysis. Indeed, shape information is crucial to know where bright spots are located in the cells, which is of strong interest for biologists. It is thus preferable to have a lower amounts of detected cells that are well segmented than too much badly segmented cells. More quantitatively, shape coefficient are not close to 1, despite good visual results. This is due to the fact that even spots of cells that were not detected are used to compute it. If we suppose that spots are equally spread among cells, we can see that the shape coefficients are generally only slightly under detection rate. This reflects thus a good segmentation for cells that are detected.



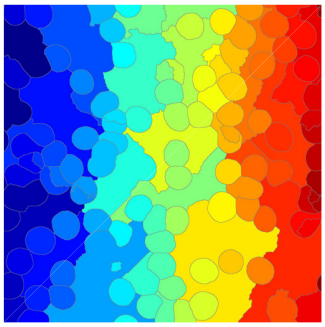
(a) Markers for the CHT controlled watershed



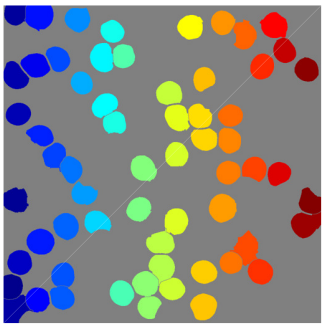
(b) Markers for the thresholding controlled watershed



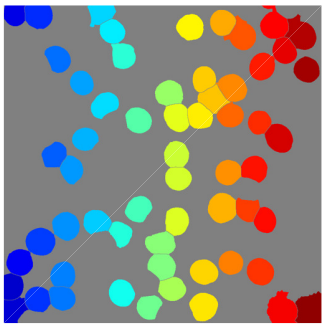
(c) Segmentation image obtained with the CHT controlled watershed algorithm



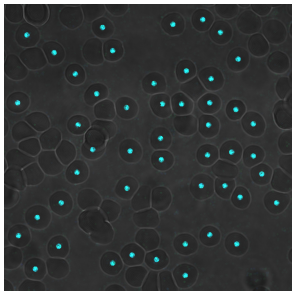
(d) Segmentation image obtained with the thresholding controlled watershed algorithm



(e) Segmented cells with the CHT controlled watershed algorithm

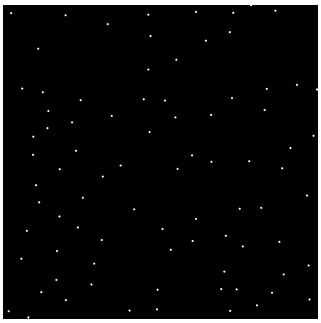


(f) Segmented cells with the thresholding controlled watershed algorithm

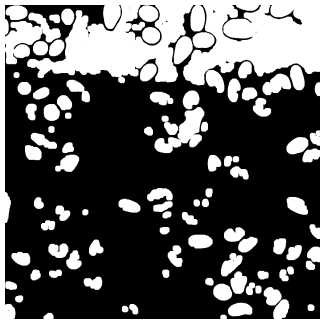


(g) Initial transmission image with annotated cells

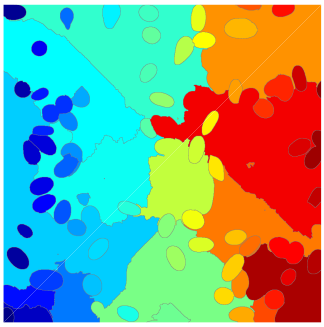
Figure 6.1: Segmentation results for confocal images of healthy cells, with the two proposed methods : left column is for CHT controlled watershed and right column is for thresholding controlled watershed. The image to segment, the markers, the segmentation results as well as the regions kept from the segmentation and that correspond to cells are shown.



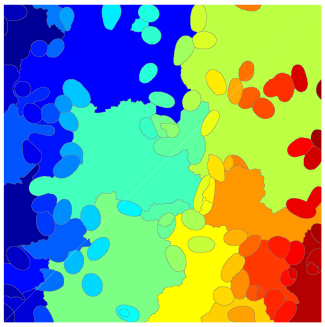
(a) Markers for the CHT controlled watershed



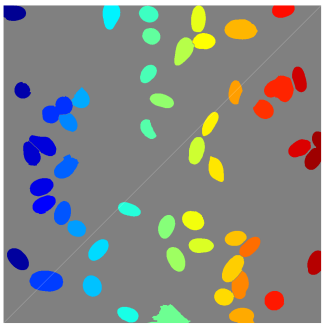
(b) Markers for the thresholding controlled watershed



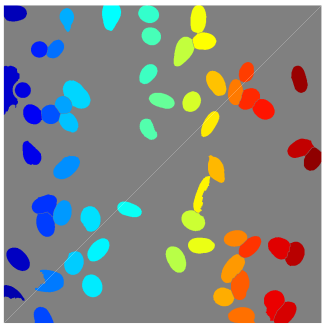
(c) Segmentation image obtained with the CHT controlled watershed algorithm



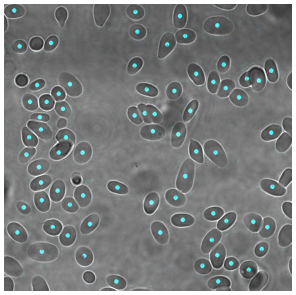
(d) Segmentation image obtained with the thresholding controlled watershed algorithm



(e) Segmented cells with the CHT controlled watershed algorithm

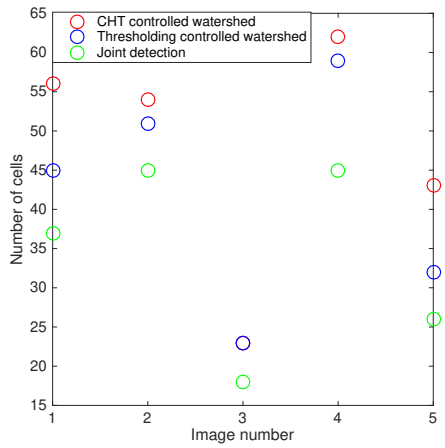


(f) Segmented cells with the thresholding controlled watershed algorithm

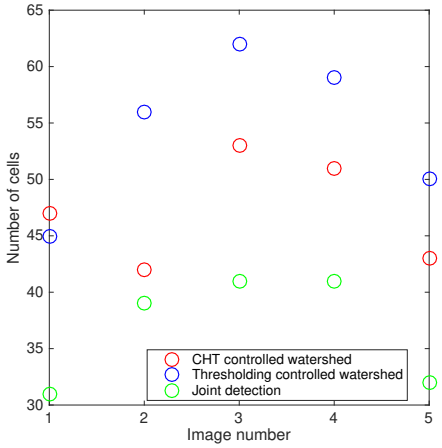


(g) Initial transmission image with annotated cells

Figure 6.2: Segmentation results for confocal images of elliptic cells, with the two proposed methods : left column is for CHT controlled watershed and right column is for thresholding controlled watershed. The image to segment, the markers, the segmentation results as well as the regions kept from the segmentation and that correspond to cells are shown.

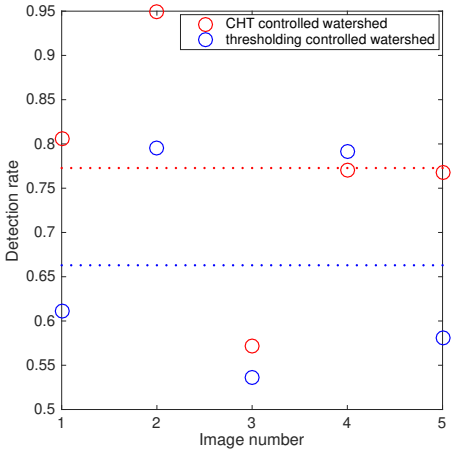


(a) Healthy cells. Joint percentage = 0.721 ± 0.0084

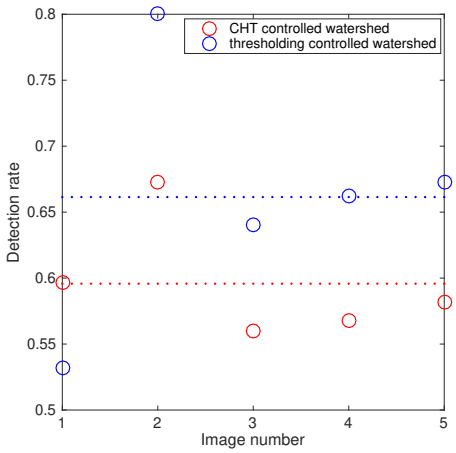


(b) Elliptic cells. Joint percentage = 0.782±0.0096

Figure 6.3: Number of cells detected with each method and for each image : (a) healthy cells, (b) elliptic cells.

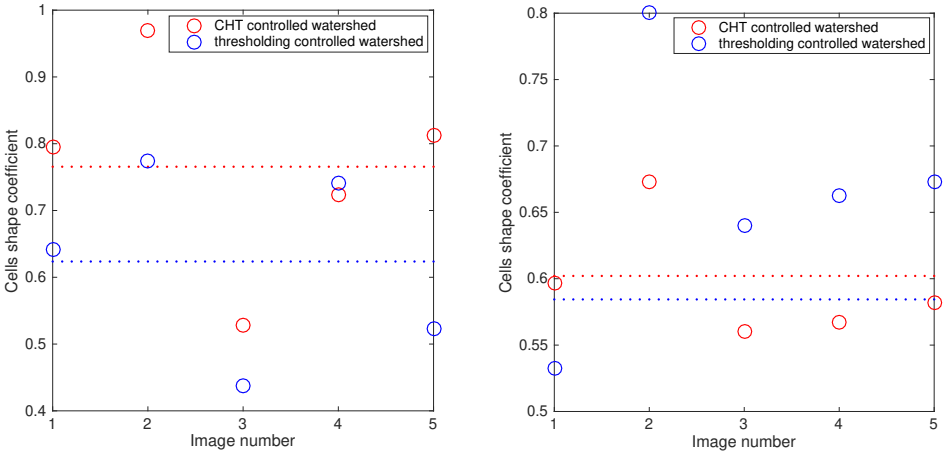


(a) Healthy cells. Mean detection rate for CHT controlled watershed = 0.773±0.018 ; for Thresholding controlled watershed = 0.663±0.015.



(b) Elliptic cells. Mean detection rate for CHT controlled watershed = 0.596±0.002 ; for Thresholding controlled watershed = 0.664±0.0091.

Figure 6.4: Detection rate for each method and for each image : (a) healthy cells, (b) elliptic cells.



(a) Healthy cells. Cells shape coefficient for CHT controlled watershed = 0.765±0.0256; for thresholding controlled watershed = 0.6236±0.0203

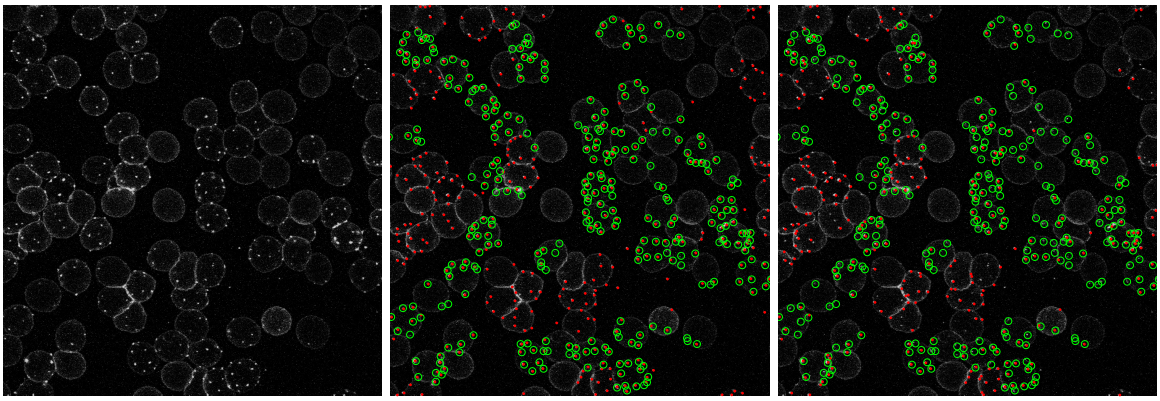
(b) Elliptic cells. Cells shape coefficient for CHT controlled watershed = 0.602±0.0026; for thresholding controlled watershed = 0.584±0.0283

Figure 6.5: Cells shape coefficient for each method and for each image : (a) healthy cells, (b) elliptic cells.

6.1.2 Bright spots detection

Two methods are proposed for the bright spots detection. One is based on iterative thresholding while the other is based on image filtering and a unique thresholding. A comparison between them will be given and their performances will be assessed. From a preliminary analysis of figure 6.6, we can say that both techniques miss some bright spots. Moreover a lot of points not belonging to ground truth are also detected. This is due to the fact that not all cells are annotated by biologists. Figure 6.7 shows a comparison of points detected by both methods. They have a lot of detections in common : bright spots detected by the iterative thresholding method are nearly all detected by the Unique thresholding and filtering method. Moreover, this second method detects much more spots. Note that similar images for elliptic cells are provided in appendice B.

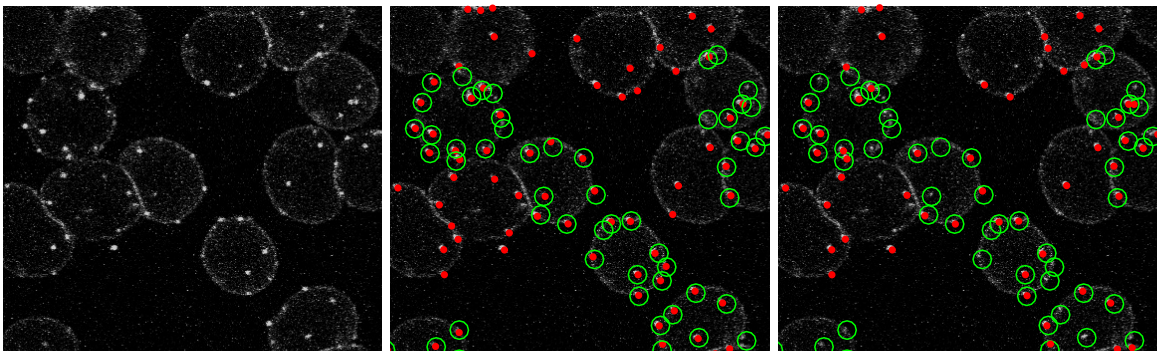
Concerning, the unique thresholding and filtering method, we can analyze how it behaves depending on the chosen threshold (fig. 6.8). The right threshold to minimize the percentage of points that do not correspond to the right geometry is computed, and then modulated by a coefficient. A higher threshold (fig. 6.8(d)) leads to less detection and points are thus missing. However, some points are already false positives. By lowering the threshold, more and more points (panels (b) and (c)) are detected : some are part of ground truth but others are not. Finally, even with the lowest shown threshold (panel(b)) some points manually detected are not detected by the method.



(a) Initial fluorescence image

(b) Unique thresholding and filtering method

(c) Iterative thresholding method



(d) Initial fluorescence image : zoomed version

(e) Unique thresholding and filtering method : zoomed version

(f) Iterative thresholding method : zoomed version

Figure 6.6: Bright spots detection results for both methods. Red dots are detection results and green circles are ground truth. The upper row shows total images while the lower row shows zoomed versions of images.

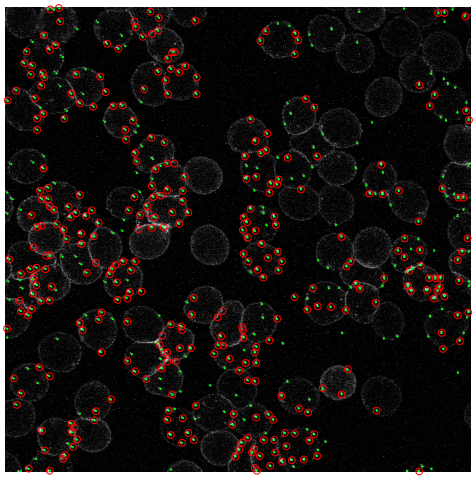
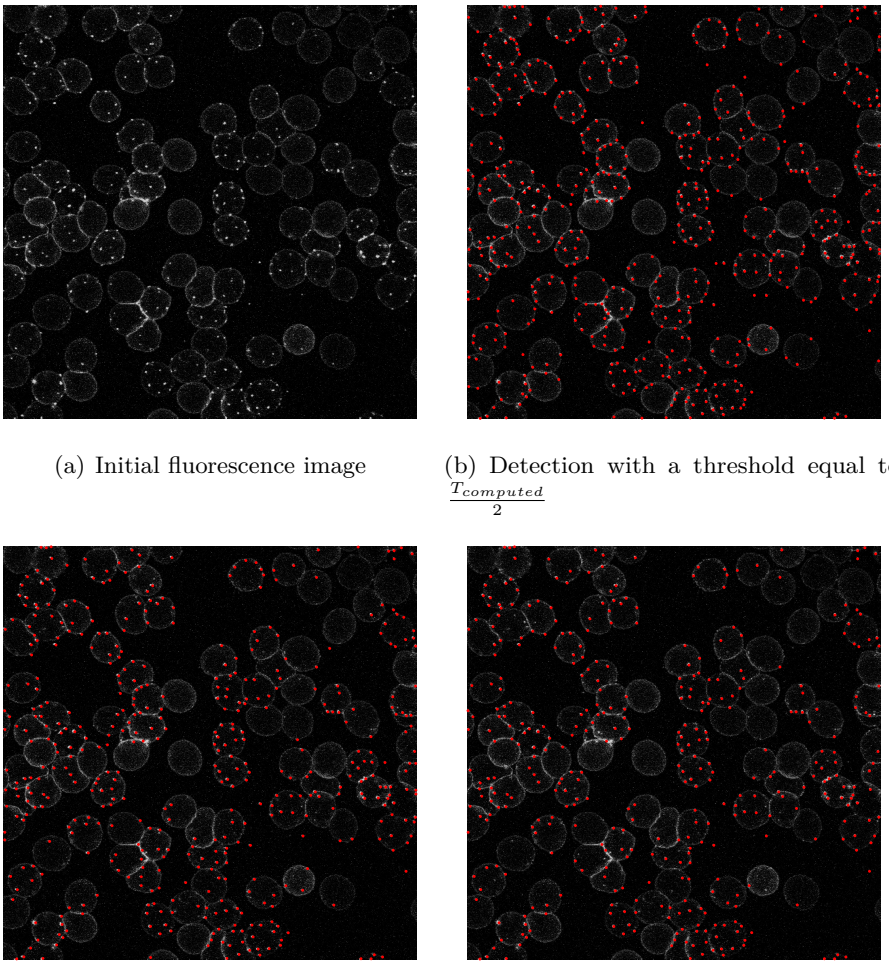


Figure 6.7: Comparison between both methods - Green dots : Unique thresholding and filtering method results; red circles : Iterative thresholding method results.



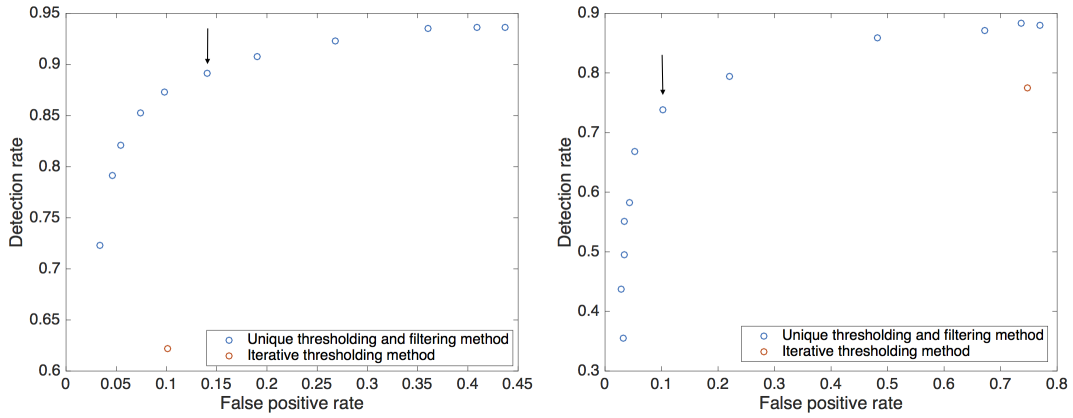
(a) Initial fluorescence image

(b) Detection with a threshold equal to $\frac{T_{computed}}{2}$

(c) Detection with a threshold equal to $T_{computed}$

(d) Detection with a threshold of $\frac{3*T_{computed}}{2}$

Figure 6.8: Unique thresholding and filtering method : bright spots detection results with different thresholds



(a) Healthy cells

(b) Elliptic cells

Figure 6.9: ROC curve for the bright spot detection methods on confocal images.

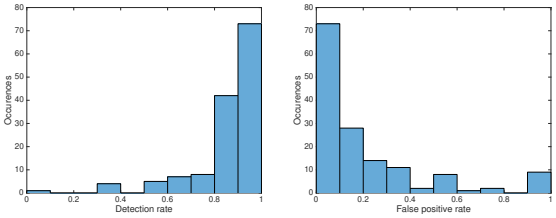
To be able to have a more quantitative analysis, the cell segmentation must be taken into account to be able to only look at points located in cells chosen by biologists. This allows to compute a false positive rate. For the Unique thresholding and filtering method, a ROC curve can be drawn by varying the used threshold. This is shown in figure 6.9(a) for healthy cells and in figure 6.9(b) for elliptic ones. A point for the performances of the Iterative thresholding method is also added for comparison. The best method is the one for which the detection rate is high and the false positive rate is low, corresponding to points in the left upward part of the graph. Regarding to this criterion, the Unique thresholding and filtering method performs better. However, even with a large false positive rate, the detection rate never reaches 100% reflecting that some bright spots will always be missing. The iterative thresholding is in comparison less efficient. Missing detections are mainly occuring for low intensities spots. A solution could be to lower the minimum threshold. However, the minimum threshold cannot be lowered otherwise every small intensity increases in the image (due to cells edges for example) will also be chosen as spot. This will also increase the false positive rate, something we want to avoid. Performance of this method can thus hardly be increased since it is not enough shape specific. The Iterative thresholding method is thus less accurate since for the same detection rate, the false positive rate is higher.

A comparison between performances for healthy cells and elliptic cells can also be done. We can see that performances of the Unique thresholding and filtering method are better for healthy cells, since for the same detection rate, the false positive rate is lower (ROC curve shifted to the left). This is explained by the fact that for elliptic cells, spots are less well shaped. Some of them are larger and also more flattened. The Mexican hat filtering is thus less suited for such spots. It could be interesting to use different filter sizes to be able to detect larger spots. Concerning their shape, improvement is more difficult since to respond to elliptic shapes, the orientation of the filter must be chosen. We do not know which orientation the spots have and thus many filters must be tested, increasing computational time. When looking at the performance of the iterative thresholding method, drawing a conclusion is more difficult since only one point in the ROC curve can be obtained. Nevertheless, we can see that performances for healthy cells and elliptic cells are strongly different. False positive rate is higher for elliptic cell, this is explained by the fact that intensities in these images are higher. The minimum used threshold should thus be increased or in general adapted to the intensities histogram, which is something that was not implemented.

Concerning the Unique thresholding and filtering method, an optimal threshold can be chosen based on the ROC curve. Depending on biologists requirements, we can allow more or less false positives. In our case, since bright spots need to be counted, a compromise must be found between correct detections and false positives. For the following analysis, we will choose the threshold that is located, as already said, the most in the upper left corner of the curve. For healthy cells, $T_{best} = 0.8 * T_{computed}$ and for elliptic cells, $T_{best} = 0.6 * T_{computed}$. The fact that this computed threshold is not optimal indicates that the criterion to define what a spot is, do not support ground truth. By taking a closer look to figure 6.6, we can guess that undetected spots are mainly small spots. Based on the spots size analysis that will be made in section 7, we could see if the chosen criterion was coherent or not.

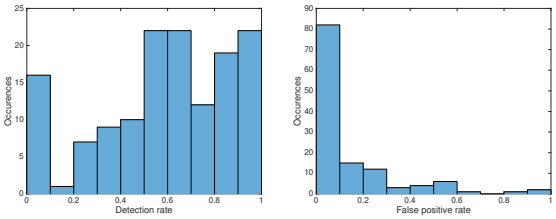
To grasp more easily methods performances, the histograms of detection rates and false positive rates per cell for each method and each cell type (fig. 6.10 and 6.11) are analyzed. Globally, detection rate histograms have an increasing exponential shape, while false positive rate histograms have a decreasing exponential shape. This reflects good performances of the algorithm : a lot of cells have a detection rate of one and a false positive rate of zero. However, some histograms do not follow this trend. For healthy cells first, panel (c) of figure 6.10 shows that more than 15 cells have a detection rate of zero : the iterative thresholding method is thus

missing a lot of detections, as already seen with the ROC curve (fig. 6.9(a)). Concerning elliptic cells, as already seen previously with ROC curves (fig. 6.9(b)), panel (d) of figure 6.11 shows that the false positive rate histogram has a high number of cells with a false positive rate of one. Moreover, this analysis enables to see that we are not in a binary case where some cells have a detection rate close to one, while some others are very close to zero. Instead, errors are regularly spread over all cells.



(a) Detection rate histogram : Unique thresholding and filtering method

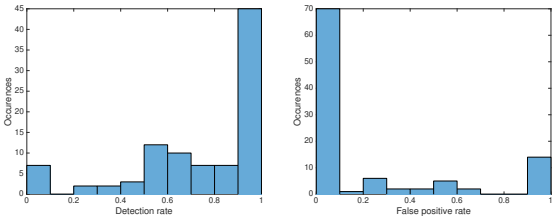
(b) False positive rate histogram : Unique thresholding and filtering method



(c) Detection rate histogram : Iterative thresholding method

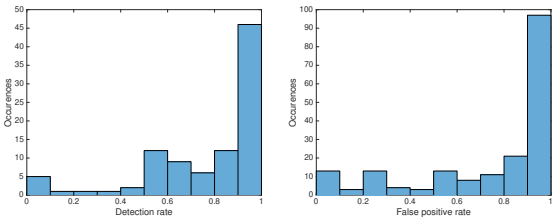
(d) False positive rate histogram : Iterative thresholding method

Figure 6.10: Analysis of the detection rate and false positive rate per cell for healthy cells.



(a) Detection rate histogram : Unique thresholding and filtering method

(b) False positive rate histogram : Unique thresholding and filtering method



(c) Detection rate histogram : Iterative thresholding method

(d) False positive rate histogram : Iterative thresholding method

Figure 6.11: Analysis of the detection rate and false positive rate per cell for elliptic cells.

6.1.3 Partial conclusion for confocal images

Concerning cells segmentation, analysis shows that CHT controlled watershed has a higher detection rate than Thresholding controlled watershed for healthy cells. For elliptic cells, it is the reverse situation. However, for both image types, the detection rates nearly reach 77 and 66% depending on cells type. This is mainly due to incorrect cell seeding. Either many seeds are present in one cell, a solution for this could be to merge regions together. Either seeds are placed on edges, many cells are thus merged together. The intensity of marker location could be analyzed to reject these seeds or to cut them to have one seed in each cell. In terms of cells shapes, CHT controlled watershed regions shapes are more conform to ground truth. However, both methods yield good results : if a cell is detected, its shape is correctly drawn. Some exceptions are present for strongly flattened cells or cells that are anyway not used by biologists because they are mis-placed on their support or overlapping each other.

Concerning bright spots detection, the unique thresholding and filtering method performs better than the iterative thresholding one. Indeed, the iterative thresholding method is less shape specific. Moreover, the minimum used threshold seems to be crucial and it should be adapted to image intensities. Globally, we have seen that for elliptic cells, intensities were higher. It could be intrinsically due to the type of cells or could depend on acquisition parameters. For the unique thresholding and filtering method, performances are higher. However, the used threshold was slightly adapted to optimize results. For further use, the same adaptation could be used for same images type or the way it is defined should be adapted mainly by modifying the way a correct spot is defined. Finally, this method is better suited for healthy cells where spots are better shaped. For elliptic cells, spots are larger and flattened. Many Mexican Hat filter sizes could be used to detect spots of larger areas. However, an adaptation to elliptic spots will be more difficult since their orientation is variable.

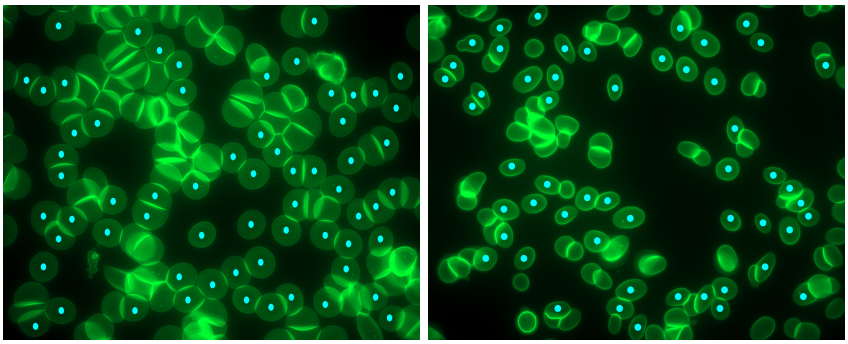
Finally, the developed methods were only used for cholesterol domains acquired with confocal microscopy. However, since segmentation is made on the transmission images, the segmentation methods are general whatever the fluorescent labelling and can be used for all segmentation tasks of RBC in confocal images. On the contrary, domains detection techniques are limited to cholesterol domains in confocal images, or at least to cases where light is only emitted from domains and not from the whole cell as it is the case for BODIPY-sphingomyelin labelling. Moreover, input parameters can be adapted to detect larger or smaller domains, as well as differently shaped ones. However, for the Unique thresholding and filtering method, domains must stay circular.

6.2 Wide-field images

6.2.1 Cells Segmentation

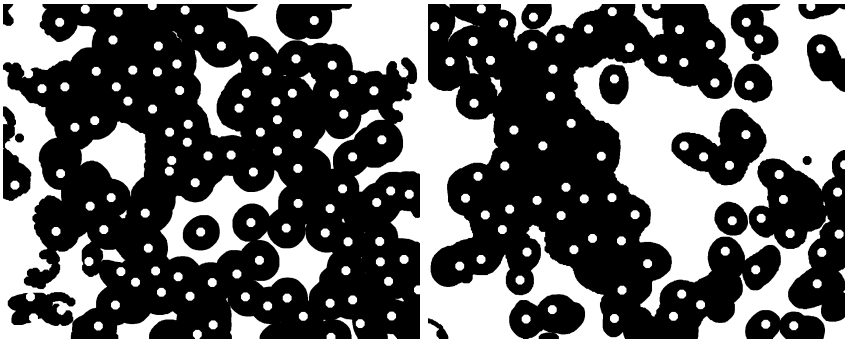
For wide-field images only one technique for cell segmentation is proposed. It consists in a controlled marker watershed, where the marker is based on thresholding and on Circular Hough Transform. Visual results are given in figure 6.12 for healthy and elliptic cells. Globally, touching cells are not well segmented since their shape and size are different from the regular red blood cells. It is thus preferable to have images where cells are not touching. This is also required by biologist to be able to correctly detect bright spots manually. As for confocal images, the weak point of this method is seeding. However, here seeding seems better accurate since we have less cells segmented in many regions. Same improvement as the one proposed for confocal images could be implemented.

Detection rates and shape coefficients are computed for each image to provide a better evaluation of the segmentation. The detection rate (fig. 6.13(a) and 6.14(a)) is better for elliptic cells. As previously said, this is mainly due to the fact that elliptic cells are smaller and thus not touching each other in the image. Cells are better detected when there are not touching other ones. Concerning segmentation quality, shape coefficients are equivalent for both image types and are satisfactory because if we assume that spots are well spread among cells, all spots in detected cells are in the segmented regions.



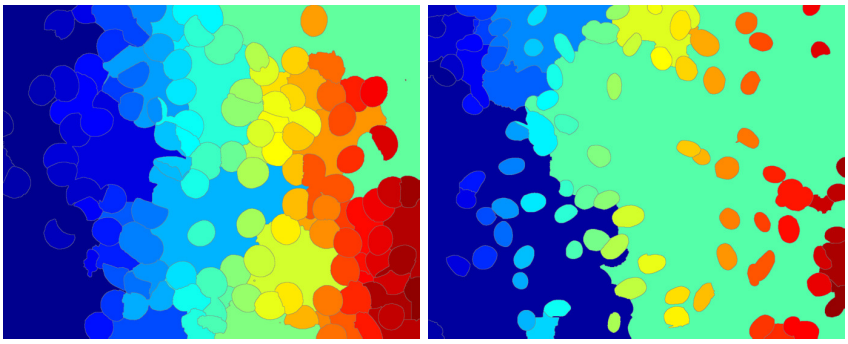
(a) Initial fluorescent image with annotated cells

(b) Initial fluorescent image with annotated cells



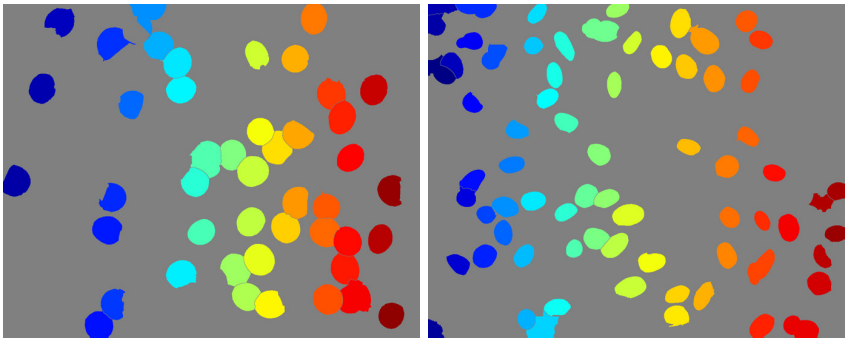
(c) Markers used for controlled watershed

(d) Markers used for controlled watershed



(e) Segmentation image

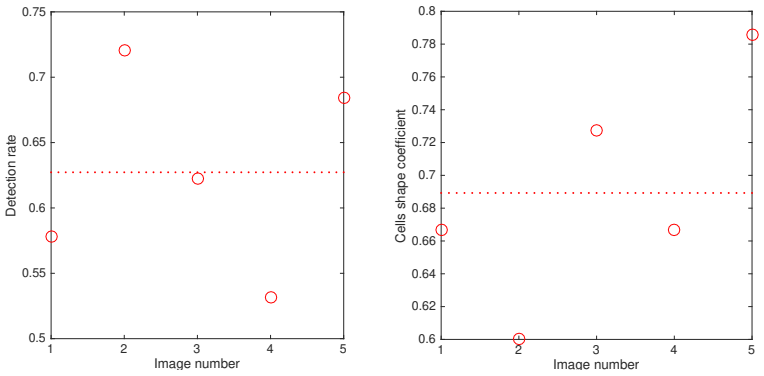
(f) Segmentation image



(g) Segmented cells

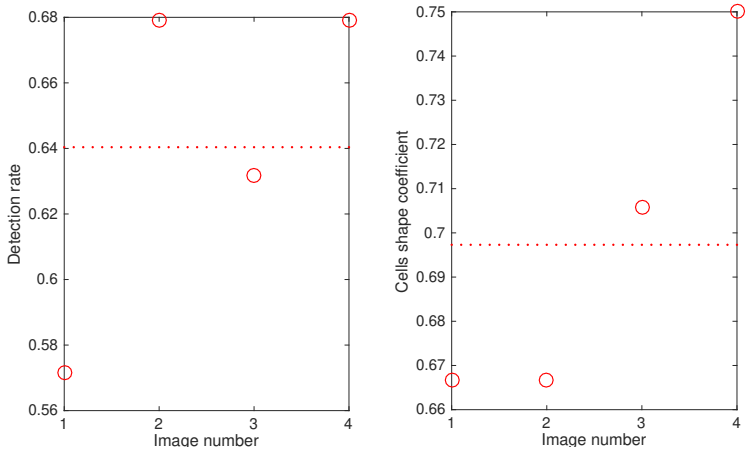
(h) Segmented cells

Figure 6.12: Segmentation results for wide-field images of healthy (left column) and elliptic cells (right column). The image to segment, the marker, the segmentation results as well as the regions kept from the segmentation and that correspond to cells are shown.



(a) Mean detection rate = 0.627±0.0059 (b) Mean shape coefficient = 0.6893±0.0049

Figure 6.13: Detection rate and shape coefficient for the different images for healthy cells.

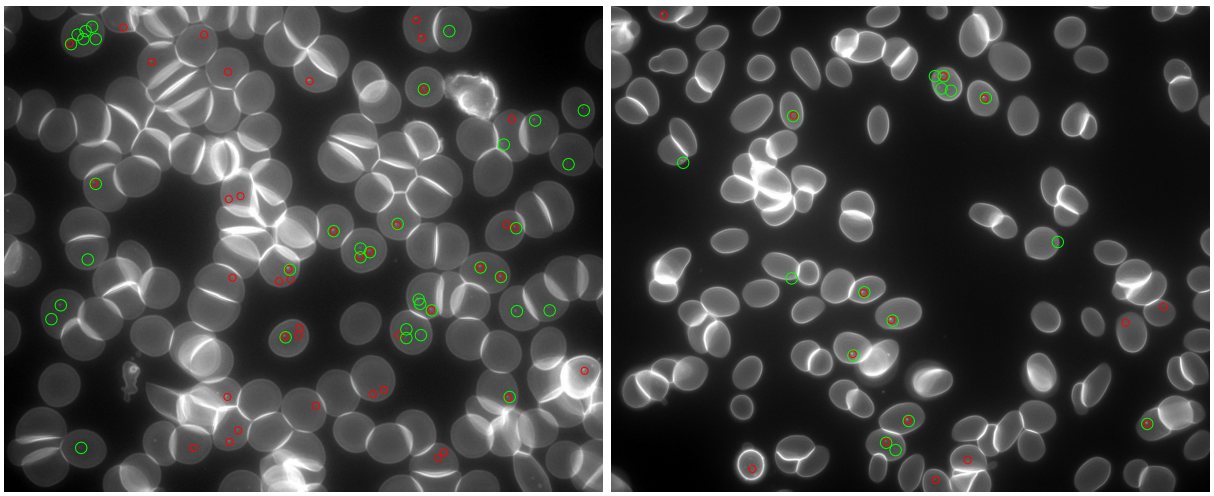


(a) Mean detection rate = 0.6404±0.0026 (b) Mean shape coefficient = 0.6973±0.0016

Figure 6.14: Detection rate and shape coefficient for the different images for elliptic cells.

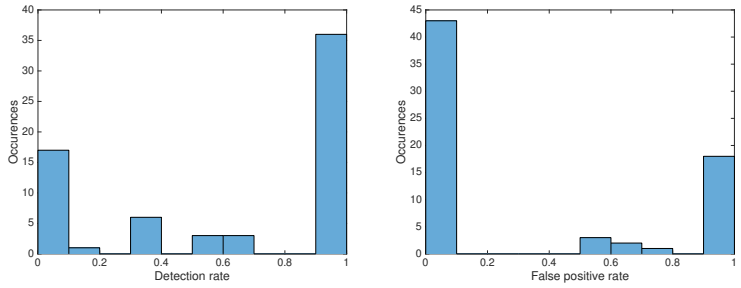
6.2.2 Bright spots Detection

Some detection results are shown on figure 6.15. For both images, there are missing detections and also false positives. False positives are due to Sobel filtering that add noise to the image, while missing detections are due to the fact that in the Sobel image, spots are not brighter enough compared to cell. From the histograms of detection rate and false positive rate, we can say that for elliptic cells there are less false positives than for healthy cells. However, since there is not much points detected, the statistic is poor and histograms are less representative of a global behaviour. In comparison to confocal images results, bright spots results are here worse. Indeed, due to the fact that the fluorescence of the whole cells is detected by the microscope, contrast between cells and spots is lower. This complicates spots detection. Moreover, since there are not a lot of spots per cell, results need to be really accurate for further computations. On the contrary, for confocal images, it was less critical due to the large amount of spots that will attenuate errors in terms of location and density. To improve results, Sobel filtering should be avoided as it increases noise. Thresholding is not well performing. This is due to the microscope used as well as to the kind of labelling. Using confocal images (this type of image was shown in figure 1.2) will maybe yield better results as for cholesterol domains.

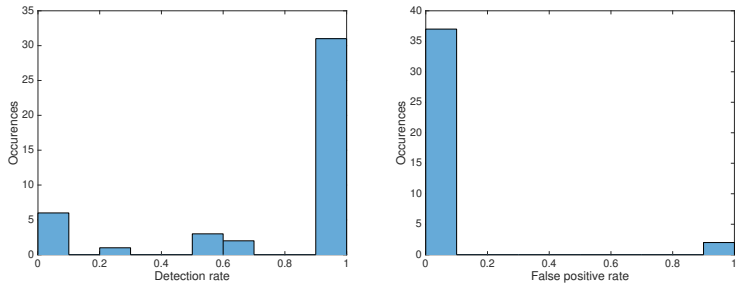


(a) Healthy cells (b) Elliptic cells

Figure 6.15: Bright spots detection results for healthy cells and elliptic cells. Red dots are algorithm results and green dots are ground truth.



(a) Detection rate histogram for healthy cells (b) False positive rate histogram for healthy cells



(c) Detection rate histogram for elliptic cells (d) False positive rate histogram for elliptic cells

Figure 6.16: Analysis of detection rate and false positive rate for healthy and elliptic cells

6.2.3 Partial conclusion on wide-field images

Concerning cells segmentation, unpacked cells are better segmented and this is mainly visible for elliptic cells that are smaller. As for confocal images, correct seeds location is crucial. Solutions to improve it are watershed regions merging, graph-cuts used to allow many seeds in one cell or intensities analysis at seeds location to remove or modify them. These are the same than the ones proposed for confocal images.

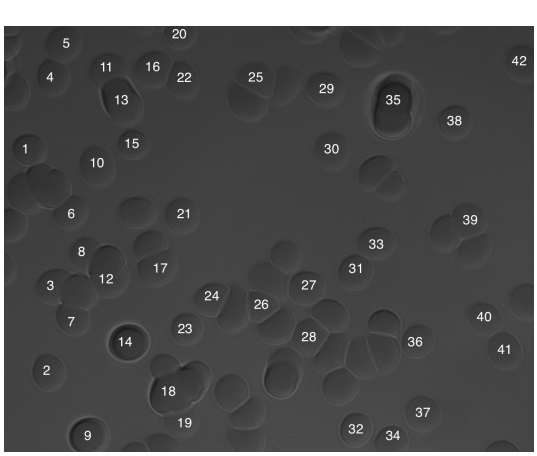
Concerning bright spots detection, the number of spots per cells is well evaluated by the algorithm. However, frequently detected bright spots do not match ground truth. Since the number of spots in one image is not huge, detection must be really accurate. We have seen that Sobel filtering and thresholding were not the best tools for this. A solution to improve detection is to use confocal images instead of wide-field images. Wide-field images were firstly used due to their rapid acquisition. However, confocal images because they gather light only from a thin sample layer will be less bright and spots could be easily detected.

Finally, it is worth mentioning that proposed methods were designed specifically for the detection of sphingomyelin domains in wide-field images. Since segmentation and spots detection methods are performed on the fluorescence image, methods cannot be used for other microscope images or other lipidic domains. However, the detection of domains of other sizes or shapes can easily be implemented.

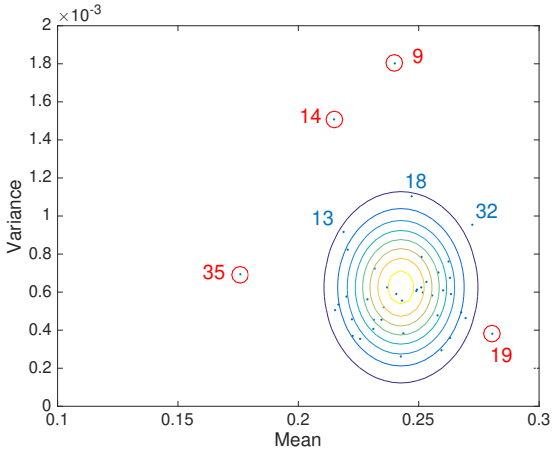
6.3 Irrelevant cells detection

As explained in section 4.5, some cells need to be removed from the segmentation we obtained previously. Primary results show that the RANSAC method was able to remove irrelevant cells but each time wrong segmented cells were also removed. This led us to define irrelevant cells as darker cells not well attached to the support, but also as wrong segmented cells that have not been removed by previously applied methods. Since the same method is applied on both images types, results are shown together.

First of all, RANSAC is a random method, results are thus variable. Depending on the randomly generated sample, cells that are rejected will be different. We can see in figure 6.17 that rejected cells correspond to darker cells as expected (cells n°9, 14 and 35) but also to lighter cells as cell n°19. Moreover, due to random variations, cells n°13, 18 and 32 also appear to be rejected in some cases. Cells n°13 and 18 are darker because many cells stick to each other and this results also in a wrong segmentation. Finally, cell 32 should not be removed at all but it is sometimes the case.



(a) Transmission image



(b) Mean-variance plot : rejected cells are surrounded in red, the Gaussian probability density function is shown with yellow to blue curves

Figure 6.17: Ransac results for a sphingomyelin marked image (wide-field acquired image)

More quantitatively, the detection rate and the false positive rate can be assessed for each image type. Results are shown in table 6.1. Detection rates are close to 100%, which is good. However, as mentioned, false positive rates are high too. This reflects the removal of cells we would like to keep for analysis. False positive rates are higher for confocal images than for wide-field images. Globally, those results are not critical since, as we will see later, the number of cells kept for the analysis does not influence much results due to the large number of cells used. However, to improve results, the fluorescence information could be used too. Learning technique could also be implement to learn a cell model based on annotated data and then be able to reject irrelevant cells.

		Detection rate	False positive rate
Wide-field image	Healthy cells	100%	35%
	Elliptic cells	92.3%	50%
Confocal image	Healthy cells	87.5%	68%
	Elliptic cells	100%	54%

Table 6.1: Detection rates and false positive rates for irrelevant cells detection.

Chapter 7

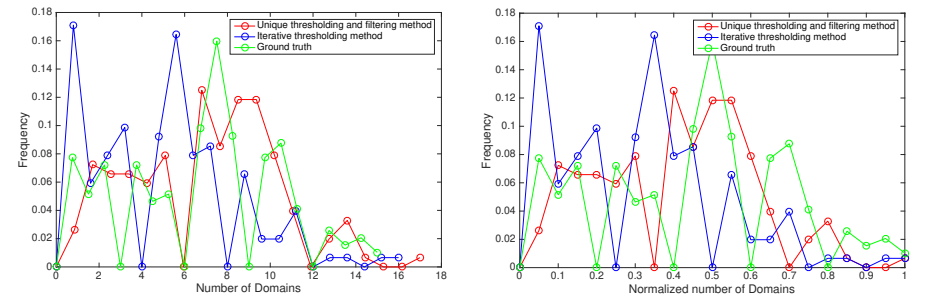
Lipidic Domains Analysis

Algorithm results have been compared to ground truth to assess their quality. But even with wrong detections or segmentation, some values of interest could be well estimated. A relative comparison between healthy cells and elliptic cells could also be meaningful. Some outputs analyzed by biologists will thus be computed : they are interested in the location and radial distribution of bright spots, their density, their size distribution and their coverage of cells. The precise definition of each characteristic and the way there are computed are explained in section 5.2. For each characteristic, values computed by the algorithm will be compared to ground truth. The meaningfulness of a comparison between healthy cells and elliptic ones will also be assessed.

7.1 Cholesterol domains

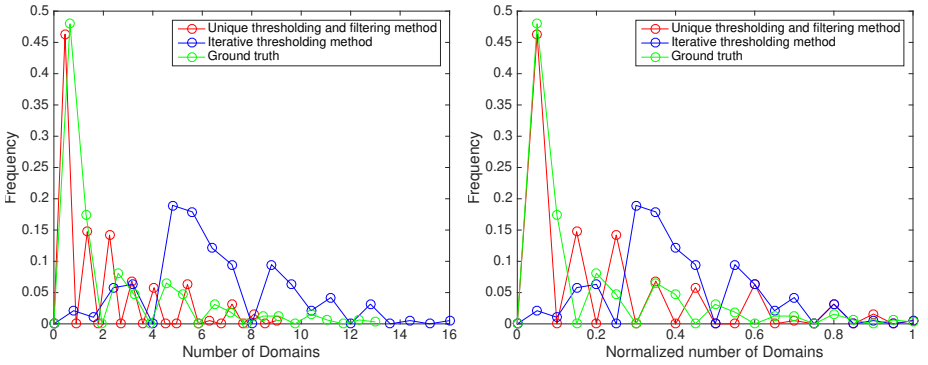
7.1.1 Number of bright spots

The number of bright spots per cell does not follow a gaussian distribution (as seen in figure 7.1). Moreover, the distribution returned by the algorithms is wrong compared to ground truth. Even when the numbers of spots are normalized by the maximum number of spots per cells (right column of figure 7.1), distributions do not match. Only for elliptic cells, the proportion of cells that have no bright spots is in agreement with ground truth. However, if we normalize the number of spots by the cells area i.e. compute the density, we can see that the unique thresholding and filtering method is able to reproduce ground truth results (fig. 7.2). The iterative thresholding method does not estimate the mean density correctly, it detects either too much or not enough spots. A comparison can then be made between healthy cells and elliptic cells. We can see that for ground truth, the density is 2 times larger for healthy cells than for elliptic cells (values are given in table 7.1). This is also confirmed by the Unique thresholding and filtering method. However the iterative thresholding method completely fails at evaluating this value. This is due to the fact that, as seen previously, this method shows a high number of false positives for elliptic cells and nearly not for healthy cells.



(a) Number of bright spots distribution per cell for healthy cells

(b) Normalized number of bright spots distribution per cell for healthy cells



(c) Number of bright spots distribution per cell for elliptic cells

(d) Normalized number of bright spots distribution per cell for elliptic cells

Figure 7.1: Analysis of the number of bright spots per cell.

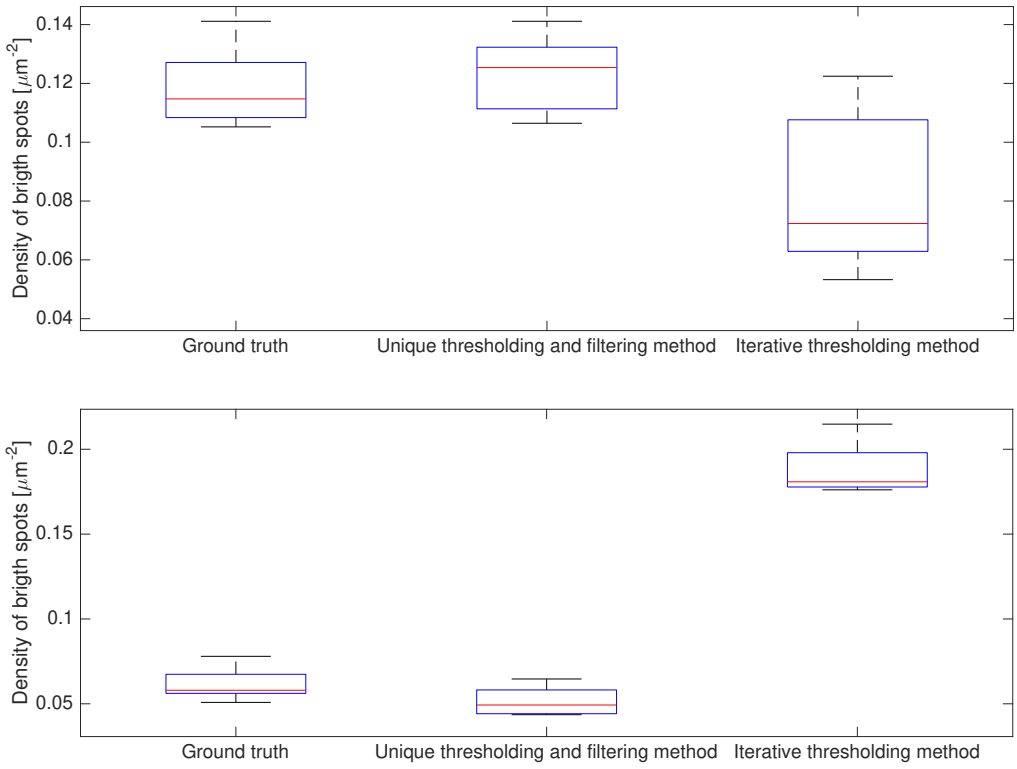


Figure 7.2: Density of bright spots : upper panel : healthy cells; lower panel : elliptic cells.

Ground truth	Unique thresholding and filtering method	Iterative thresholding method
0.52	0.47	2.49

Table 7.1: Ratio between density of bright spots in elliptic cells and healthy cells.

7.1.2 Bright spots location

Since biologists are interested in the radial distribution of bright spots, we analyzed the detection performances regarding the distance to the center of the cell. Results are shown in figures 7.3 and 7.4 for both techniques. First, concerning healthy cells, the unique thresholding and filtering method is performing pretty well : the curve is in good agreement with the ground truth curve. On the contrary, the iterative thresholding method, due to a lower detection rate, is under the ground truth curve. However, once curves are normalized with respect to the total number of bright spots detected, distributions are similar (right panel of fig. 7.3). This proves that even if detections are missing and false positive detections are present, distributions computed by both techniques can be trusted for healthy cells. This property can be explained by the fact that a lot of points (nearly 1000) are detected in all 5 images and used to draw the curve. Globally, false detections and missing ones are compensating each other, leading to a correct distribution.

Concerning elliptic cells (fig. 7.4), the Unique thresholding and filtering method is also in good agreement with ground truth. Even if it misses some detections, the bright spots distribution corresponds also the ground truth. On the contrary, the iterative thresholding method detects much more points and these points are mainly located more than 20 pixels[1] from the cell center. The bright spot distribution is thus not the same and the mean distance to cell center will be overestimated if based on this method. By looking at normalized curves, distributions are in good agreement, the Iterative thresholding method seems however sharper.

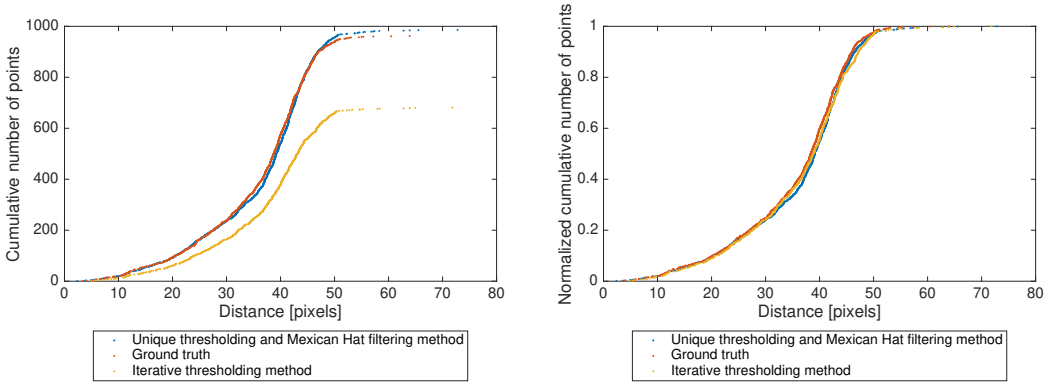


Figure 7.3: Comparison of bright spots distributions between ground truth and both detection methods for healthy cells. The left panel is the cumulative number of spots and the right panel is the normalized curve.

[1] 20 pixels correspond approximately to 2 μm for confocal images in our dataset.

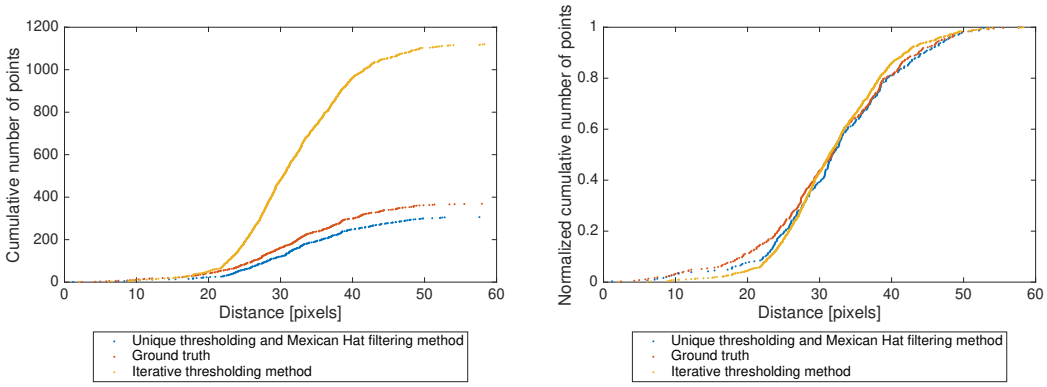


Figure 7.4: Comparison of bright spots distribution between ground truth and both detection methods for elliptic cells. The left panel is the cumulative number of spots and the right panel is the normalized curve.

Another way to look at the bright spots distribution is to compute the percentage of bright spots located at the cell periphery and in the central part of the cell. As can be seen in figure 7.5, for healthy cells, the mean percentage of spots located in the central part of the cell is correctly estimated by both methods compared to ground truth. This result is comparable to what was already computed by C. Léonard et al. in 2017 [23]: they also reached a percentage of about 40% for central bright spots. This also proves that cells segmentation is adequate. However, for elliptic cells, the ratio is underestimated by both methods. It shows that not enough cells are detected in the central part of cells. This was also seen in figure 7.4 where results curves are under ground truth curve for distances less than 30 pixels.

A comparison between healthy cells and elliptic ones can now be performed (values are given in table 7.2). Ground truth defines a ratio of percentage of bright spots in central part of cells between elliptic cells and healthy ones of 0.619. The unique thresholding and filtering method approximate this value quite well. Even if both percentages are lower than ground truth, the ratio between them is the same. On the contrary, the iterative thresholding method underestimates this value greatly due to a percentage for elliptic cells too low compared to healthy cells.

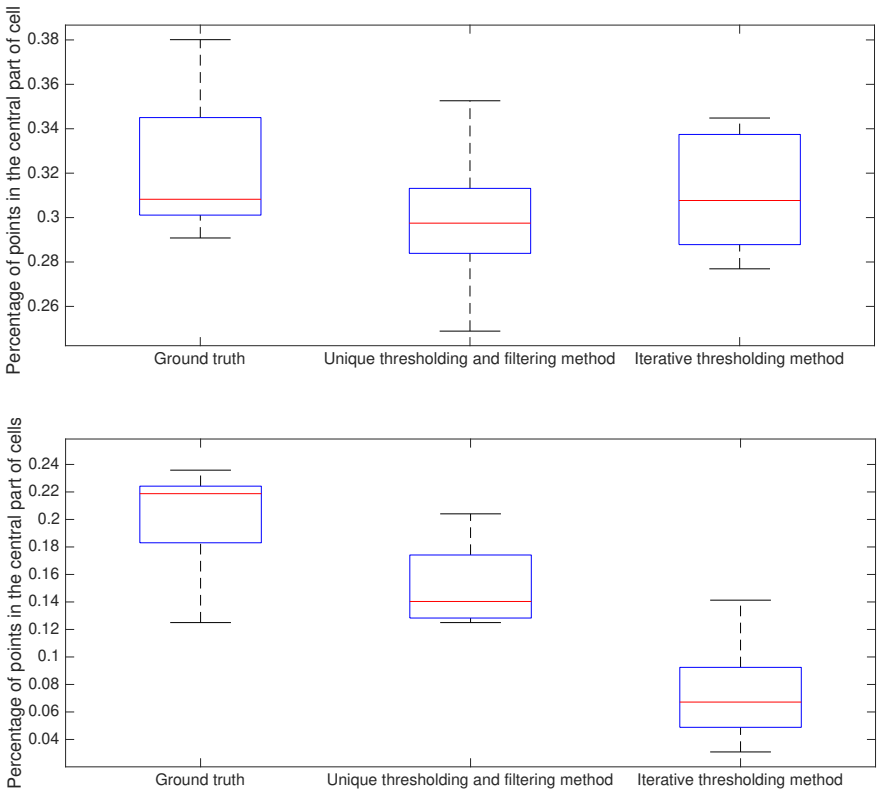


Figure 7.5: Percentage of bright spots in the central part of cells for ground truth and algorithmic results : upper panel : healthy cells; lower panel : elliptic cells.

Ground truth	Unique thresholding and filtering method	Iterative thresholding method
0.619	0.55	0.25

Table 7.2: Ratio between percentage of bright spots in the central part of elliptic cells and healthy cells.

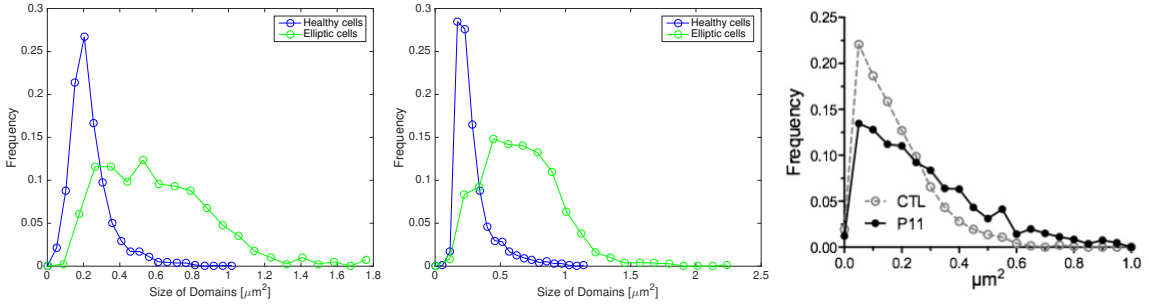
7.1.3 Domains area and surface coverage

Manual results for domains area are not available for our dataset. A comparison between our results and results obtained on another dataset is performed (fig. 7.6). We can see that for both methods, results are in agreement with results from Léonard et al. However for elliptic cells, we detected spots with larger sizes. For both methods, results are really similar due to the fact that the way the size is computed is the same, only domains used for analysis are different and since there are a lot of points, distributions are comparable. Next, a comparison between healthy cells and elliptic cells can be made. Elliptic cells have larger points and the size distribution is larger, compared to healthy cells.

The major issue here is that the way biologists determine domains area is not well defined. The definition lack of precision and results are hardly reproducible.

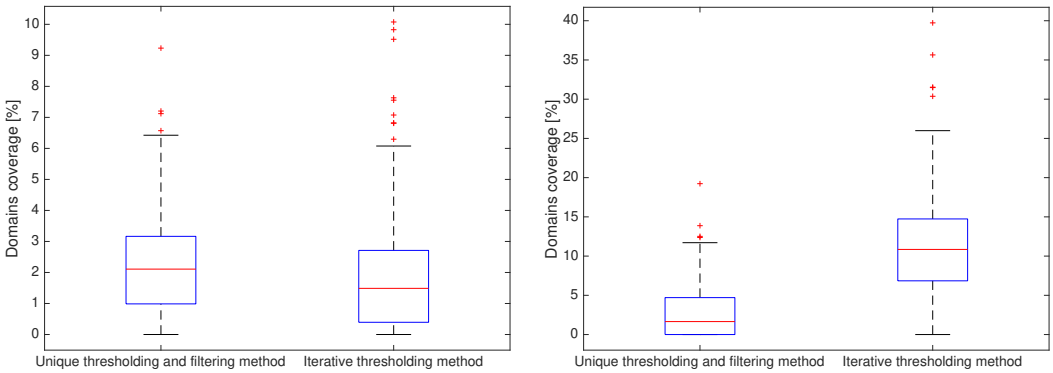
Finally, based on domains size, the surface coverage of cells, more precisely of hemi-red blood cells since only one side of the cell is seen by microscopy, can be computed. Since no ground truth is available, results quality cannot be assessed. However, because the shape of segmented cells was correctly defined and because the size of spots is in agreement with other results, surface

coverage should be correctly estimated. Concerning healthy cells, both methods compute a coverage of about 1.5%. However, coverages computed for elliptic cells are different depending on the spots detection method. The iterative thresholding method evaluates quite well spots area but due to a really high false positive rate, the coverage is importantly over-estimated.



(a) Unique thresholding and filtering method (b) Iterative thresholding method (c) Similar results from Léonard et al.[23] (unpublished data)

Figure 7.6: Frequency histogram of domains size



(a) Healthy cells (b) Elliptic cells

Figure 7.7: Coverage percentage for healthy and elliptic cells

7.1.4 Partial conclusion on cholesterol domains

We have seen that despite low detection rates for both methods, some domains characteristics were correctly computed and matched ground truth. Concerning the number of domains per cell, only the percentage of cells without domains was correctly estimated by both methods. The total number of domains was well evaluated only by the unique thresholding and filtering method. The related domains density was also correctly computed by this method. Concerning domains location, both methods were able to reproduce normalized cumulative distributions and thus percentage of domains in the central part of cells, for healthy ones. For elliptic cells, densities were underestimated by both methods due to slightly too much detection in the outer part of cells and not enough detection in the central part. Concerning domains area, discussion is more tricky since ground truth is not available. However compared to other works, our area definition seems appropriate. Mainly for healthy cells, area and thus surface coverage are in agreement between both methods. However, for elliptic cells, the iterative thresholding method due to a too high false positive rate, clearly over-estimates domains coverage.

7.2 Sphingomyelin domains

7.2.1 Number of bright spots

Since the detection rate is high and the false positive rate low, the number of bright spots per cell is correctly evaluated by the proposed method. From figure 7.8, we can see that frequencies are well reproduced by the algorithm. However, for both cells types, the method has a lower frequency for high numbers of spots. Indeed, we miss some spots and have no cells with more than 4 domains for healthy cells and 2 domaines for elliptic ones.

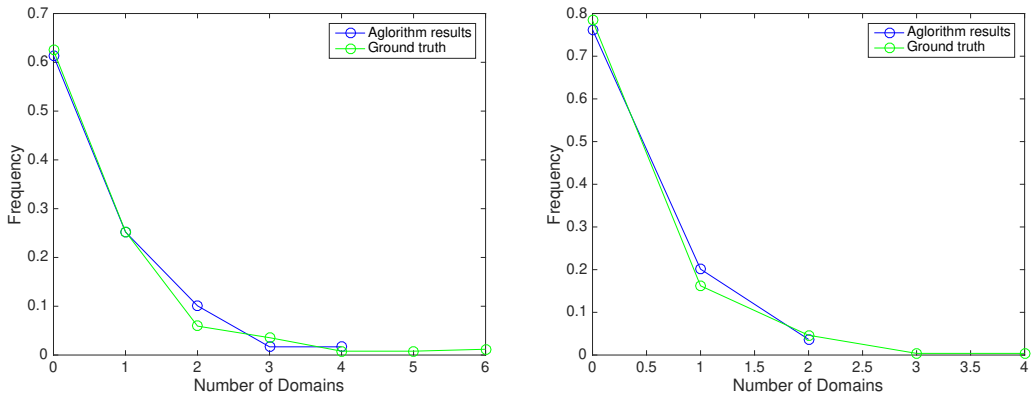


Figure 7.8: Frequency of the number of brights spots per cell for healthy cells (left panel) and elliptic cells (right panel).

We can then look at the density of bright spots. When comparing values between ground truth and method results, they are relatively in the same range. However, values are in both cases smaller due to the fact that we detected less domains. Moreover, ground truth results are more spread than algorithmic results. A comparison between healthy cells and elliptic cells can then be made. The ratio of density is slightly different depending if it is based on ground truth or algorithmic results (see results in table 7.3). However, values stay comparable.

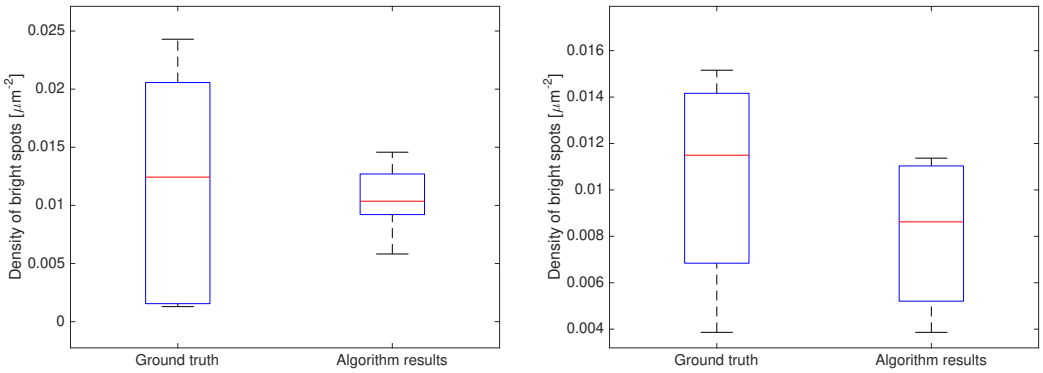


Figure 7.9: Density of domains : left panel : healthy cells; right panel : elliptic cells

Ground truth	Algorithm results
0.889	0.764

Table 7.3: Ratio between densities of bright spots in elliptic cells and healthy cells.

7.2.2 Bright spots location

Concerning the bright spots distribution, both for healthy and elliptic cells, results do not match ground truth (fig. 7.10 and 7.11). For healthy cells, distributions are similar until 20 pixels[2] away from the center (approximatively half the cell radius), after there are too much missing detections and the number of points is lower. Concerning elliptic cells, few points are detected too far from the cell center compared to ground truth. This leads to a normalized distribution shifted to the left.

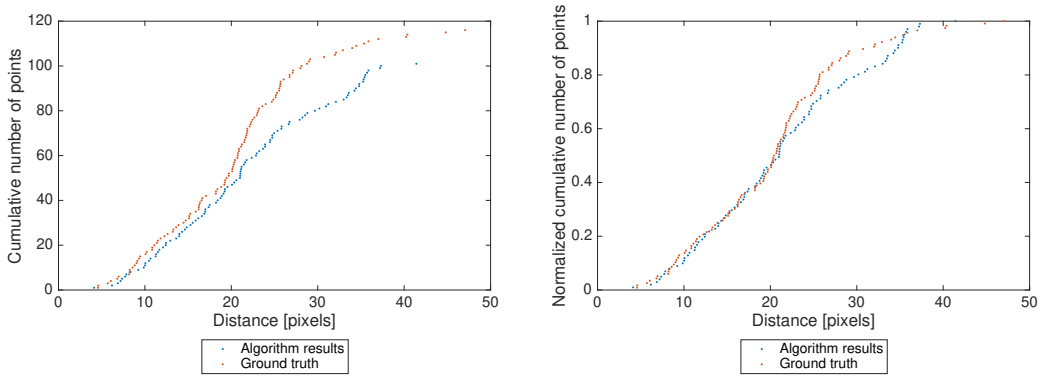


Figure 7.10: Comparison of bright spots distributions between ground truth and method detection for healthy cells. The left panel is the cumulative number of spots and the right panel is the normalized curve.

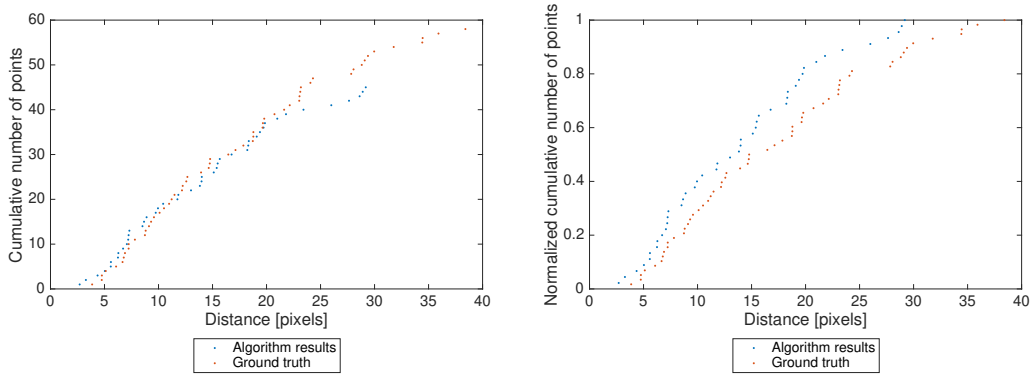


Figure 7.11: Comparison of bright spots distributions between ground truth and method detection for elliptic cells. The left panel is the cumulative number of spots and the right panel is the normalized curve

As previously, we also analyzed the percentage of spots that are located in the central part of cells. Results are shown in figure 7.12. Ground truth and algorithm results show the same tendency : most of spots are located in the central part of cells. However, we have seen previously that bright spots detection was not performing very well : it misses mainly spots located at the cells periphery and thus overestimate the proportion of spots located in the central part of cells. However, these results are in good agreement with value collected by C. Léonard et al. They computed that 100% of bright spots were located in the central part of cells [23]. However, when comparing elliptic cells to healthy ones, the ratio between them is different for ground truth and algorithm results (values are given in table 7.4). Ground truth predicts a ratio of 0.896 while our

[2]20 pixels correspond to approximately $1.8\mu m$ for wide-field images of our dataset.

algorithm computes a ratio of 1.014. In one case, the percentage is higher for healthy cells and in the other, it is higher for elliptic cells.

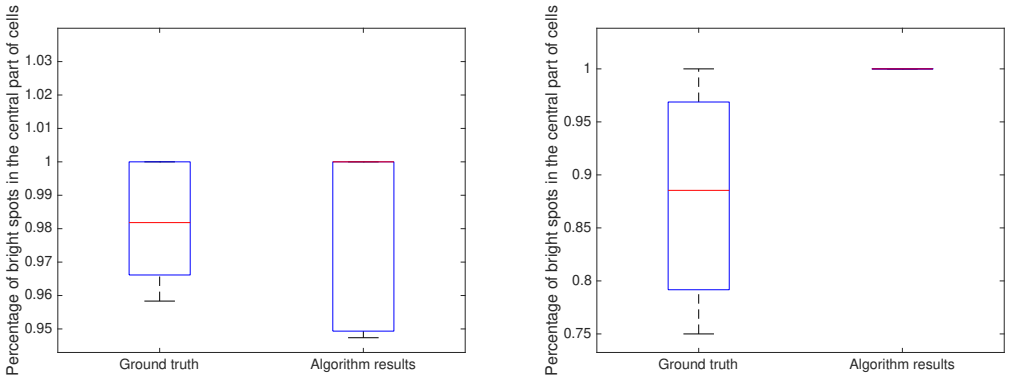


Figure 7.12: Percentage of bright spots located in the central part of cells for healthy cells and elliptic ones. Comparison between ground truth and algorithm results are provided. Left panel : healthy cells; right panel : elliptic cells.

Ground truth	Algorithmic results
0.896	1.014

Table 7.4: Ratio between percentage of bright spots in the central part of elliptic cells and healthy cells.

7.2.3 Domains area and surface coverage

For domains area and coverage, no ground truth is available to compare results. Only algorithmic results are given in the following section. We already know that we have a large number of false positive detection. This is why these domains have been discarded for analysis. Therefore, presented results do not reflect global algorithm performances but only size evaluation on correctly detected domains. Since no ground truth is available to assess computation quality, visual checking was used to evaluate performances. Such results are show in figure 7.13 for two domains. We can see that areas are correctly estimated.

Domains area histogram is show in figure 7.14-left panel for healthy and elliptic cells. Healthy cells have larger spots and their area range is larger than for elliptic cells. Domains coverage (fig 7.14-right panel) then follows the same trend. Here only cells with detected domains are kept to compute the coverage. Indeed, a lot of cells have no domains and their coverage is thus zero, computing the mean coverage will give a value close to zero. Concerning the histogram, zero coverage values have also been removed to see more clearly the distribution for cells that have domains in them. Most of cells have a coverage of 0.4% for both cells type. Moreover, a larger amount of healthy cells have a larger coverage compared to elliptic cells.

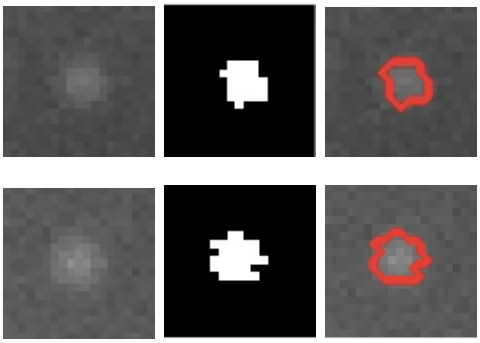


Figure 7.13: Sphingomyelin domains size evaluation results for 2 domains. Left images : fluorescent images, central images : thresholded images, right images : domain contour applied on fluorescent images.

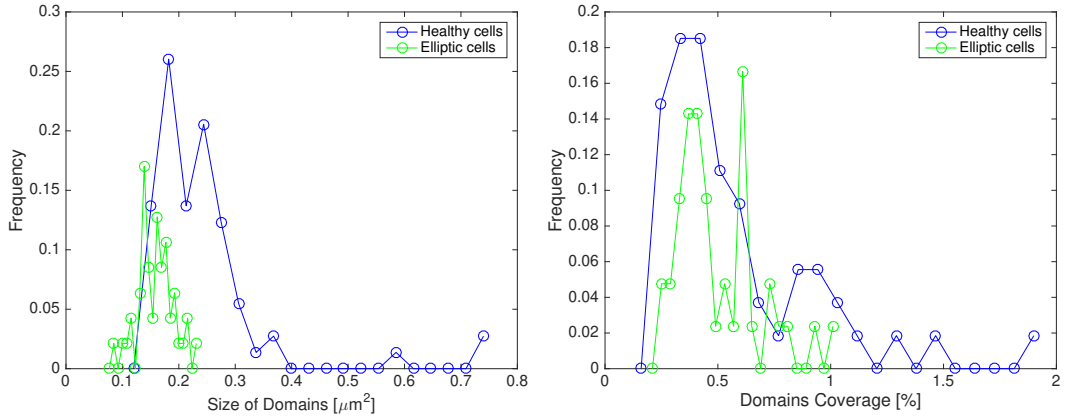


Figure 7.14: Left panel : frequency histogram of domains size; right panel : frequency histogram of domains coverage

7.2.4 Partial conclusion on sphingomyelin domains

The proposed method is able to correctly compute the number of domains per cell, except for high number of domains. The density of domains is thus slightly underestimated. Concerning domains location, undetected ones are mainly located at the outer part of cells. This leads to an overestimation of the percentage of domains in the central part of cells. Finally, concerning domains sizes, no ground truth is available to confirm results but visual assessment validate the size computation. Moreover, only correct detection have been kept for computation leading to a good size estimation.

Chapter 8

Conclusion

We proposed methods to detect bright spots (lipidic domains) and segment red blood cells in fluorescent images. We mainly focused on wide-field images of sphingomyelin domains labelled with BODIPY-sphingomyelin probes and on confocal images of cholesterol domains labelled with Theta probes.

Confocal images - cholesterol domains

Concerning confocal images, we proposed two methods to detect cholesterol domains. Both are applied on fluorescence images. The first is an iterative thresholding method and the second, a unique thresholding and filtering method. The iterative thresholding method will iteratively threshold the image, store regions that correspond to the domain definition and remove them from the images. The unique thresholding and filtering method will first filter the image with a Mexican Hat filter and then threshold this image with a computed threshold defined as the one for which the percentage of regions corresponding to domains is the highest. These methods require as input parameters an area range of domains to keep and a maximum allowed eccentricity.

We have shown that both methods missed detection and had false positives. For the unique thresholding method, the threshold was adapted by a multiplicative coefficient, leading to better results. It was defined thanks to the ROC curve analysis. However, this adaptation shows that the criterion to define correct domains should be adapted. We have seen that the used area range was correct, mainly the maximum eccentricity should be adapted. Another way to solve the problem is to use the same adaptation that was made based on ROC curves. Indeed, all confocal images of cholesterol domains have the same properties and keeping the same multiplicative coefficient is relevant. Performances of this method for healthy cells were higher since domains in healthy cells seemed better shaped. To increase detection in elliptic cells, many filter sizes could be used and an adaptation could be made for flattened shapes.

Regarding the iterative thresholding method, performances are lower compared to the other method. We have seen that the lower threshold used was crucial. It was currently a constant value. However, it could be adapted depending on image intensities. This will help to increase detection rate or lower false positive rate. The threshold was observed to be higher in elliptic cells, for intrinsic reasons or for acquisition reasons. Whatever the reason, if it is adapted for each image, performances will get better.

Concerning cells segmentation, two methods were also proposed for confocal images. Based on the transmission image, a marker controlled watershed algorithm is performed. For the Circular Hough Transform controlled watershed method, the marker is defined by centers of circles detected by the CHT. For the Thresholding controlled watershed method, the marker is obtained from binarization of the transmission image with a threshold computed from histogram analysis.

Performances have been assessed and results show that methods reach between 60 and 80% of detection rate. The CHT controlled method is better suited for healthy cells segmentation, while for elliptic cells the thresholding controlled watershed yields better results. This is mainly due to the fact that the CHT controlled watershed is very specific to circular shapes. The main cause of missing detections is incorrect seeding. Many seeds can be found in one cell, resulting in over-segmentation. In other cases, no seeds are present, the cell is thus not segmented or finally, the seed is badly placed and englobes two cells that are thus merged together. Potential solutions for this could be to use graph-cuts that allow many seeds in one region to segment, or to produce too much seeds and then merge regions together. For seeds that are placed on cells edges, the intensities at this location could be analyzed to determine if seeds should be kept or not or to cut them to have one seed in each cell.

Methods have been used to compute domains characteristics. We have seen that domains densities are correctly evaluated by the Unique thresholding and filtering method. Both methods were able to reproduce cumulative number of domains with respect to center distance, for healthy cells. For elliptic cells, curves are less suited : there are not enough detections in the central part of cells and too much in the periphery. Percentage of domains in the central part of cells is slightly underestimated by the unique thresholding and filtering method. However, the ratio of this percentage between healthy cells and elliptic cells are in agreement with ground truth. On the contrary, the iterative thresholding method completely fails. Finally, domains areas and area coverage were correctly computed for healthy cells. For elliptic cells, since a too high false positive rate is observed, the area coverage computed by the iterative thresholding method is strongly overestimated. On the contrary, the value from the unique thresholding and filtering method is trusted.

Wide-field images - sphingomyelin domains

One method is proposed to detect sphingomyelin domains. The first step was to filter the fluorescent image with a Sobel filter and the second step was to use iterative thresholding to detect domains. Results with this method are quite poor. A lot of false positive detections and a low detection rate are observed. This was mainly due to noise introduced by the Sobel filter. Moreover, domains are hardly detectable only with a thresholding since cells are already highly bright due to the type of fluorescent labelling and microscope type. A solution to improve results could be to use confocal images.

In terms of cells segmentation, a unique method was proposed. It combines thresholding and CHT results to build a control marker for watershed segmentation. Results are similar to confocal images. Since methods are based on the same principles, same improvements are proposed.

Due to poor domains detection results, their analysis is quite limited. Despite this, the number of domains per cell is correctly estimated and the domain density is slightly underestimated. Concerning domains location, the percentage of domains in the central part of cell is overestimated since mainly domains at periphery were not detected. Due to bad performances, only correct detections were used to compute domains sizes. Ground truth data was not available to assess quality. However, visual analysis shows that size computation was correctly done.

Globally, we can say that sphingomyelin domains are less present in cells. Due to this, detection must be really accurate to produce good results. On the contrary, cholesterol domains are more numerous. Thanks to this, small errors have a lower impact on global results. Regarding these results, it could be useful to analyze how much images are needed to reach statistical significance.

Perspectives

Methods were not perfectly working and some adaptations suggested previously could be implemented and tested to try to improve them. However, for cholesterol domains, the main characteristics were correctly computed by the Unique thresholding and filtering method. Moreover, proposed methods require a limited amount of parameters and all of them are related to biologist knowledge on shape of cells and domains. We have seen that the definition of what a domain is, lacks of precision for cholesterol domains. Afterwards, some aspects were not covered in this work. Methods were not tested on other image types and domains. However, in some cases it could be relevant : e.g. to segment every RBC image acquired with a confocal microscope, whatever the fluorescent probe; or to detect larger domains with similar shapes. What could also be done is to compare properties of sphingomyelin domains and cholesterol ones. Since detection method for sphingomyelin domains was not optimal, this comparison was not performed yet.

Bibliography

[1] T.J. Atherton and D.J. Kerbyson. The coherent circle hough transform. *British Machine Vision Conference*, 1993. doi:10.5244/C.7.27.

[2] T.J. Atherton and D.J. Kerbyson. Size invariant circle detection. *Image and Vision Computing*, 17:795–803, 1999.

[3] H. Bay, T. Tuytelaars, and L. Van Gool. Surf: Speeded up robust features. *Computer Vision and Image Understanding*, 110(3):346–359, 2008.

[4] E. Bengtsson, C. Wählby, and J. Lindblad. Robust cell image segmentation methods. *Pattern Recognition and Image Analysis*, 14(2):157–167, 2004.

[5] I. Berget, B.-H. Mevik, and T. Næs. New modifications and applications of fuzzy c-means methodology. *Computational Statistics and Data Analysis*, 52:2403 – 2418, 2008.

[6] A. Browet, C. De Vleeschouwer, L. Jacques, N. Mathiah, B. Saykali, and I. Migeotte. Cell segmentation with random ferns and graph-cuts. *Image Processing (ICIP), IEEE International Conference on*, 2016. 10.1109/ICIP.2016.7533140.

[7] C. Chen, W. Wang, J.A. Ozolek, and G.K. Rohde. A flexible and robust approach for segmenting cell nuclei from 2d microscopy images using supervised learning and template matching. *Cytometry A.*, 83(5):495–507, 2013.

[8] S. Chourasiya et al. Automatic red blood cell counting using watershed segmentation. *International Journal of Computer Science and Information Technologies*, 5(4):4834–4838, 2014.

[9] L. Da Costa, J. Galimand, O. Fenneteau, and N. Mohandas. Hereditary spherocytosis, elliptocytosis, and other red cell membrane disorders. *Blood Reviews*, 27:167–178, 2013.

[10] E.R. Davies. *Machine Vision : Theory, Algorithms, Practicalities.* Morgan Kaufmann, San Fransisco, third edition, 2005.

[11] Institut De Duve. Role de l'organisation des lipides membranaires dans la deformation des cellules et les maladies de fragilite membranaire. `https://www.deduveinstitute.be/fr/imaging-and-membrane-biology`. Consulted on Nov 8th 2017.

[12] R. Fisher, S. Perkins, A. Walker, and E. Wolfart. Morphology - closing. `https://homepages.inf.ed.ac.uk/rbf/HIPR2/close.htm`. Consulted on Feb 27th 2018.

[13] R. Fisher, S. Perkins, A. Walker, and E. Wolfart. Morphology - opening. `https://homepages.inf.ed.ac.uk/rbf/HIPR2/open.htm`. Consulted on Feb 27th 2018.

[14] P.G. Gallagher. Hereditary elliptocytosis: Spectrin and protein 4.1r. *Seminars in Hematology*, 41(2):142–164, 2004.

[15] C. Gonzalez, P. Melin, J. Castro, and O. Castillo. *Edge Detection Methods Based on Generalized Type-2 Fuzzy Logic*. Springer International Publishing, Switzerland, 2017.

[16] C. Harris and M. Stephens. A combined corner and edge detector. *Alvey Vision Conference*, 1988. doi:10.5244/C.2.23.

[17] Z. Jan, A. Khan, M. Sajjad, K. Muhammad, S. Rho, and I. Mehmood. A review on automated diagnosis of malaria parasite in microscopic blood smears images. *Multimed Tools Appl*, 2017. https://doi.org/10.1007/s11042-017-4495-2.

[18] L. Kitchen and A. Rosenfeld. Gray-level corner detection. *Pattern Recognition Letters*, 1:95–102, 1982.

[19] G. Lin et al. A hybrid 3d watershed algorithm incorporating gradient cues and object models for automatic segmentation of nuclei in confocal image stacks. *Cytometry Part A*, 56A(1):23–36, 2003.

[20] G. Lin et al. Hierarchical, model-based merging of multiple fragments for improved three-dimensional segmentation of nuclei. *Cytometry A.*, 63(1):20–33, 2005.

[21] C. Liu, F. Shang, J. A. Ozolek, and G. K. Rohde. Detecting and segmenting cell nuclei in two-dimensional microscopy images. *J Pathol Inform*, 7:42, 2016.

[22] D.G. Lowe. Distinctive image features from scale-invariant keypoints. *Internal Journal of Computer Vision*, 60(2):91–110, 2004.

[23] C. Léonard et al. Contribution of plasma membrane lipid domains to red blood cell (re)shaping. *Scientific Reports*, 7(1):4264 [1–17], 2017.

[24] B. Macq and G. Janssens. Lgbio2050 : Edge detection. Ecole Polytechnique de Louvain, UCL, Louvain-la-Neuve, 2016.

[25] MathWorks. Imfindcircle. `https://nl.mathworks.com/help/images/ref/imfindcircles.html?s_tid=srchtitle`. Consulted on Feb 13th 2018.

[26] Mathworks. Matlab : Understanding morphological reconstruction. `https://nl.mathworks.com/help/images/understanding-morphological-reconstruction.html#f18-26958`. Consulted on Apr 22th 2018.

[27] F. Meyer. Topographic distance and watershed lines. *Signal Processing*, 38:113–125, 1994.

[28] M. Mohideen and F.A. Niraimathi. A marker controlled watershed algorithm with priori shape information for segmentation of clustered nuclei. *International Journal of Advanced Research in Computer Science*, 2(1):349–355, 2011.

[29] P. Mukhopadhyay and B.B. Chaudhuri. A survey of hough transform. *Pattern Recognition*, 48:993–1010, 2015.

[30] J. Roerdink and A. Meijster. The watershed transform: Definitions, algorithms and parallelization strategies. *Fundamenta Informaticae*, 41:187–228, 2001.

[31] O. Schmitt and M. Hasse. Morphological multiscale decomposition of connected regions with emphasis on cell clusters. *Computer Vision and Image Understanding*, 113:188–201, 2009.

[32] C. Sha, J. Hou, and H. Cui. A robust 2d otsu's thresholding method in image segmentation. *Journal of Visual Communication and Image Representation*, 41:339–351, 2016.

[33] S. H. Shirazi, A. I. Umar, N. Haq, S. Naz, M. I. Razzak, and A. Zaib. Extreme learning machine based microscopic red blood cells classification. *Cluster Comput*, 2017. https://doi.org/10.1007/s10586-017-0978-1.

[34] S.J. Singer and G.L. Nicolson. The fluid mosaic model of the structure of cell membranes. *Science*, 175(4023):720–731, 1972.

[35] S. Trompeter and M.-J. King. Hereditary spherocytosis. *PAEDIATRICS AND CHILD HEALTH*, 25(8):381–386, 2015.

[36] T. Tuytelaars and K. Mikolajczyk. Local invariant feature detectors: A survey. *Foundations and Trends in Computer Graphics and Vision*, 3(3):177–280, 2007.

[37] D. A. Van Valen et al. Deep learning automates the quantitative analysis of individual cells in live-cell imaging experiments. *PLoS Comput Biol*, 12(11):e1005177, 2016.

[38] Z. Wu and R. Leahy. An optimal graph theoretic approach to data clustering: Theory and its application to image segmentation. *IEEE Transactions on Pattern Analysis and Machine Intelligence*, 15(11):1101–1113, 1993.

[39] C. Wählby, I.-M. Sintor, F. Erlandsson, G. Borgefors, and E. Bengtsson. Combining intensity, edge and shape information for 2d and 3d segmentation of cell nuclei in tissue sections. *Journal of Microscopy*, 215(1):67–76, 2004.

[40] W. Xie, J. A. Noble, and A. Zisserman. Microscopy cell counting with fully convolutional regression networks. *MICCAI 1st Workshop on Deep Learning in Medical Image Analysis*, 2015.

[41] F. Xing and L. Yang. Robust nucleus/cell detection and segmentation in digital pathology and microscopy images: A comprehensive review. *IEEE Rev Biomed Eng.*, 9:234–263, 2016.

[42] H.K. Yuen, J. Princen, and J. Illingworth, J.and Kittler. A comparative study of hough transform - methods for circle finding. *Image and Vision Computing*, 8(1):71–77, 1990.

[43] C. Zhang, F. Huber, M. Knop, and F.A. Hamprecht. Yeast cell detection and segmentation in bright field microscopy. *IEEE 11th International Symposium on Biomedical Imaging (ISBI)*, 2014. `https://www.researchgate.net/profile/Chong_Zhang29/publication/271424689_Yeast_cell_detection_and_segmentation_in_bright_field_microscopy/links/55f9a7ea08aeba1d9f1f7e2e.pdf?inViewer=0&pdfJsDownload=0&origin=publication_detail`.

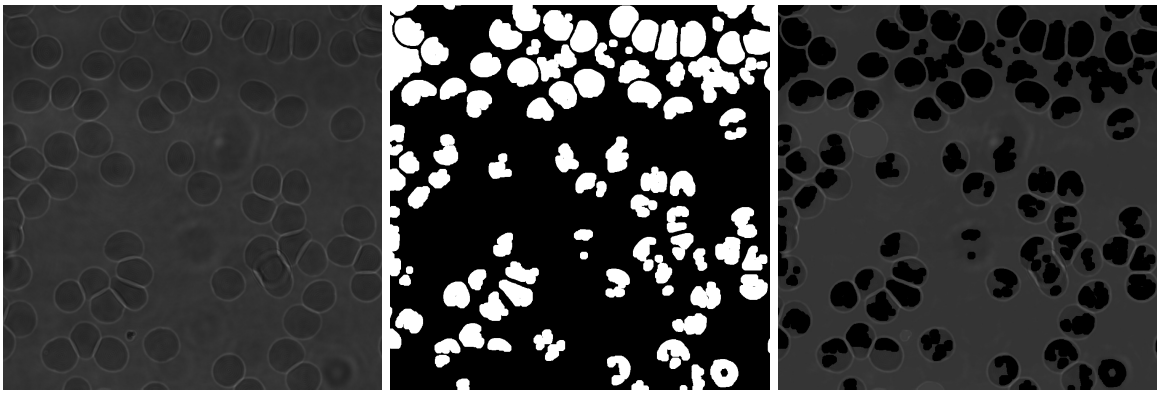
[44] Q. Zheng. Mathematical morphology : Set-theoretic representation for binary shapes. `http://slideplayer.com/slide/7476994/`, 2000. Consulted on Feb 27th 2018.

Appendices

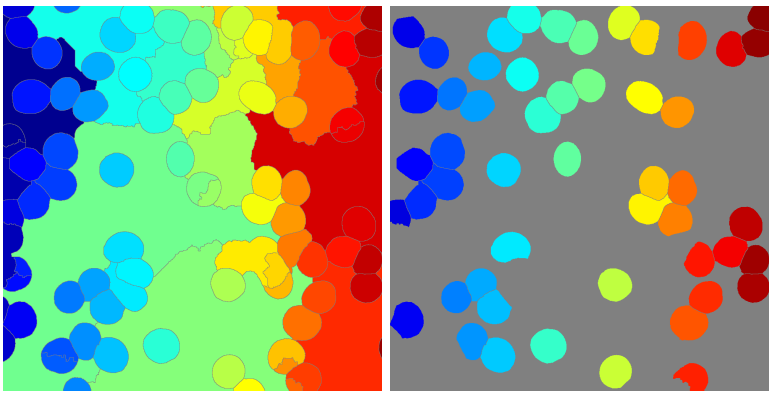
Appendix A

Additional segmentation results

Confocal images

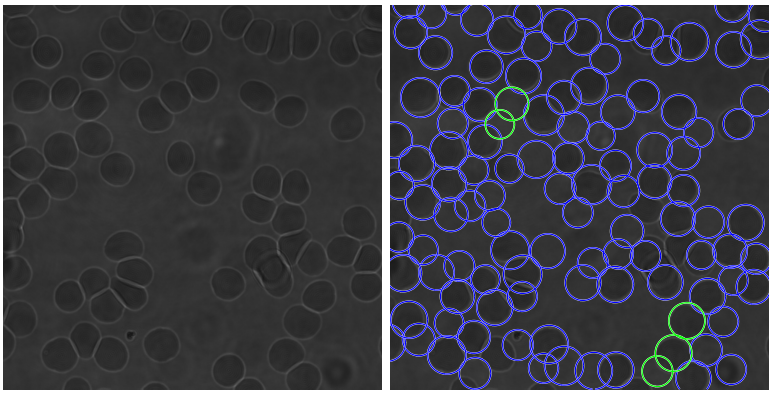


(a) Initial transmission image (b) Marker for watershed control (c) Image used for watershed and obtained by morphological reconstruction

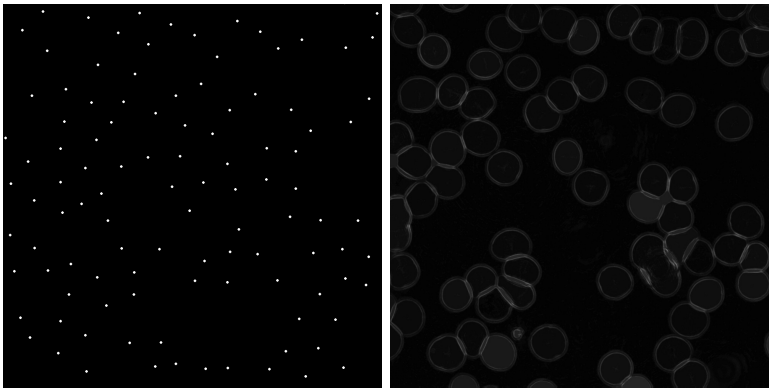


(d) Obtained segmentation (e) Watershed regions kept as cells

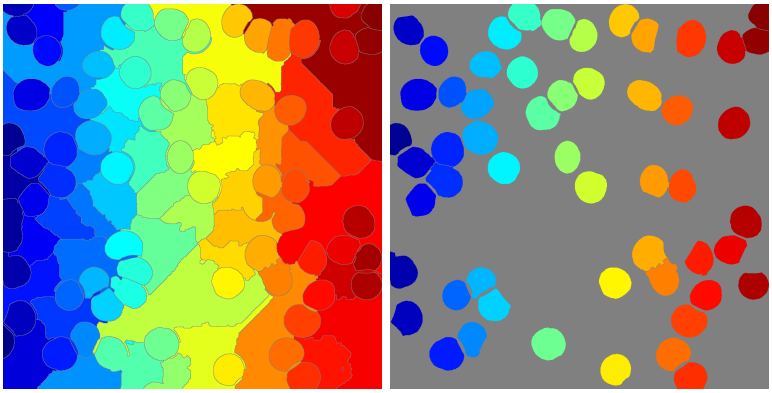
Figure A.1: Results images at each step of the Thresholding controlled watershed for a confocal image of healthy cells (Theta labelling).



(a) Initial transmission image (b) Circles kept by the CHT

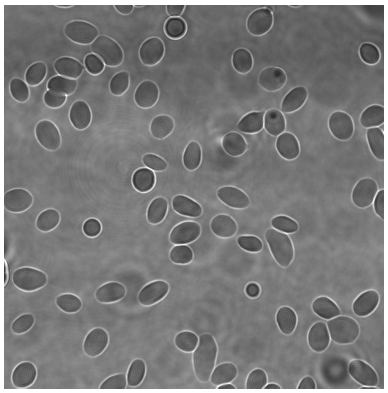


(c) Marker for watershed control (d) Image used for watershed and obtained by morphological reconstruction

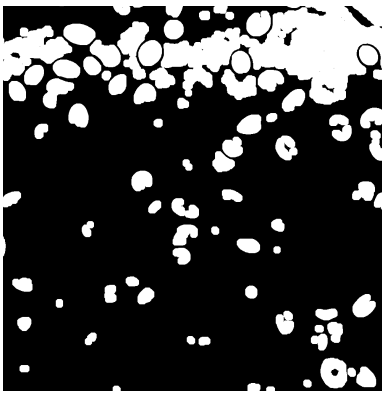


(e) Obtained segmentation (f) Watershed regions kept as cells

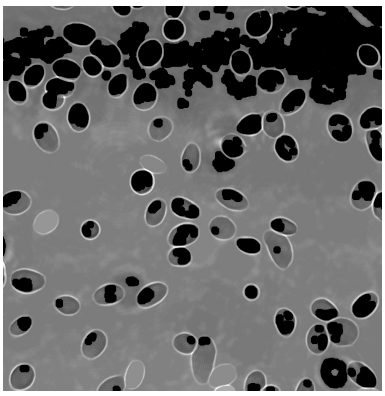
Figure A.2: Results images at each step of the CHT controlled watershed for a confocal image of healthy cells (Theta labelling).



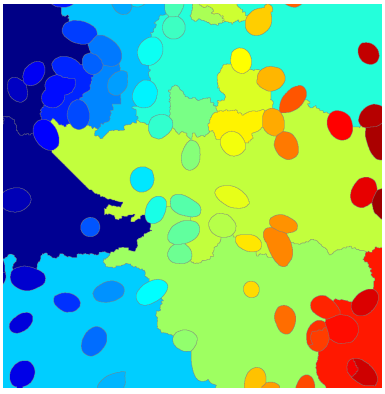
(a) Initial transmission image



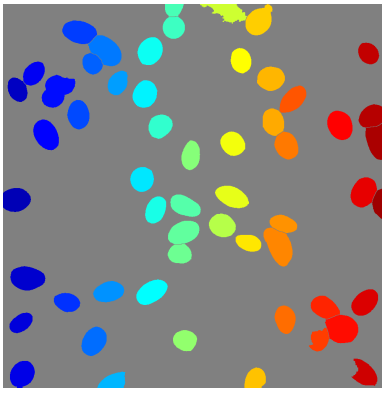
(b) Marker for watershed control



(c) Image used for watershed and obtained by morphological reconstruction

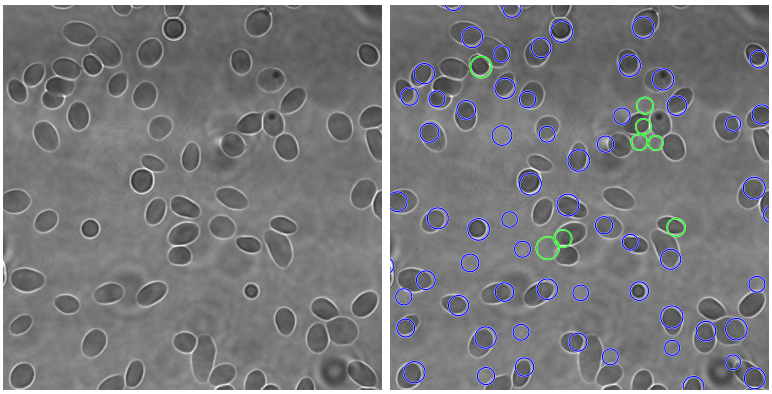


(d) Obtained segmentation

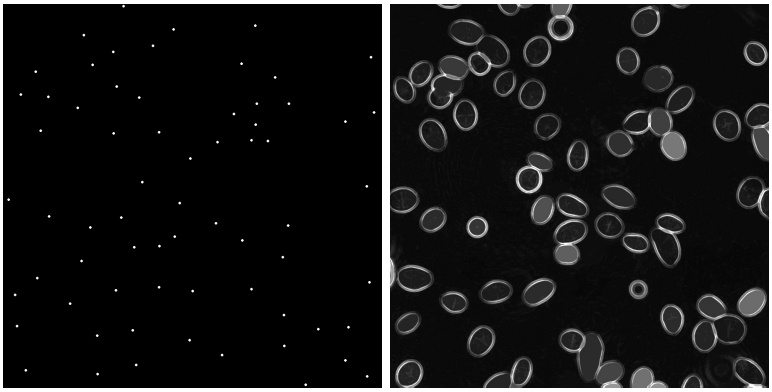


(e) Watershed regions kept as cells

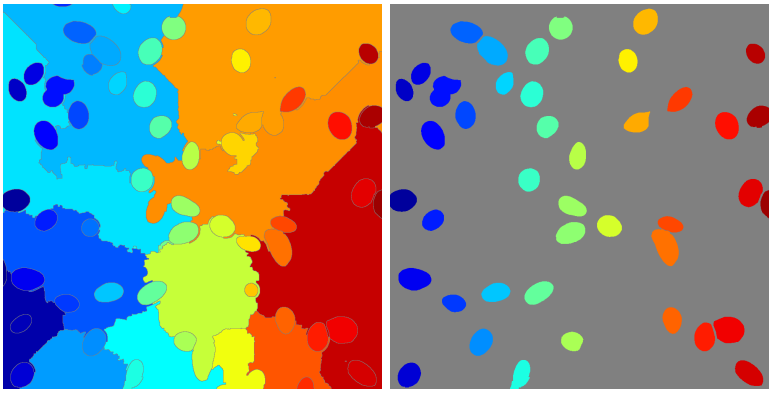
Figure A.3: Results images at each step of the Thresholding controlled watershed for a confocal image of elliptic cells (Theta labelling).



(a) Initial transmission image (b) Circles kept by the CHT



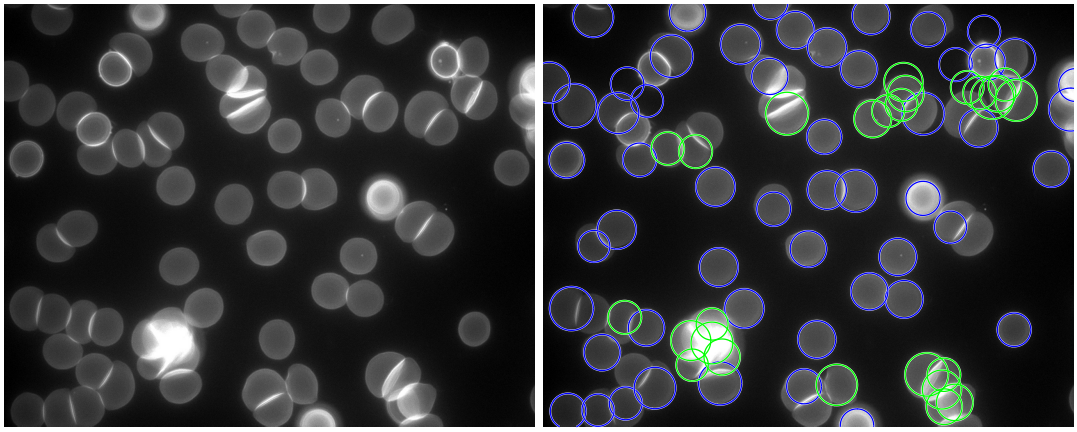
(c) Marker for watershed control (d) Image used for watershed and obtained by morphological reconstruction



(e) Obtained segmentation (f) Watershed regions kept as cells

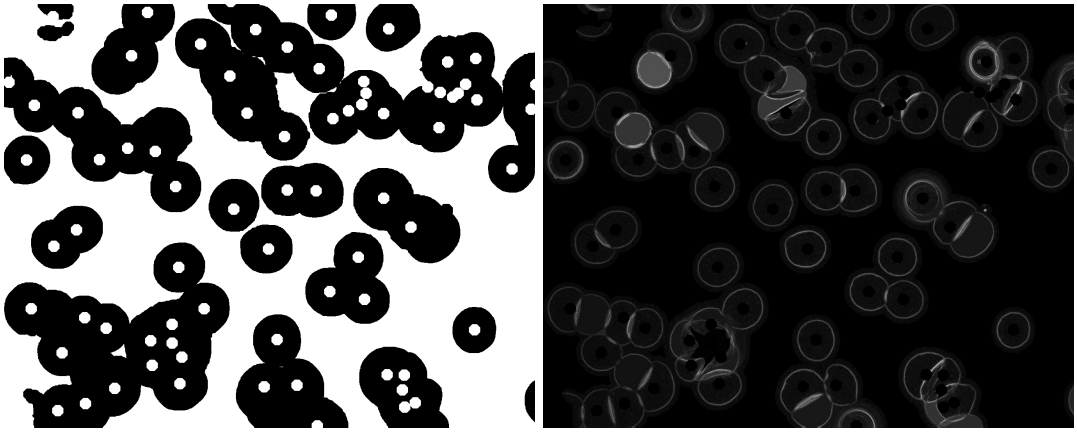
Figure A.4: Results images at each step of the CHT controlled watershed for a confocal image of elliptic cells (Theta labelling).

Wide-field images



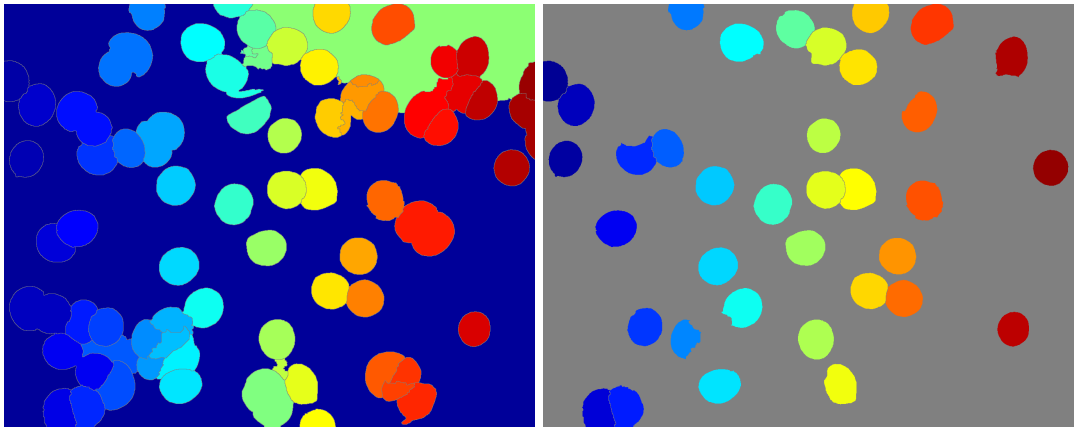
(a) Initial fluorescent image

(b) Circles kept by CHT



(c) Marker for watershed control

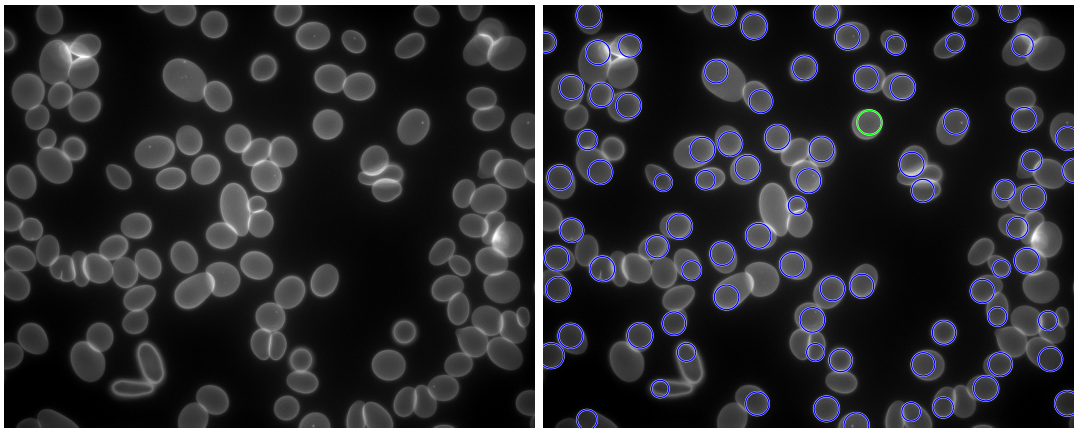
(d) Image used for watershed obtained by morphological reconstruction



(e) Obtained segmentation

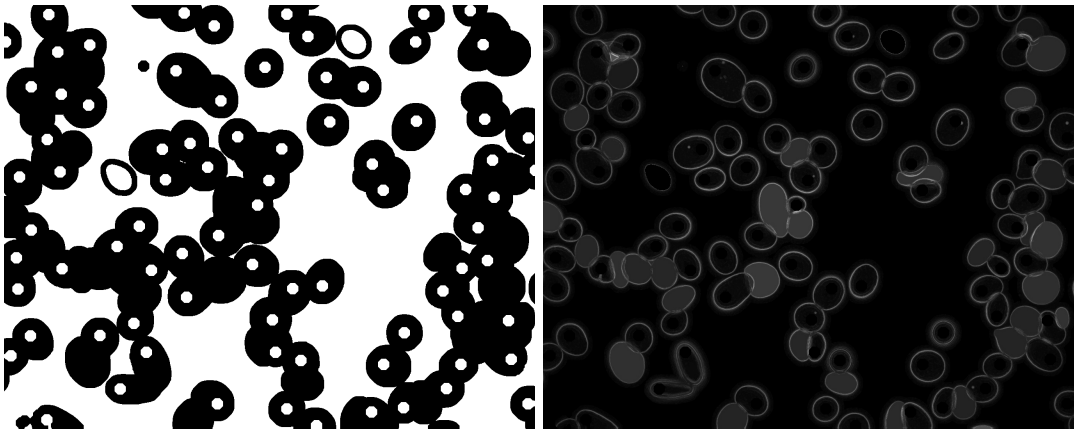
(f) Watershed regions kept as cells

Figure A.5: Results images at each step of the algorithm for a wide-field image of healthy cells (BODIPY-sphingomyelin labelling).



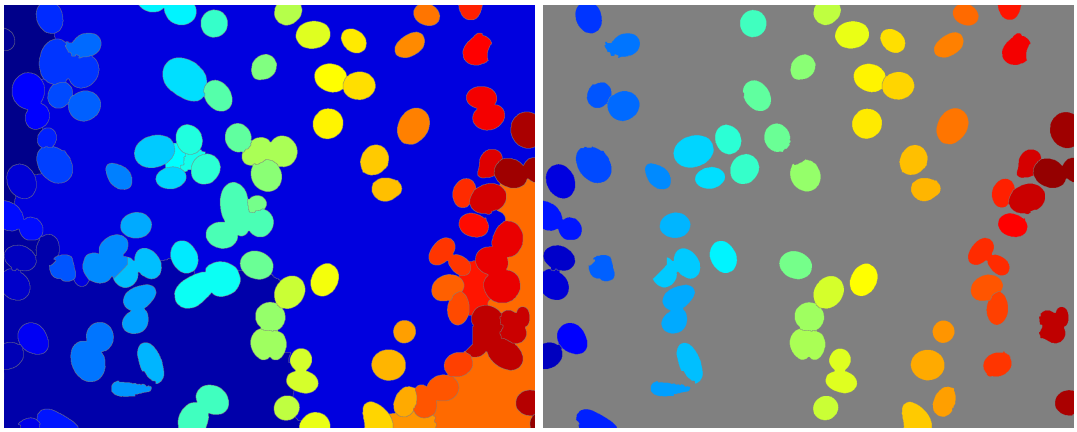
(a) Initial fluorescent image

(b) Circles kept by CHT



(c) Marker for watershed control

(d) Image used for watershed obtained by morphological reconstruction



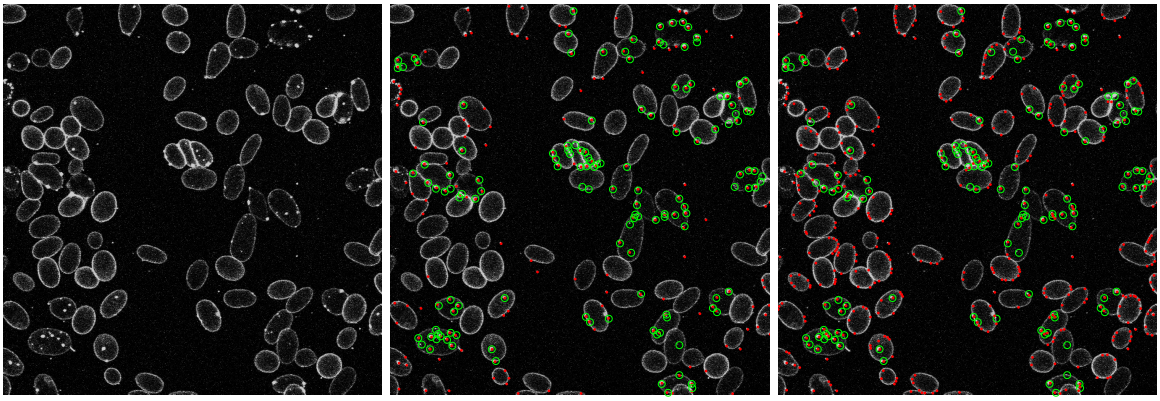
(e) Obtained segmentation

(f) Watershed regions kept as cells

Figure A.6: Results images at each step of the algorithm for a wide-field image of elliptic cells (BODIPY-sphingomyelin labelling).

Appendix B

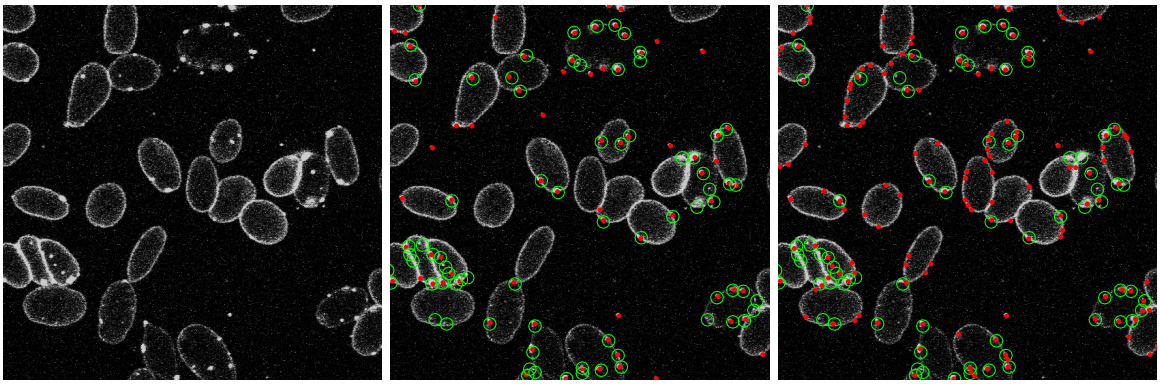
Additional detection results



(a) Initial fluorescent image

(b) Unique thresholding and filtering method

(c) Iterative thresholding method



(d) Initial fluorescent image : zoomed version

(e) Unique thresholding and filtering method : zoomed version

(f) Iterative thresholding method : zoomed version

Figure B.1: Detection results for a confocal image of elliptic cells. Red dots are algorithm results and green circles are ground truth spots.

Rue Archimède, 1 bte L6.11.01, 1348 Louvain-la-Neuve **www.uclouvain.be/epl**

